

1. Accelerators and Detectors

In the following, we concentrate on the three machines SPS, Tevatron and LHC with the experiments UA1, UA2, CDF, D0, ATLAS and CMS, representing the past, present and future of high energy p p physics¹.

The accelerators are treated as ‘black boxes’: the parameters relevant for the experimenters are reviewed, but the physics and technical aspects are not covered.

The detector design is discussed first in general terms, then the six detectors are presented and compared in some detail.

1.1. Accelerators

parameter	SPS	Tevatron	LHC
time	1981-1990	1987-2009	2007-2020
particles	$p + \bar{p}$	$p + \bar{p}$	$p + p$
c.m. energy / GeV	630	1960	14000
circumference l /km	6.91	6.28	26.66
peak lumi / $10^{30}/\text{cm}^2/\text{s}$	6	50	10000
average lumi / $\text{fb}^{-1}/\text{year}$	0.05	0.5	100
number of bunches	6 + 6	36 + 36	2808 + 2808
particles (p, \bar{p}) / bunch / 10^{10}	15, 8	25, 3	11
bunch separation Δt /ns	3800	396	25
beam crossing angle	0	0	300 μrad
inelastic collisions / crossing	0.1	2	20
inelastic collisions / s	$5 \cdot 10^5$	$4 \cdot 10^6$	$8 \cdot 10^8$
particle production / s	$2 \cdot 10^7$	$3 \cdot 10^8$	$1 \cdot 10^{11}$
bunch size σ_x, σ_y / μm	~ 50	30	16
bunch length σ_z /cm	20	38	7.5

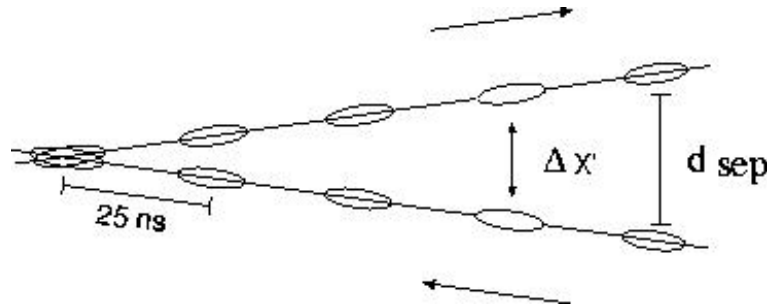
Note: The figures for the SPS refer to the best performance reached; the Tevatron parameters are those expected for the data taking period 2004 of ‘run IIa’; the LHC numbers are design values which will probably not be reached before the end of the decade.

Reference: Review of Particle Physics 2002 (Phys. Rev. D 66 (2002) 1).

Some comments:

i) The beam crossing angle in the LHC (in which two separate beams circulate!) avoids unwanted parasitic collisions:

¹the generic expression p p physics covers both pp and $p\bar{p}$ collisions



Note: $25 \text{ ns} = 7.5 \text{ m}$.

ii) The number \tilde{n} of inelastic collisions per bunch crossing can be calculated this way:

$$\tilde{n} = \dot{N} \Delta t = L \sigma_{inel} \Delta t \quad \sigma_{inel} \sim 50 \text{ mb} \quad (1)$$

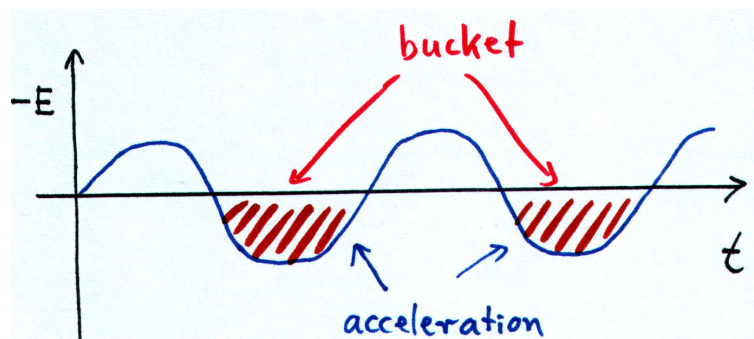
where Δt denotes the (average) bunch spacing.

iii) The *particle* production rate is given by the average particle multiplicity per inelastic collision (increases from 40 at SPS to 140 at LHC²) and the event production rate.

iv) In general the bunch spacing is not uniform in time:

Example Tevatron:

Radiofrequency = RF = 53 MHz. This corresponds to $\tau = 1/\text{RF} = 19 \text{ ns}$ and $d = \tau c = 5.7 \text{ m}$. But not all ‘buckets’ can be filled in this accelerator scheme, only every seventh, resulting in a smallest bunch separation of $7 \cdot 19 \text{ ns} = 132 \text{ ns}$.

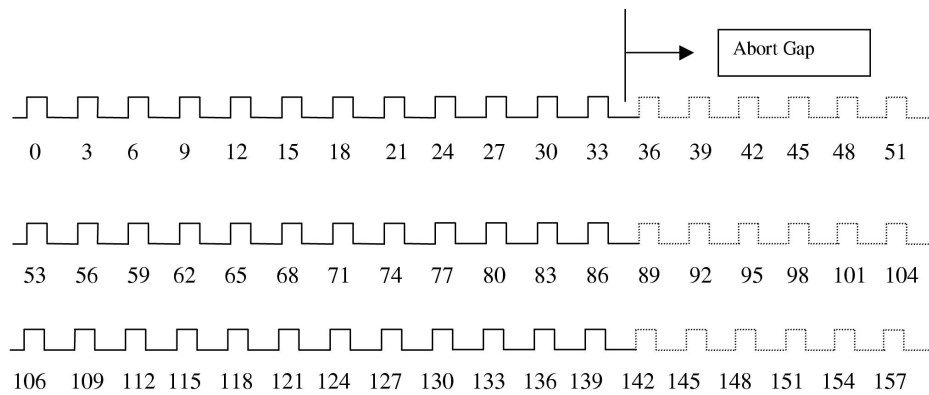


Every 132 ns-clock-signal is called a ‘tick’. This operating mode was originally foreseen for Run IIb, but it might never be realised. It would also require a nonzero beam crossing angle for the reasons explained above.

Currently, in run IIa, only every third tick is filled, that is $\Delta t = 396 \text{ ns}$. However, the timing is more complicated: Along the Tevatron circumference of about $l = 6.3 \text{ km}$ one can fit exactly 153 ticks, which are divided into 3 groups of 53 ticks, since the Tevatron has a threefold symmetry³. But 53 is not a multiple of 3, so that some ‘adjustment’ is necessary, resulting in 12 bunches (= 36 ticks):

²Pythia simulation: all ‘stable’ particles

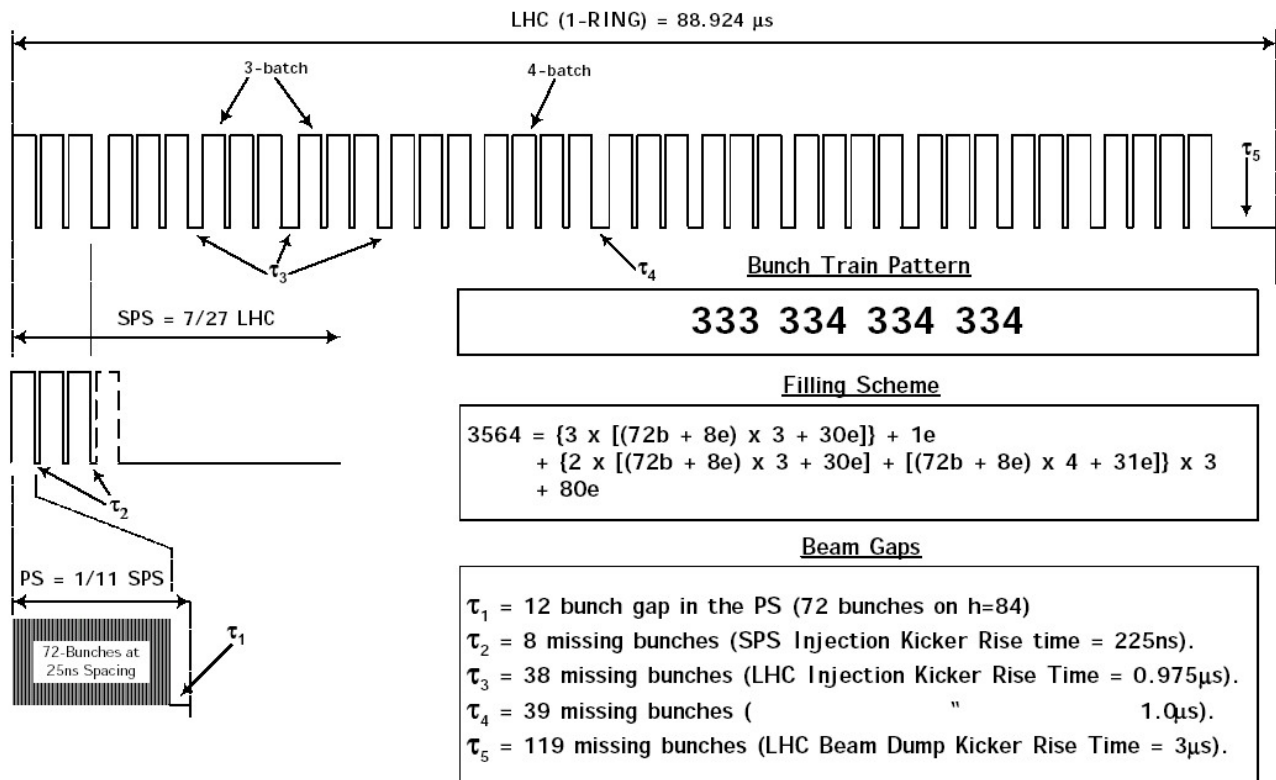
³so that CDF and D0, at a distance of $l/3$, get the same luminosity



Example: LHC⁴:

Radiofrequency = RF = 400.8 MHz. This corresponds to $\tau = 1/\text{RF} = 2.5 \text{ ns}$ and $d = \tau c = 75 \text{ cm}$. Only every 10th bucket is used, resulting in a bunch spacing of 25 ns:

Nominal Proton Bunch Pattern in the LHC for 25ns Spacing



Here ‘glitches’ are unavoidable due to the transfers between the different accelerators: PS → SPS → LHC. Sometimes bunches remain empty, up to 119 in a row! This results in a total of 2808 bunches

⁴for pp operation; in heavy ion mode the bunch separation will be even smaller

per LHC ring/beam. The ‘empty crossings’ can be used to measure backgrounds (electronic noise, cosmics).

v) The transverse beam size is given by the ‘squeezing’ in the nearest quadrupoles. The total longitudinal beam size can not exceed half the ‘wavelength’ d ; here we quote the r.m.s of the distribution, σ_z , which is then limited by $d/(4\sqrt{3})$. The bunch length might be substantially shorter than this limit, if stable beam acceleration is limited to a smaller phase interval.

Beyond the parameters listed in the table, the experimenter is interested in background rates (e.g. proton halo scraping collimators upstream⁵) and - related - the minimum radius of the beam tube (in order to place vertex detectors as close to the interaction region as possible).

1.2. Detectors

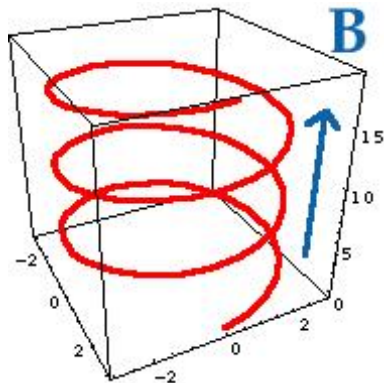
Since the magnet choice has a major impact on the design of all the other detector parts, the different types of magnets are described first in this chapter.

1.2.1. Magnets

A good momentum measurement requires precise detectors and ‘thick’ magnetic fields with a large B field. The track curvature radius grows with particle energy/momentum, so that at high energy colliders this task becomes particularly difficult.

Some formulae:

i) Trajectory inside magnetic field



A charged particle describes a helix inside a homogeneous magnetic field; the radius of curvature for a particle with charge ± 1 is given by

$$R = \frac{p_B}{eB} = 3.3 \text{ m} \cdot \frac{p_B/\text{GeV}}{B/\text{T}} \quad (2)$$

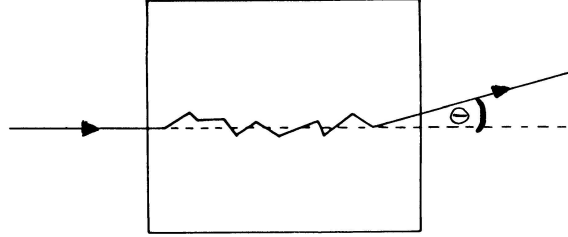
where p_B denotes the component of \vec{p} perpendicular to \vec{B} .

Example: The Tevatron superconducting dipole magnets produce $B = 4.4 \text{ T}$. For 1 TeV particles this implies a radius of $R = 750 \text{ m}$. This number is smaller than the geometrical Tevatron radius of 1 km , since the magnets do not cover all the circumference!

⁵this is not the most important background source at the LHC, see section 1.2.2

ii) Multiple scattering

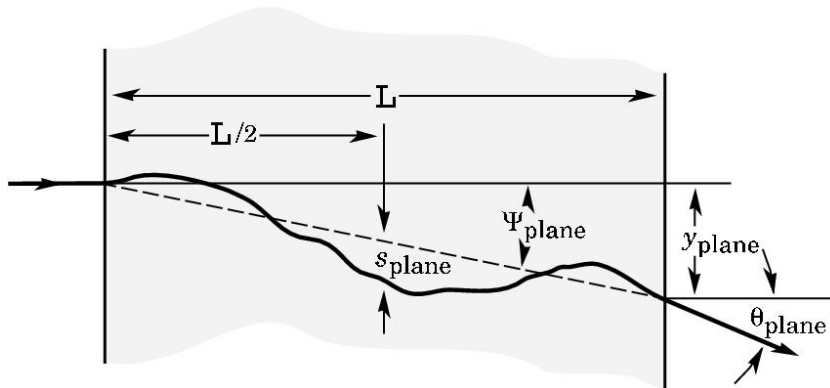
Multiple deflections in the Coulomb field of nuclei result in both a spatial and an angular displacement:



The overall scattering angle is Gaussian distributed. In one projection the width is given by

$$\theta_{MS} = \frac{13.6 \text{ MeV}}{p} \sqrt{\frac{L}{X_0}} \left(1 + 0.038 \ln \frac{L}{X_0}\right) \quad (3)$$

for relativistic particles with unit charge. The last factor is close to 1 and can often be ignored. L is the traversed matter thickness and X_0 the radiation length of the material.



The track displacement is (approximately)

$$y_{MS} = \frac{1}{\sqrt{3}} L \theta_{MS} \quad (4)$$

and

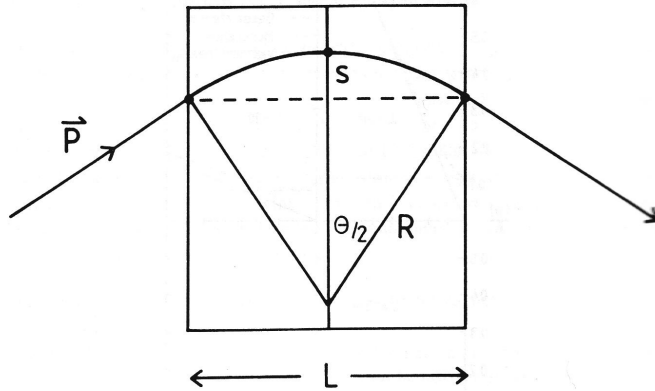
$$s_{MS} = \frac{1}{4\sqrt{3}} L \theta_{MS} \quad (5)$$

Reference: Review of Particle Physics 2002 (Phys. Rev. D 66 (2002) 1).

Example: A muon of $p = 1 \text{ GeV}$ is deflected by typically $\theta_{MS} = 0.6^\circ$ (in one projection) when passing through $L = 1 \text{ cm}$ of iron ($X_0 = 1.8 \text{ cm}$).

iii) Curvature measurement

The momentum resolution depends on the detector precision, on the amount of material the particle has to traverse, and on the measurement principle. In collider experiments often the sagitta s is measured inside the magnet region:



At least three coordinate measurements are necessary. It is also possible to measure the track direction inside and/or outside the magnet area and to include the collision point as a constraint in the momentum determination - but we will not discuss these points here.

The sagitta is given by (\rightarrow tutorial)

$$s = \frac{e B L^2}{8 p_B} = 0.3 \text{ m} \frac{B/\text{T} (L/\text{m})^2}{8 p_B/\text{GeV}} \quad (6)$$

Obviously, the more precise the s measurement, the better the momentum resolution. The quadratic dependence on L is very important! Some comments on this dependence:

- intuitive explanation: trajectory in homogeneous field (angle $\vec{p} - \vec{B}$ approx. constant) = parabola: transverse momentum $\sim L$, spatial deviation $\sim L^2$.
- doubling the radius of an inner tracking detector = fourfold improvement in momentum resolution! Difficult to reach by increasing B or by improving detector resolution!
- If a detector is subdivided into two independent identical halves, each of thickness $L/2$: Measuring the sagitta twice and combining the momentum measurements yields a resolution which is worse by a factor $4/\sqrt{2}$ compared to the full detector's resolution. To avoid this degradation a common track fit through both detector parts is mandatory, implying: no material (MS) in between, negligible alignment uncertainties.

Example: A muon of $p = 100 \text{ GeV}$ traversing a magnetic field $B = 1 \text{ T}$ (at right angles) of thickness $L = 1 \text{ m}$ results in a sagitta of only $s = 0.4 \text{ mm}$.

A sagitta measurement requires three coordinate measurements, for example the measurement of y_1 , y_2 and y_3 at the coordinates $x_1, x_2 = x_1 + L/2, x_3 = x_1 + L$ along the trajectory:

$$s = y_2 - \frac{y_1 + y_3}{2}. \quad (7)$$

The formula implies that the central point should be measured more precisely than the outer ones. This can be realized by using *four* identical coordinate detectors, which measure independently with a resolution of Δy at $x = 0, x = L/2, x = L/2$ (!) and $x = L$:

$$s = \frac{y_{2a} + y_{2b}}{2} - \frac{y_1 + y_3}{2}. \quad (8)$$

In this case the sagitta error is

$$\Delta s = \Delta y \cdot \sqrt{1/4 + 1/4 + 1/4 + 1/4} = \Delta y \quad (9)$$

Example: A detector resolution of $\Delta y = 0.1$ mm yields $\Delta s = \sqrt{1.5} \Delta y = 0.12$ mm using three detectors and $\Delta s = \Delta y = 0.1$ mm with four detectors.

iv) Momentum resolution

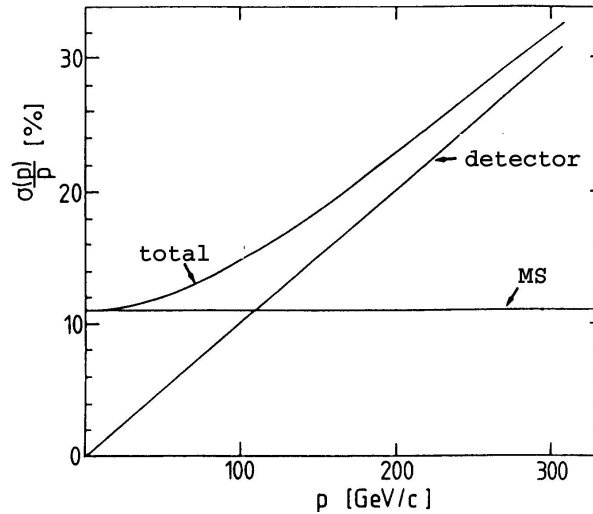
In many cases the relative momentum resolution can be parametrised as follows:

$$\frac{\Delta p}{p} = \frac{\Delta p_{det}}{p} \oplus \frac{\Delta p_{MS}}{p} = c_{det} \cdot \frac{p}{\text{GeV}} \oplus c_{MS} \quad (10)$$

where $a \oplus b$ stands for $\sqrt{a^2 + b^2}$.

Here $\vec{p} \perp \vec{B}$ was assumed, the more general case is discussed below. This formula applies for example when a muon track through an iron yoke is measured several times in 'holes' inside the material along the trajectory.

Note that the detector resolution contribution is growing with p , while the MS part is independent of momentum:



From the sagitta formula (6) we can calculate the detector term c_{det} :

$$\frac{\Delta p}{p} = \frac{\Delta s}{s} = 8 \cdot \frac{\Delta y}{eL^2 B} \cdot p = 26.4 \cdot \frac{\Delta y/\text{m}}{L^2/\text{m}^2 B/\text{T}} \cdot p/\text{GeV} \quad (11)$$

assuming $\Delta s = \Delta y$, thus

$$c_{det} = 0.026 \cdot \frac{\sigma/\text{mm}}{L^2/\text{m}^2 B/\text{T}} \quad (12)$$

All these formulae assume $\vec{B} \perp \vec{p}$!

The multiple scattering term can be calculated in a similar way from the fake sagitta (equation 5):

$$c_{MS} = \frac{\Delta p}{p} = \frac{s_{MS}}{s} = \frac{1}{4\sqrt{3}} L \frac{13.6 \text{ MeV}}{p} \sqrt{\frac{L}{X_0}} \cdot 8 \frac{1}{L^2 B} \cdot p = \frac{16 \text{ MeV}}{L B} \sqrt{\frac{L}{X_0}} \quad (13)$$

$$= \frac{0.052}{L/\text{m} B/\text{T}} \sqrt{\frac{L}{X_0}} \quad (14)$$

Example: We assume a magnetic field of 2 T and an iron layer of $L = 1\text{ m}$ thickness. For the 4 chamber model with $\Delta y = 0.1\text{ mm}$ we get

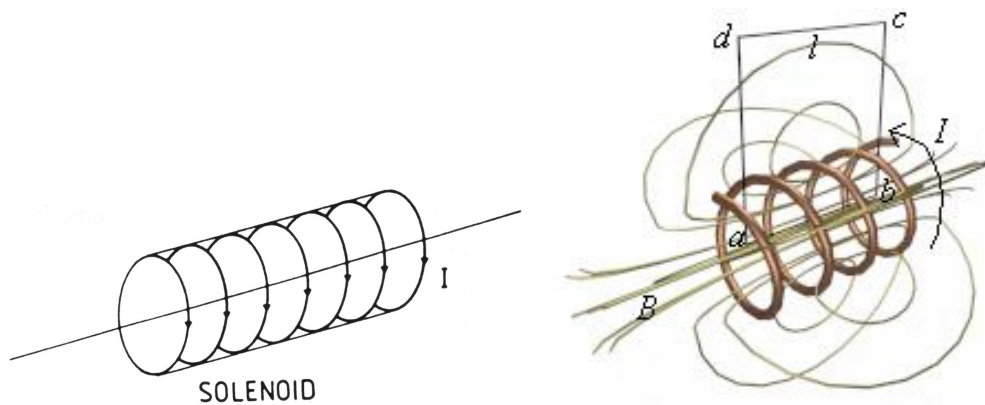
$$c_{det} = 0.13\% \quad c_{MS} = 19\% \quad (15)$$

Thus the detector contribution becomes relevant only for momenta above $\sim 100\text{ GeV}$.

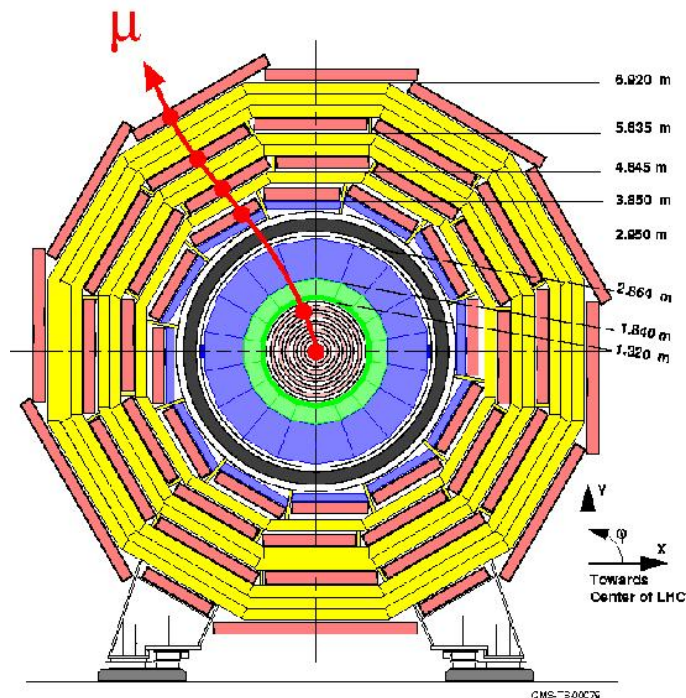
v) Magnetic field configurations

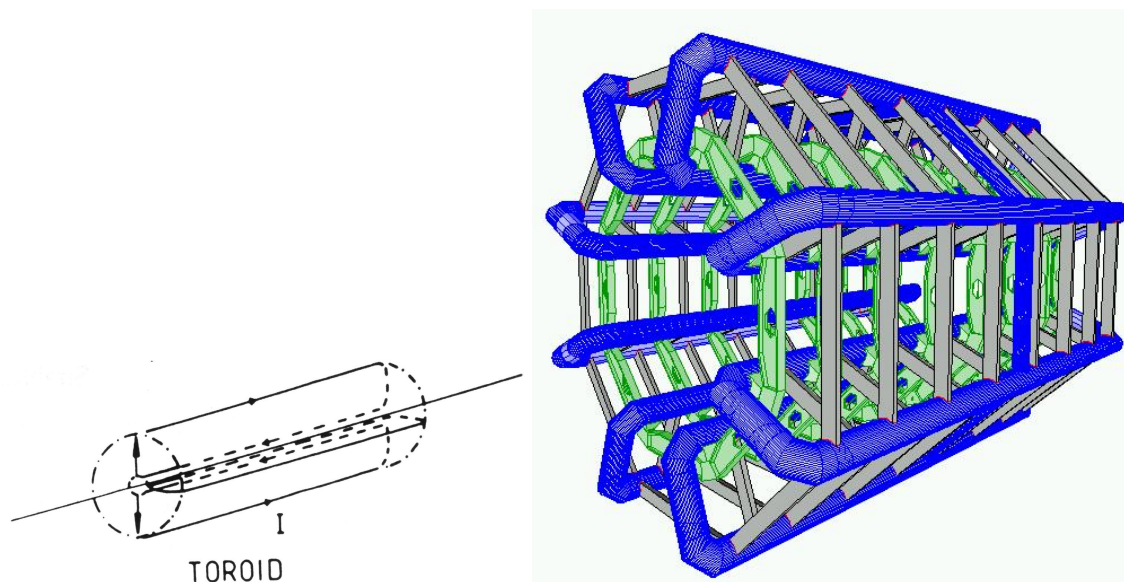
Since the beam must not be disturbed by the detector's magnetic field only two field configurations seem possible:

a) Solenoid



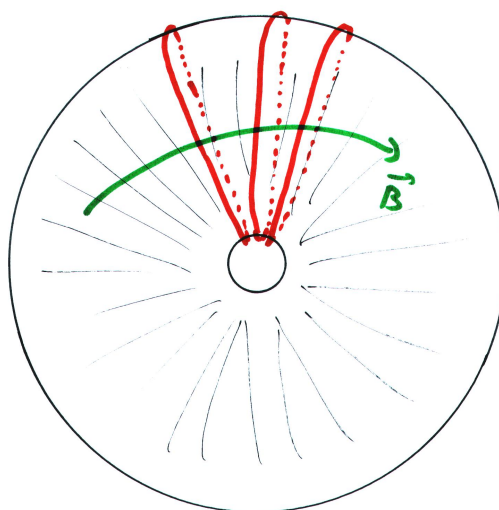
The symmetry axis of the solenoid coincides with the beam line, so $\vec{v} \times \vec{B} = \vec{0}$. The cross section of the coil can be circular, but also a rectangular design will work. The field lines extend far outside the magnet; to avoid related problems one can capture the field in a cylindrical magnet yoke outside the solenoid and feed it back. Another advantage of the yoke is the extra field that can be used to (re)measure track momenta.



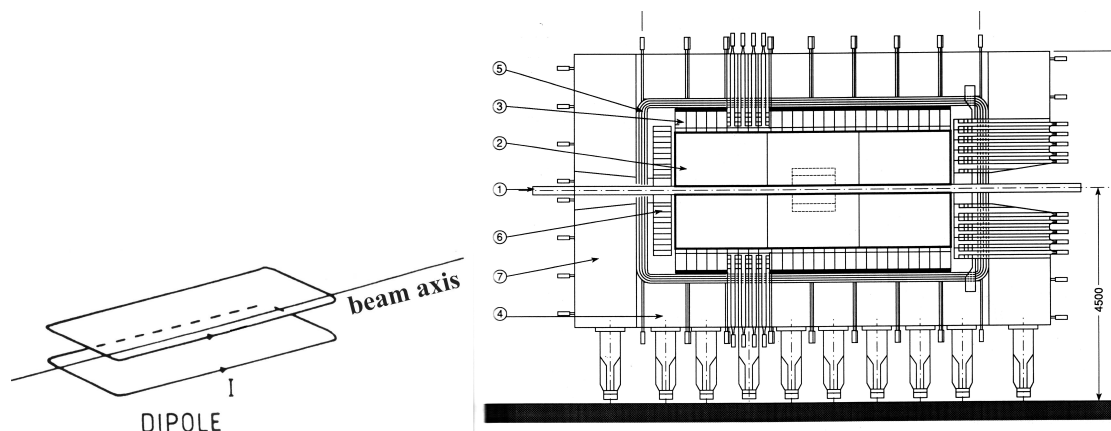
b) Toroid

Toroids contain closed B field lines, thus there is no need for extra yokes, avoiding the resulting multiple scattering!

In the endcap regions often iron toroids are used:



c) There is a notable exception to the rule $\vec{v} \times \vec{B} = \vec{0}$: the UA1 detector used a horizontal dipole field (generated by a 'rectangular solenoid') which was oriented perpendicular to the beam:



Of course this requires another magnetic field outside the detector to compensate. A dipole magnet can never be used in electron accelerators, due to the induced synchrotron radiation.

Some general comments on magnet technology:

- The magnetic fields can be generated by ‘conventional’ or by superconducting coils, the latter type is used in all modern experiments. The resulting field strengths are in the range **0.7 T** (UA1 dipole) to **4 T** (CMS sc. solenoid). These values are limited by the power dissipation (conventional) and the breakdown of superconductivity for high B fields. The field strength inside an iron magnet is normally close to the saturation value, i.e. $B = 1.5 - 1.9$ T.
- Superconducting magnets need a cryostat, thus complicating the detector design.
- Mechanical forces can be important. Example: the CMS iron yoke can move by $\mathcal{O}(cm)$ when the coil is turned on/off.
- The energy stored is huge. Quenches must be avoided. Example: ATLAS toroid = 1500 MJ.
- An iron filled magnet needs substantially lower currents than an air magnet. Examples: D0 central toroid: each coil: $n I = 25$ kA, ATLAS barrel toroid: each coil = 3 MA.

Comparison of ‘physics performance’:

The two main aspects are:

* multiple scattering: dominated by iron yoke (if existing); severe limitation for momentum resolution, see above.

* field geometry:

a) barrel toroid: bending in plane containing beam

+ $\vec{p} \perp \vec{B}$, in barrel toroid $B L^2$ largest at small angles!

- no vertex constraint (long collision region)

- no field in central detector part

b) barrel solenoid: axial field, bending in plane perpendicular to beam

o \vec{p}_\perp is measured, resolution indep. of angle (without MS)

+ vertex constraint (small beam diameter)

+ B field inside and close to beam pipe

c) barrel dipole: bending in plane containing beam, ϕ dependent!

+ $B L^2$ largest at small angles, works even for $\eta \pm \infty$.

- no vertex constraint (long collision region)

- no bending for tracks $\parallel \vec{B}$

- needs compensation

In the forward region there is less choice: only toroids make sense ($\vec{P} \approx \perp \vec{B}$).

Above the momentum resolution formulae were given for barrel magnets at $\theta = 90^\circ, \eta = 0$. For other polar angles the following modifications have to be taken into account for cylindrical magnets:

- solenoids measure p_T ($\rightarrow p = p_T / \sin \theta$).

- toroids measure p , effective track length $L = L_0 / \sin \theta$, resolution $\sim 1/L^2$ (sagitta method).

- similar for dipole, but additional ϕ dependence.

- multiple scattering increases: effective thickness = $L_0 / \sin \theta$.

Summary of the magnet configurations of the six pp detectors:

experiment	UA1	UA2	CDF	D0	ATLAS	CMS
solenoid	-	-	1.6 T sc	2.0 T sc	2.0 T sc	4.0 T sc
solenoid yoke	-	-	iron	-	yes	1.6 T iron
barrel toroid	-	-	-	1.9 T iron	4 T sc air	-
endcap toroid	-	yes	iron	2.0 T iron	4 T sc air	-
endcap yoke	-	yes !	-	-	-	2 T iron
dipole	0.7 T	-	-	-	-	-
dipole yoke	1.8 T iron	-	-	-	-	-

Some (expected) performance figures (depend of course on position resolution) for $\eta = 0$:

CMS central tracker:

$$\frac{\Delta p}{p} = 0.012\% \cdot p/\text{GeV} \oplus 0.5\% \quad (16)$$

ATLAS toroid:

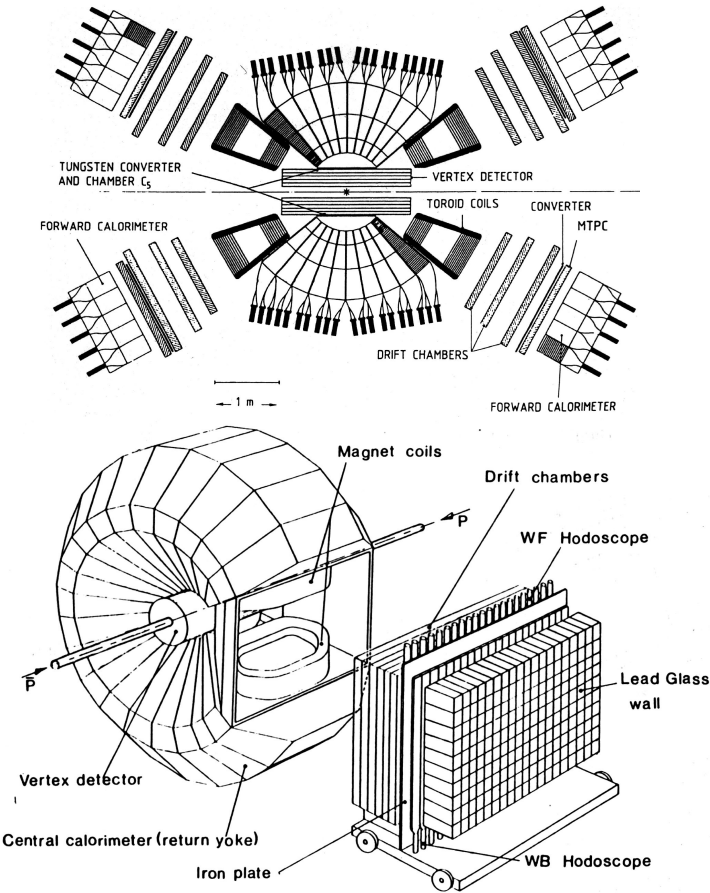
$$\frac{\Delta p}{p} = 0.01\% \cdot p/\text{GeV} \oplus 1.5\% \quad (17)$$

D0 toroid:

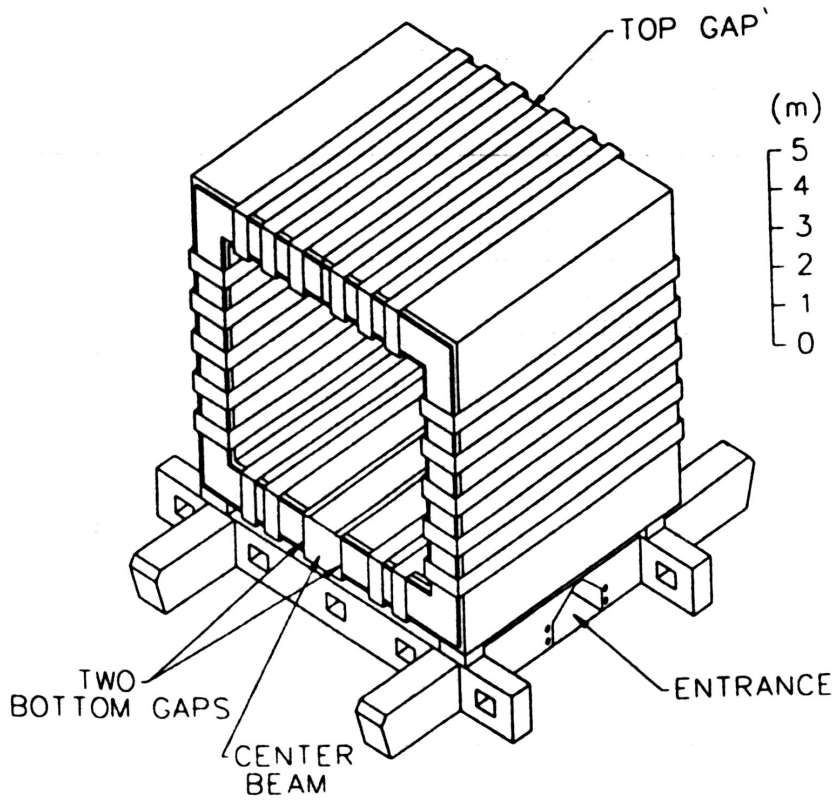
$$\frac{\Delta p}{p} = 0.3\% \cdot p/\text{GeV} \oplus 18\% \quad (18)$$

Finally a few pictures:

UA2 detector:



D0 toroid:

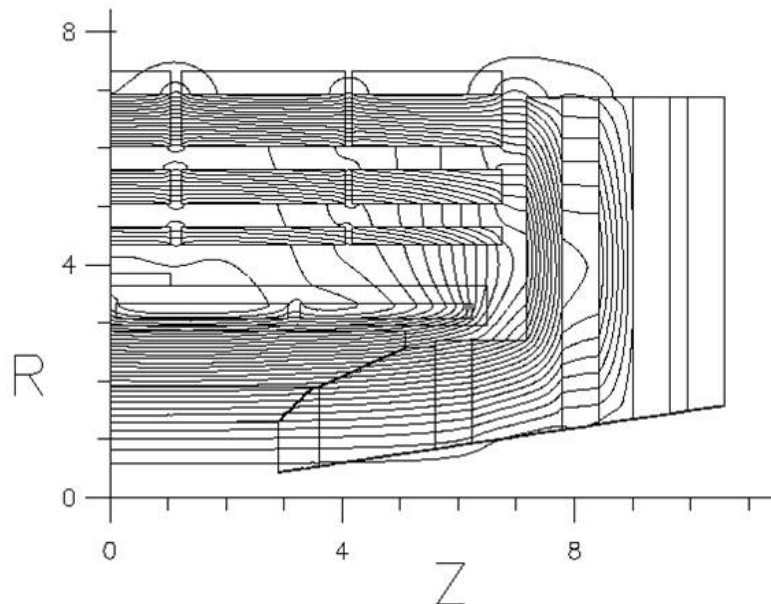


Note: here no sagitta measurement, but determination of track direction before and after traversing magnet.

Atlas toroid coil:



CMS magnetic field:

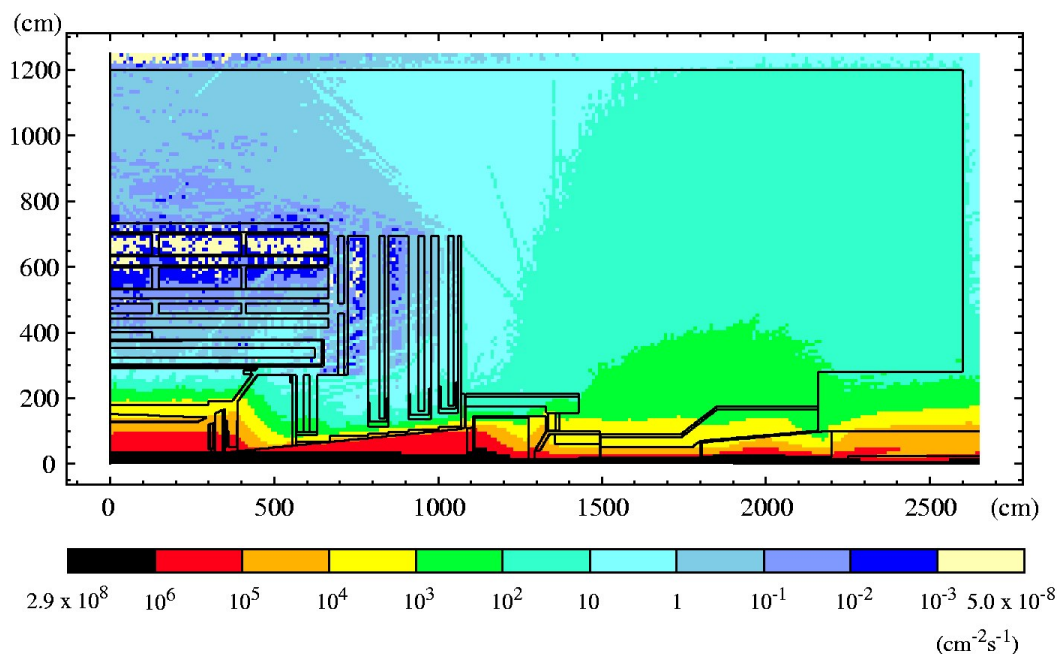


1.2.2. Detectors - general considerations

The high particle rate at proton colliders implies:

- Detectors (and electronics) must be radiation hard. The expected dose obviously depends very much on the location; it is highest close to the beam pipe in forward/backward direction. The exposure can be measured as deposited energy / mass of exposed material (unit Gy = J/kg = 100 rad)¹ or in terms of particle fluence (= integrated flux). Which quantity is better suited to characterize a potential damage depends on the type of detector.

Example: At nominal LHC operation for one year some shielding elements near the detector regions suffer from neutron fluences of up to $10^{16}/\text{m}^2$ and 100 Gy. In the detector itself the dose is lower by at least 2 orders of magnitude.

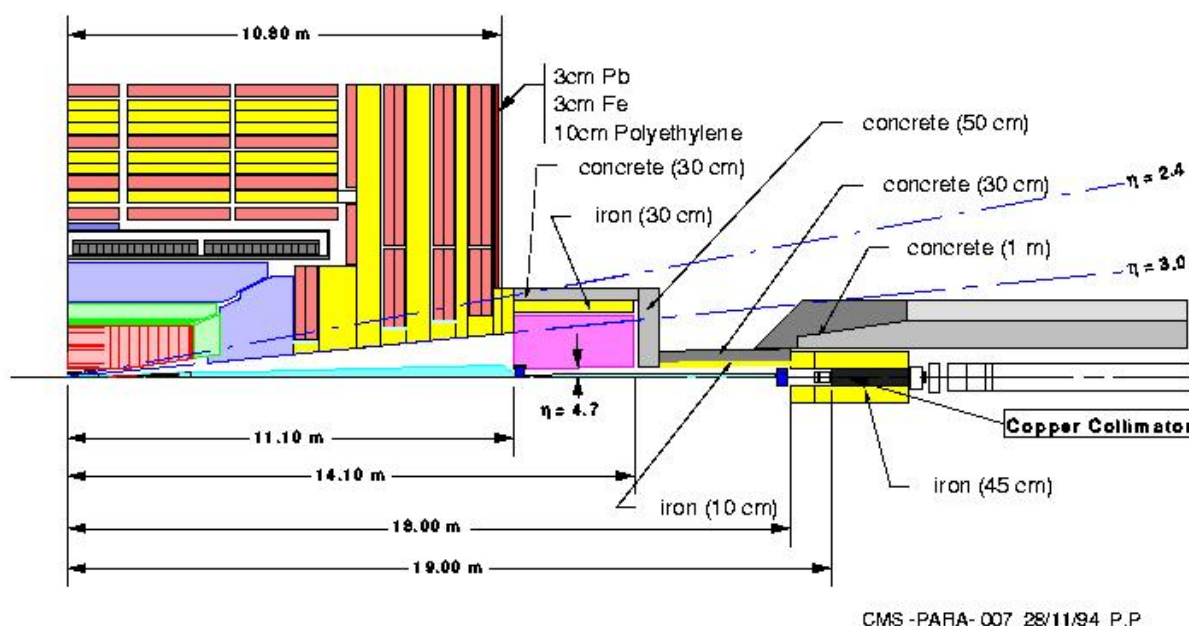


The LHC background is particularly high, we will discuss only this case in the following². The background stems mainly from pp collisions in the collision region (10^{11} particles / second), and not from beam-gas, beam-wall interactions and not from synchrotron radiation.

Example: At both ends of the CMS detector two collimators are installed which absorb many particles created at large η values. Each collimator absorbs per event on average 2.1 TeV (exposure from 'inside'!), corresponding to a power of $2.1 \text{ TeV} \cdot 40 \text{ MHz} = 13 \text{ W}$.

¹10 Gy = lethal

²Also at the Tevatron radiation damage plays an important role; the silicon track detectors have an estimated 'lifetime' of only a few fb^{-1} ! Even at the SPS detectors degradation due to radiation was an issue - for example the scintillators of the UA2 hadron calorimeter had to be replaced...



Even those detector elements, which are rather far away from the collision region see a high background rate.

Example: The background in the CMS muon chambers (up to 10 MHz/m^2) is dominated by low energy electrons from neutron capture and by charged hadrons (and not by muons!)

In addition to ‘normal’ radiation a ‘catastrophic beam loss’ might (should not!) occur, in which case the exposed detector parts or collimators would be locally destroyed. Worst case: All protons ($3 \cdot 10^{14}$) are lost, corresponding to an energy deposit of 0.3 GJ.

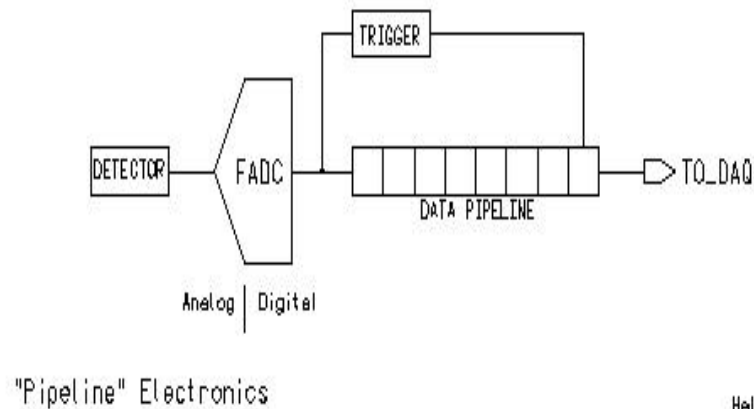
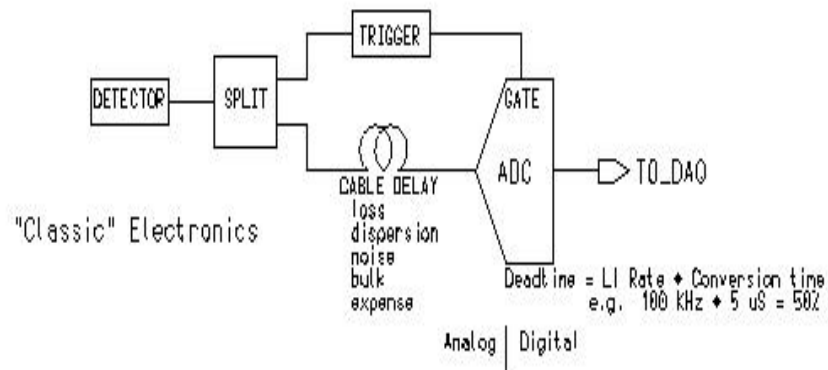
- Detectors (and electronics) must be fast; it is desirable to extract the signal before the next bunch crossing arrives. In general this is not possible; since signals overlapping in time can in general not be disentangled, the probability of such overlaps must be kept small. This is quantified by the ‘occupancy’ O of a given detector cell, this is the probability that at a given moment the cell (not the readout!) is ‘busy’. Apart from the speed the cell size (detector granularity) influences the occupancy: the more cells, the better. . . Modern pp detectors must therefore avoid long drift- or relaxation times and need a huge number of independent detector cells.

Example: In the CMS barrel muon system a single drift cell ‘fires’ with a rate of about $f = 10 \text{ kHz}$ (mainly charged particle background, not muons!). The maximum drift time amounts to $t = 400 \text{ ns}$, thus $O = f t < 1\%$. (Note: ions drift much longer, so a small local E-field distortion will be felt even after a few 1000 bunch crossings!)

Counter example: In the TPC (Time Projection Chamber) of the Aleph experiment at LEP the maximum drift time is $55 \mu\text{s}$, corresponding to 2000 bunch crossings.

Example: ATLAS pixel detector, estimate: The total number of pixel cells ($50 \mu\text{m} \times 400 \mu\text{m}$) is $\sim 10^8$. It takes less than 25 ns for the electrons/holes to drift through the depletion layer. Since each bunch crossing produces ‘only’ ~ 1000 particles traversing the pixel detector, the cell occupancy is negligible.

- The detector signals must be kept till a trigger decision has been made. This can last of the order of milliseconds, so a ‘pipeline’ storage system is needed:



Hall D
December, 1999

1.2.3. Calorimeters

Important aspects:

- electromagnetic / hadronic
- sampling or homogeneous
- compensation (jets)
- readout (light, charge)
- speed
- energy resolution
- spatial resolution / transverse sampling (granularity)
- longitudinal sampling (electron-hadron separation)
- absolute energy scale

- η coverage, hermeticity

What matters in particular for the data analysis are energy and spatial resolution.

Example: Invariant mass of high energy particle pair:

$$m^2 = 2 E_1 E_2 (1 - \cos \theta_{12}) \quad \rightarrow \quad (\theta_{12} \ll 1) \quad \rightarrow \quad m^2 = E_1 E_2 \theta_{12}^2 \quad (1)$$

The energy resolution can be parametrised in the following way:

$$\frac{\Delta E}{E} = \frac{A}{\sqrt{E/\text{GeV}}} \oplus \frac{B}{E/\text{GeV}} \oplus C \quad (2)$$

The sampling constant A describes the intrinsic shower fluctuations (number of particles N etc.), the variation of the sampling fraction and the ionization/photoelectron statistics. Due to the statistical nature and the relation $N \sim E$, the sampling term decreases with \sqrt{E} . Electronic and other sources of noise effectively contribute an energy offset (B) with size independent of E , thus the relative influence drops with $1/E$. Calibration uncertainties and material inhomogeneities lead to a constant term C , which dominates at high energy.

Good electromagnetic calorimeters reach $A \sim 10\%$, $B = 0.5$ (GeV !), $C = 1\%$.

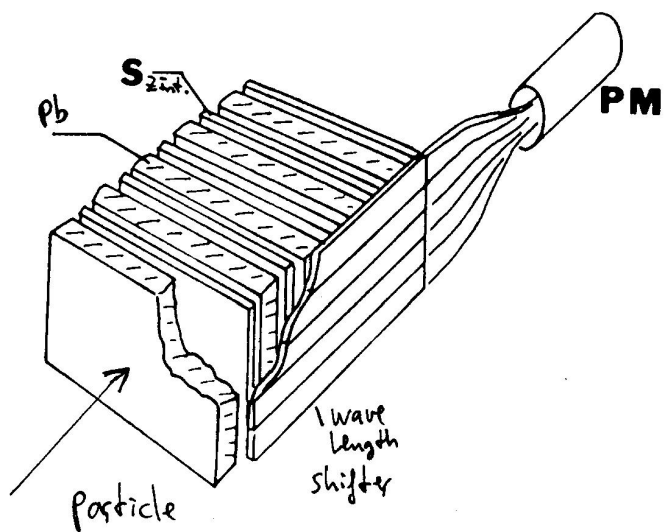
Hadron calorimeters are considered good if $A \sim 50\%$, $B = 1$ (GeV !), $C = 5\%$.

Also the position resolution improves with energy.

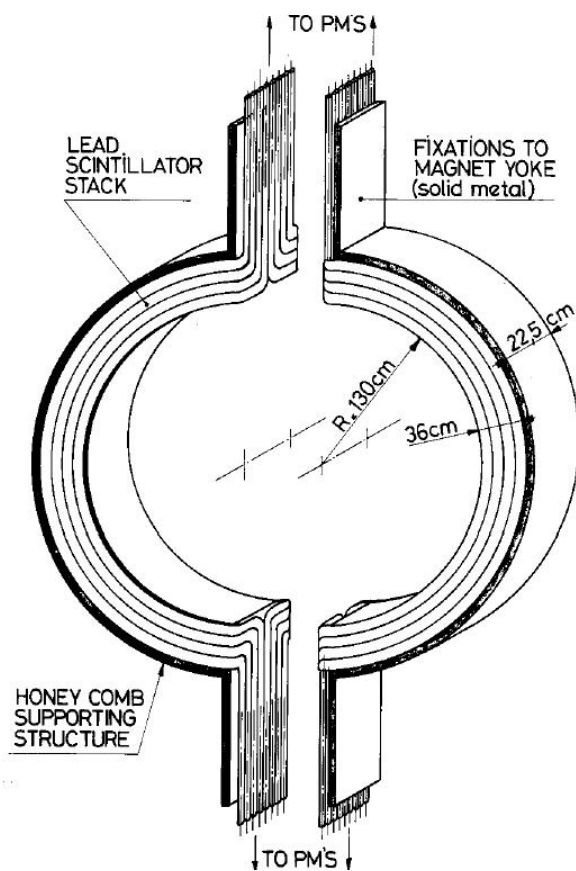
Electromagnetic (hadronic) detectors must have a thickness of approx. $20 X_0$ (10λ) in order to absorb the shower completely. X_0 (λ) denotes the radiation length (absorption length). These material constants should be small to allow for a compact calorimeter design. ‘Classical’ materials for the passive layers in sampling calorimeters are lead (high Z) and iron (high density, easy to handle).

In the following I will first describe the various calorimeter concepts used in the six pp detectors and then I try to compare and evaluate.

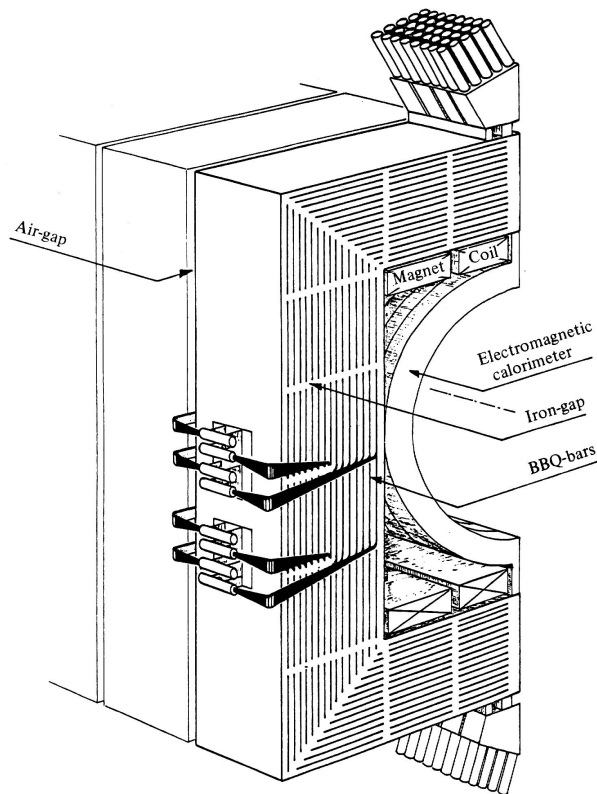
The **UA1** experiment uses ‘classical’ lead-scintillator and lead-iron (magnet yoke) sampling calorimeters with PM readout. New was at that time the light transport via wavelength shifting fibres, which avoids large dead regions:



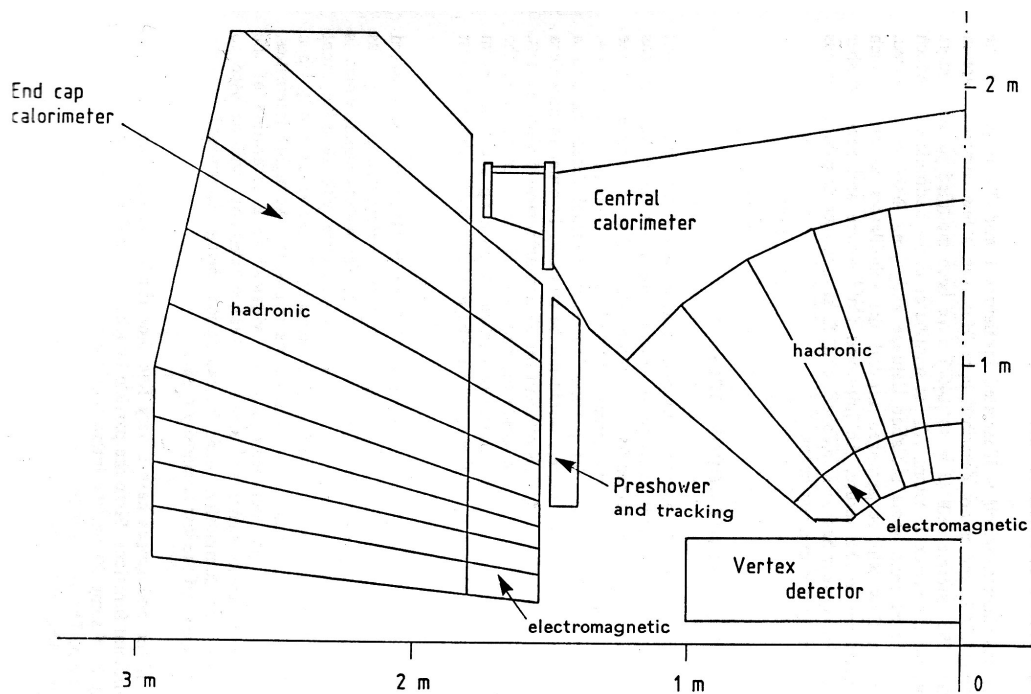
'Gondolas' (elm):

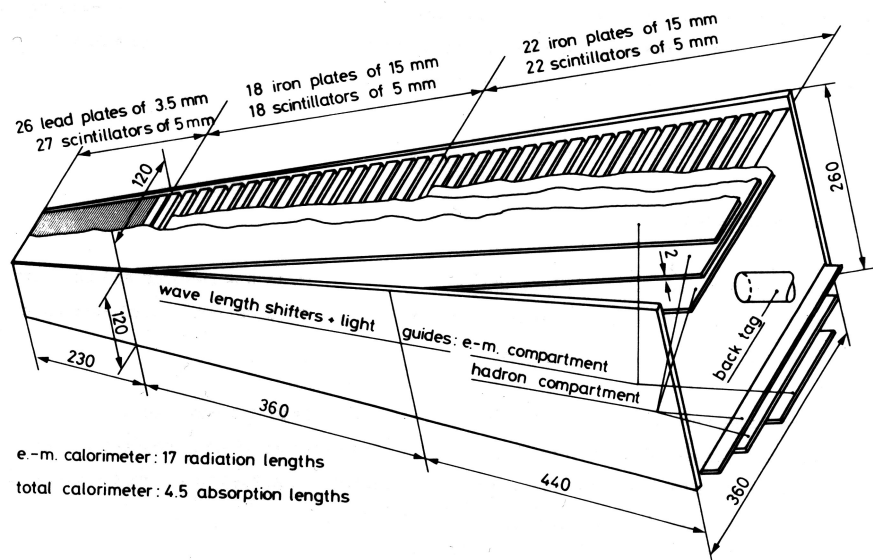


Hadron calorimeter:



The UA2 detector employs similar techniques:



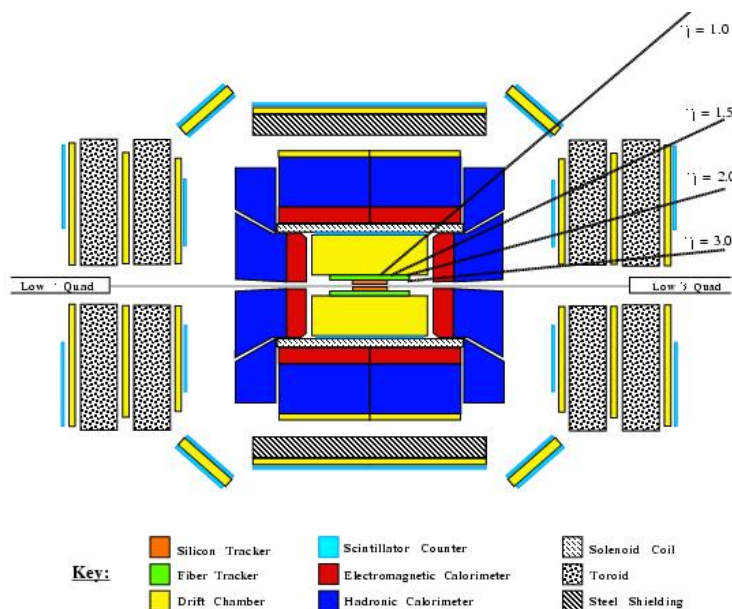


Some numbers about the structure:

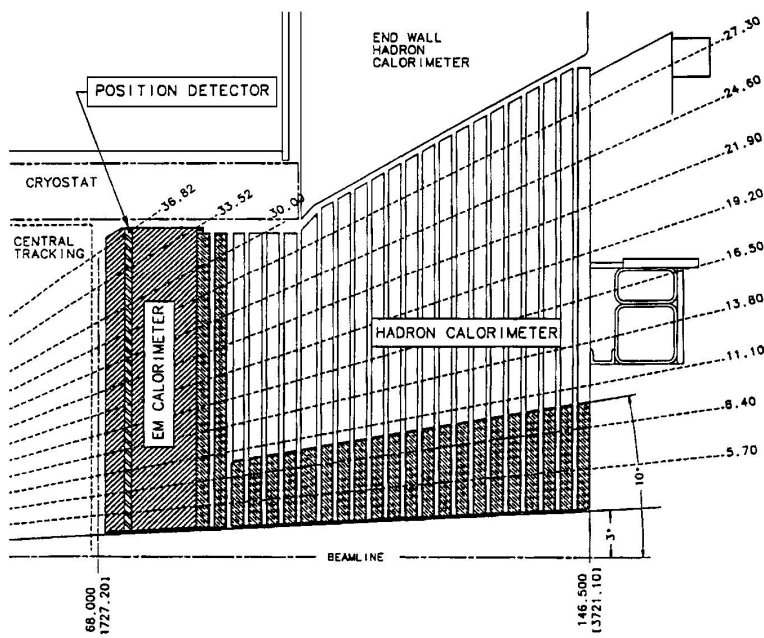
electromagnetic endcap calorimeter: 33 alternating layers of lead (3 mm) and scintillator (4 mm).

hadronic endcap calorimeter: 38 alternating layers of iron (25 mm) and scintillator (4 mm).

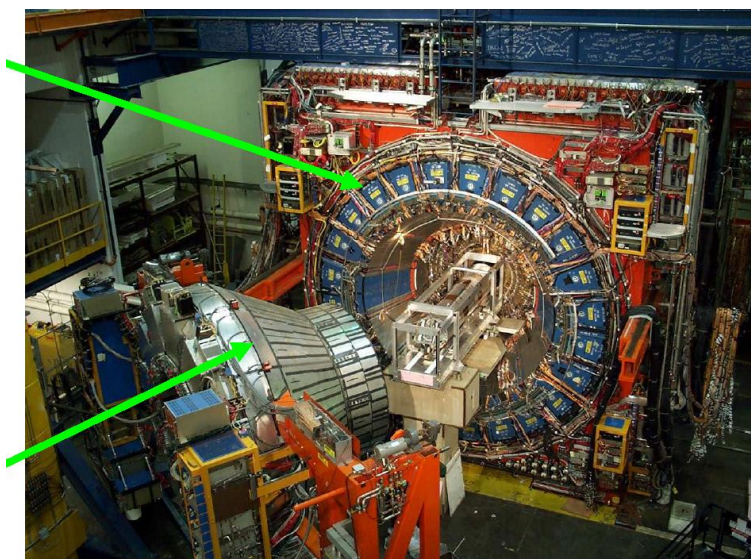
Also the **CDF** experiment



uses sampling calorimeters based on lead/iron and scintillators, both in the central and in the endcap regions, the latter is shown here:



The photo shows both parts:

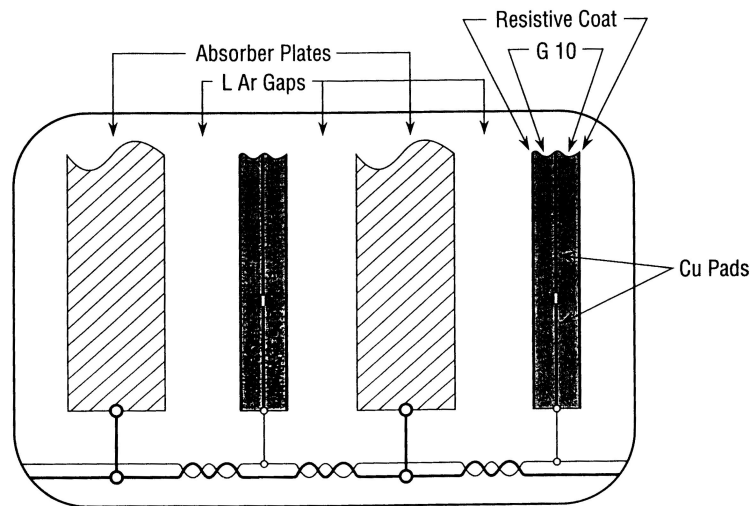


The light is collected by wavelength shifting plates and measured with PMs. In the endcap calorimeter wavelength shifting fibres are used (more on this technique see below, CMS).

Both the central and the endcap calorimeters have one position detector (chamber, scintillator strips) inserted where electromagnetic showers reach their maximum energy deposit, in order to separate π^0 's and single photons.

Note that the endcap calorimeter is new, the older version used chambers for the readout, but they were too slow for Tevatron run II.

The **D0** calorimeter is quite different from the detectors discussed so far: It uses the ionization in liquid argon. Principle:



The liquid argon gaps are only 2.3 mm thick. The electric field between absorber and signal boards (~ 2.5 kV) leads to electron drift times < 450 ns³ ($\approx \Delta t$ between bunch crossings!).

(Dis-)Advantages of this technique:

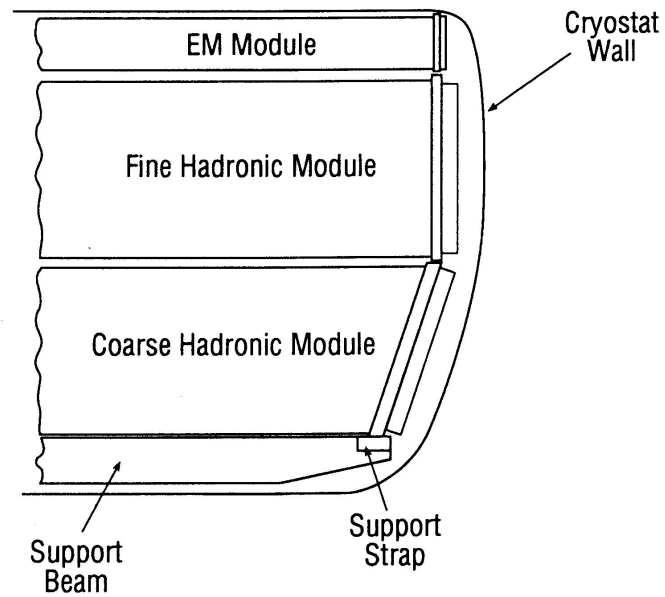
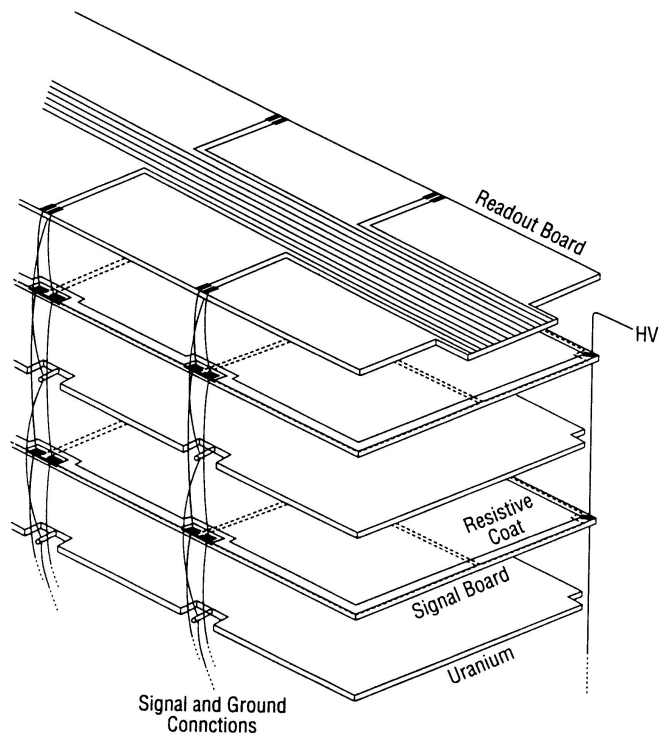
- + high number of electron-ion pairs $(5 \cdot 10^4/\text{MeV})^4 \rightarrow$ small fluctuations \rightarrow good energy resolution
- requires cryostat ($T < 87$ K)
- + excellent homogeneity and hermiticity
- + high granularity possible
- slow
- repair difficult
- + radiation hard

In principle one could use other liquids, either other noble gases or maybe substances which are liquid at room temperature. However, the latter ones require a very high purity (to avoid absorption of the electrons), which is technically difficult to achieve.

D0 calorimeter:

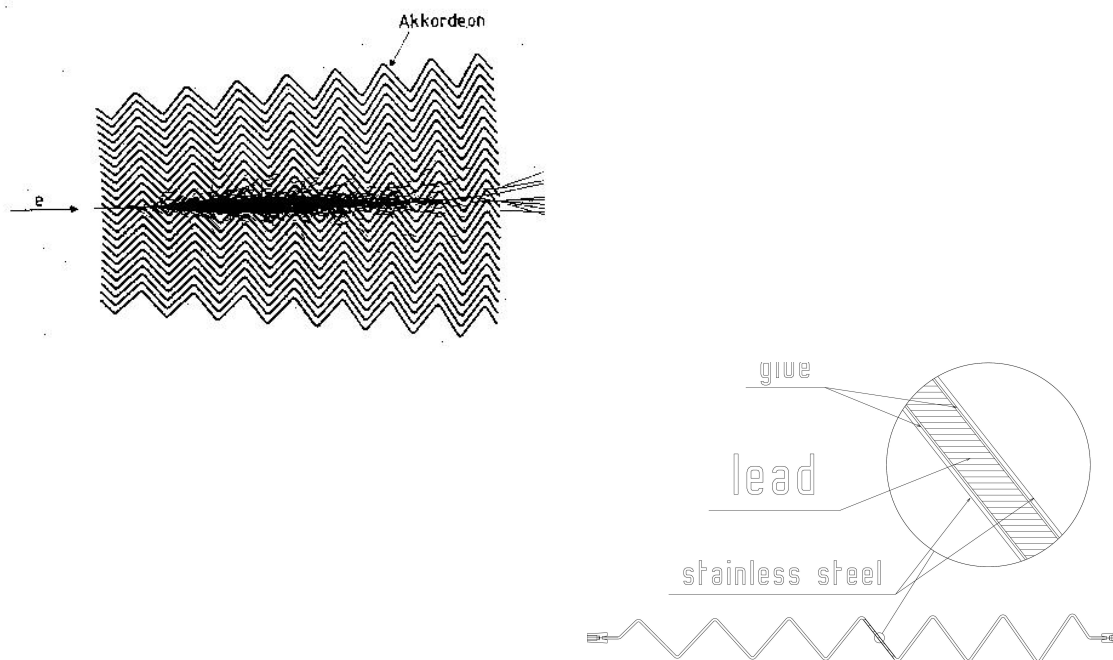
³scintillators: few ns!

⁴compare scintillators: 10^4 primary photons /MeV.



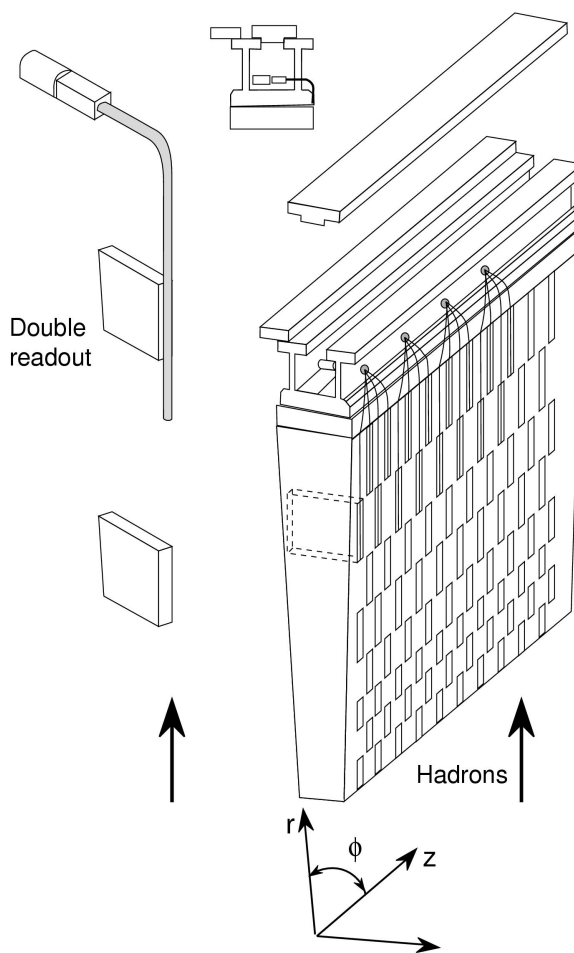
The electromagnetic and the first hadronic compartment are made out of uranium absorber, the coarse hadronic module uses copper and stainless steel.

Also the **ATLAS** electromagnetic calorimeter is of liquid Argon (LAr) type, with accordion geometry:



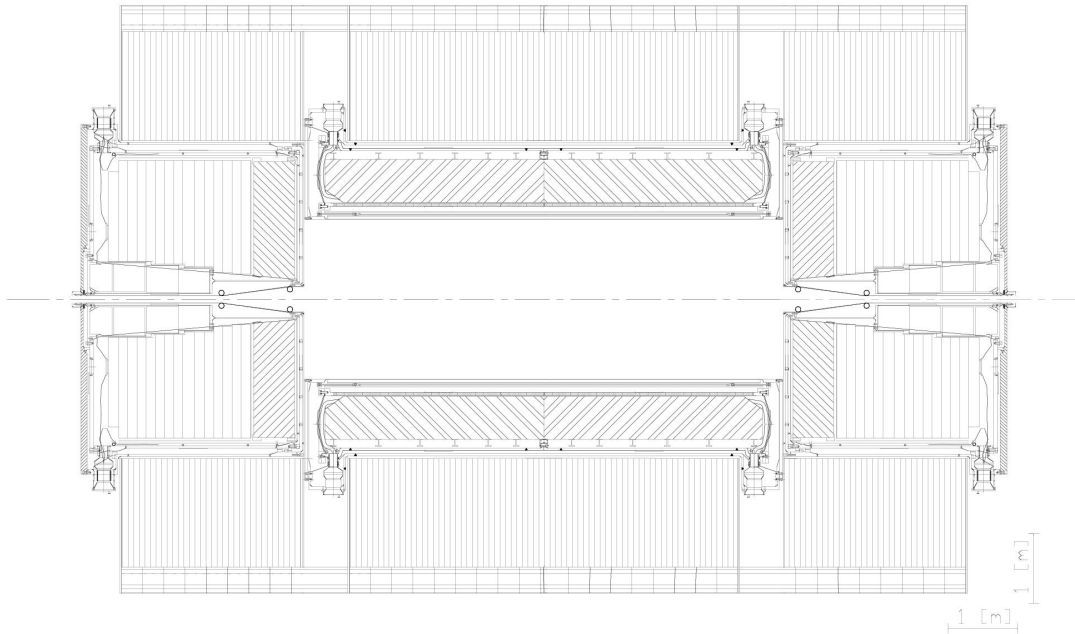
Absorber material is lead. The endcap hadron calorimeter is made of iron plates and LAr.

The barrel hadron calorimeter uses iron absorber plates (parallel to incoming particles) and scintillator plates, read out via wavelength shifting fibres and PMs:

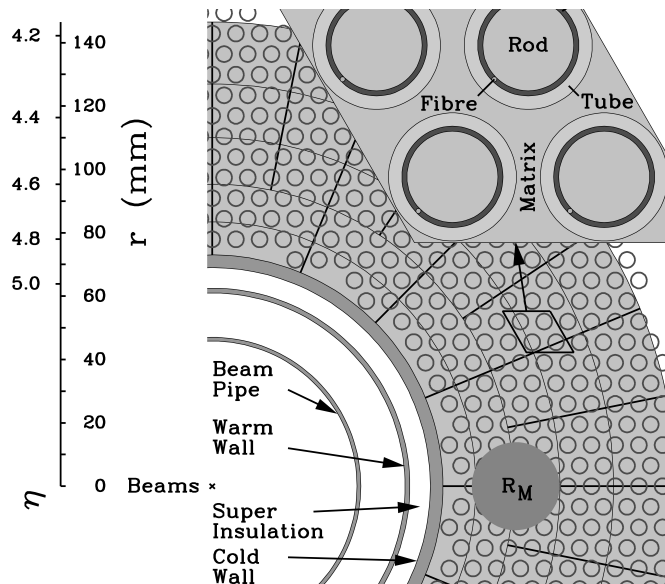


This is called a ‘tile calorimeter’; note that the incoming particles move parallel to the scintillator plates. The light yield is approximately 40 photoelectrons per GeV.

Global view of the ATLAS calorimeter:

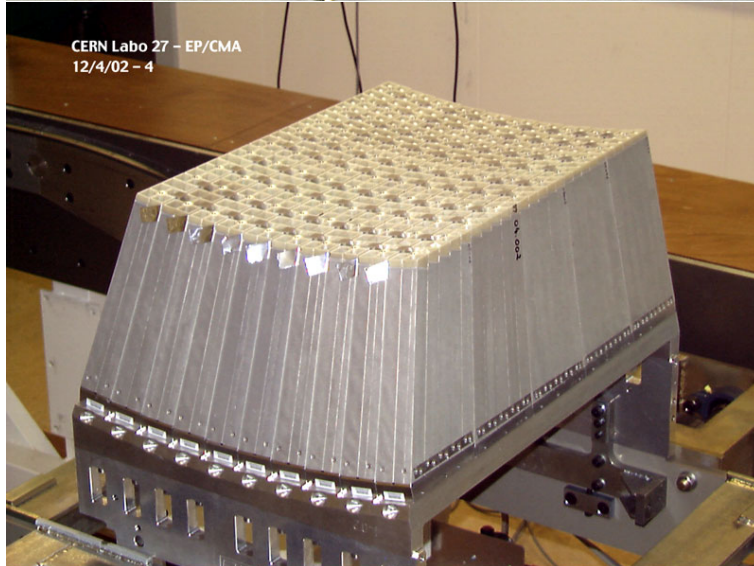
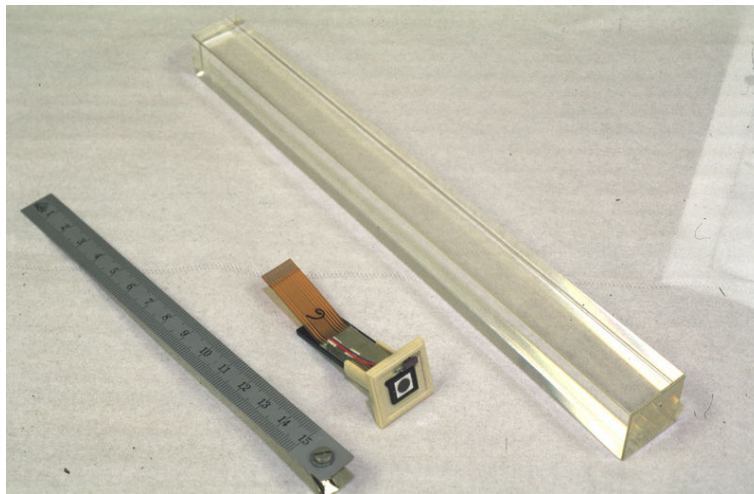
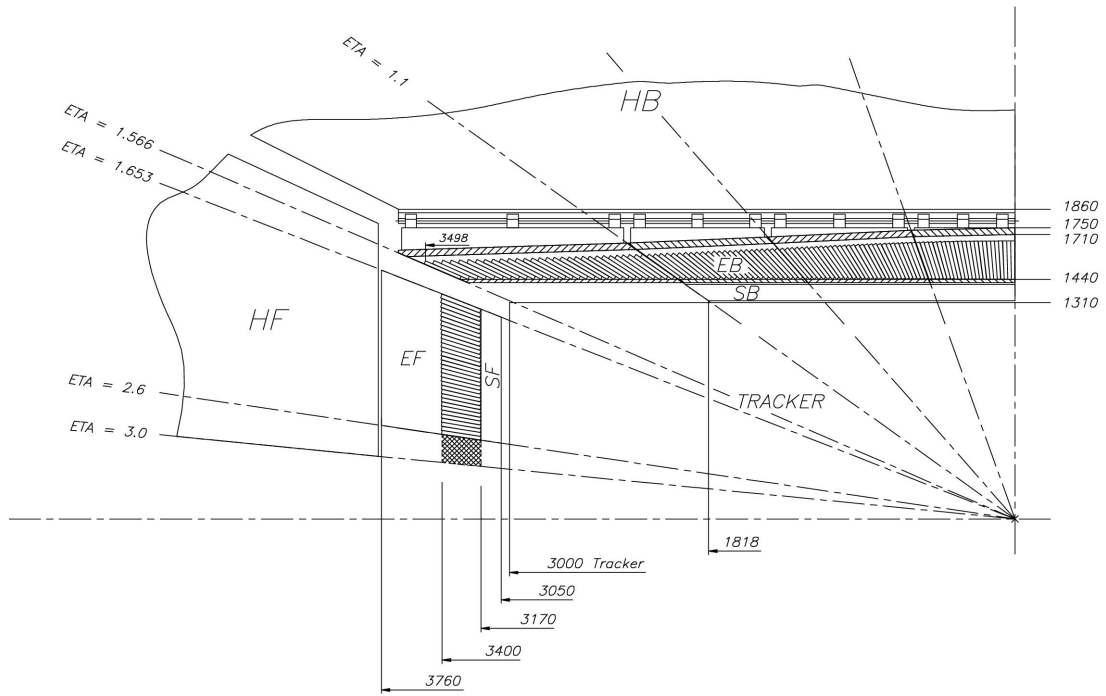


Near the beam pipe the forward calorimeter can be seen, which is also an LAr type detector, but of another geometry:



Only the small gaps between ‘rod’ and ‘tube’ are filled by Liquid Argon. Absorber Materials are copper (elm.) and tungsten alloy (hadr.). This calorimeter is compact and fast.

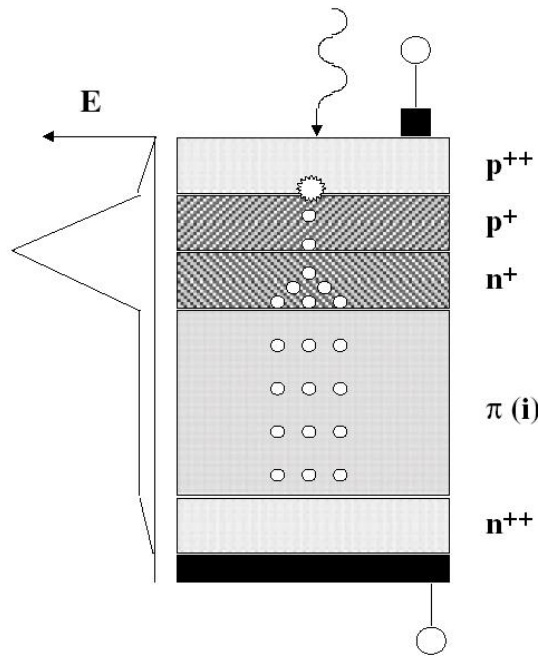
Quite different is the **CMS** electromagnetic calorimeter. It is *not* a sampling device built out of about 93,000 $PbWO_4$ crystals and thus allows for a very good energy resolution.



Lead-tungstate is a transparent scintillating material with a very short radiation length of **0.89 cm**, allowing for a very compact calorimeter (thickness $\sim 23\text{cm}$). The (dis)advantage of $PBWO_4$ compared to other suitable anorganic scintillators are:

- + small radiation length
- + radiation hardness
- + short decay constant (scintillation light pulse) $\sim 10\text{ ns}$
- light yield: $\sim 100\text{ photons /MeV}$

The latter disadvantage can be overcome by using novel photodetectors⁵ with a high quantum efficiency of $> 60\%$, ‘Avalanche PhotoDiodes’ (APD) (of which two are used per crystal):



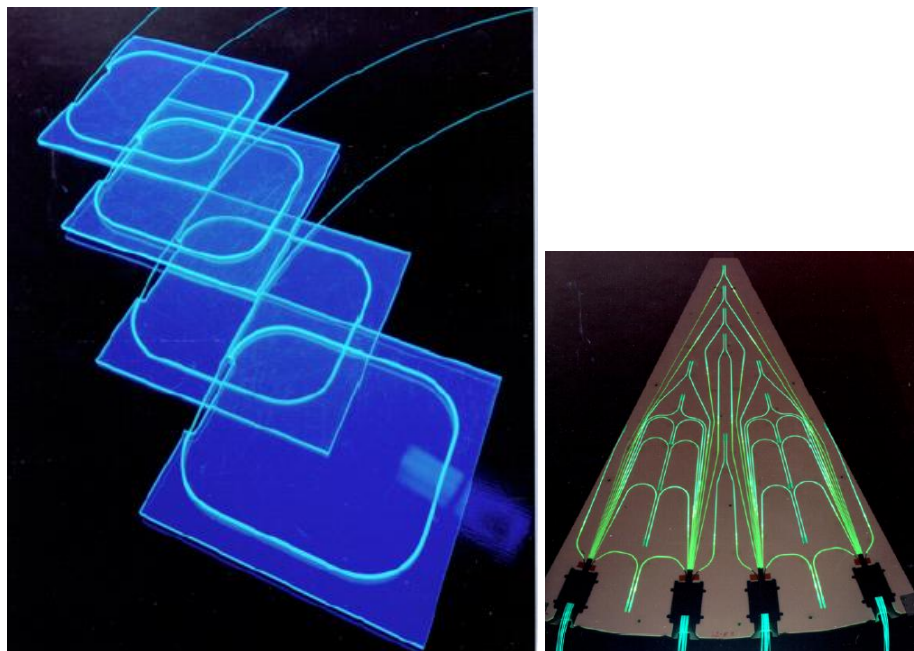
The strong magnetic field can not deteriorate the performance, since the detectors are very thin (first layer $< 100\mu\text{m}$).

Disadvantage of the crystal design: no longitudinal sampling (along shower axis)!

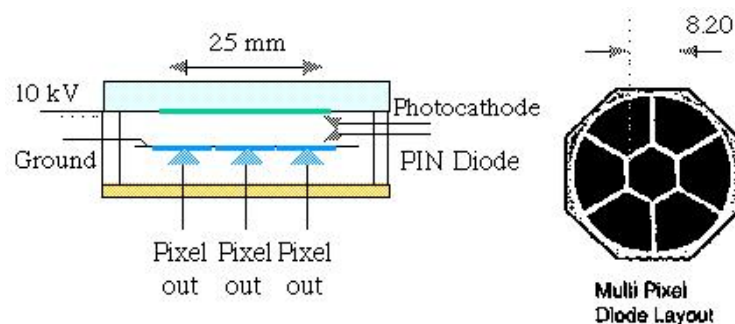
There is another important difference between the ATLAS and CMS calorimeters: In ATLAS the solenoid coil sits in front of the electromagnetic calorimeter, thus degrading the resolution, while in CMS both the elm. and hadr. calorimeters are inside the solenoid coil.

The CMS hadronic calorimeter is made of copper and scintillating tiles:

⁵barrel only; endcap: vacuum triodes

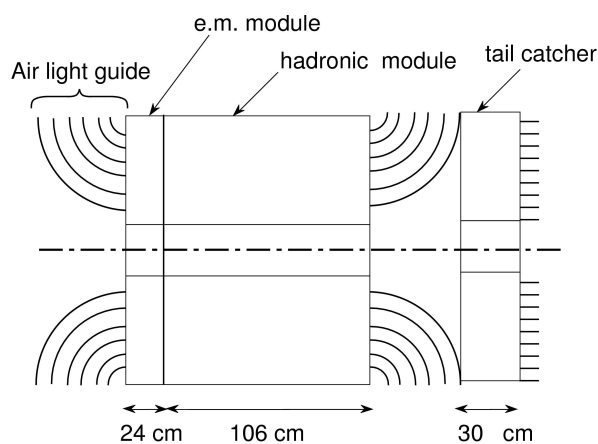


Advantage of this design: light extraction needs very little space ! As absorber material copper is used. The light is converted into an electrical signal with Hybrid PhotoDiodes (HPD's):



This combination of a thin (few millimeters) electrical field region and a silicon detector can operate in strong magnetic fields. The photocathode is segmented, so that one device can read out several fibres independently.

In addition to the barrel and endcap calorimeters there are forward hadron calorimeters made out of steel with quartz fibres, where *Cerenkov light* is generated. This detector is extremely radiation hard:



The light is read out via photo multipliers. Special: Cerenkov light is emitted only from ultra relativistic particles - so this detector 'sees' mainly electrons and is quite insensitive to hadronic 'background'.

Comparison of electromagnetic calorimeters:

detector	type	E-resol. <i>A</i>	E-resol. <i>C</i>	channels	long. sampling
UA1	scint	10%	2%	~ 1200 <i>PM</i>	4
UA2	scint	14%	~ 1%	~ 500 <i>PM</i>	1
CDF	scint	14%	< 1%?	~ 1000 <i>PM</i>	1
D0	LAr	15%	0.3%	~ 20000	4
ATLAS	LAr	10%	0.5%	~ 180000	3
CMS	<i>PBWO</i> ₄	6%	0.5%	~ 100000 <i>APD</i>	1

The angular resolution for both the ATLAS and the CMS central elm. calorimeters (incl. preshower) can be parametrised by

$$\sigma_{\theta} = \frac{0.05}{\sqrt{E/\text{GeV}}}$$

Comparison of hadronic calorimeters:

detector	type	E-resol. <i>A</i>	E-resol. <i>C</i>	channels	long. sampling
UA1	scint	~ 110%	?	1000 <i>PM</i>	1
UA2	scint	~ 100%	?	~ 1000 <i>PM</i>	2
CDF	scint	~ 50%	4%	~ 1400 <i>PM</i>	1
D0	LAr	50%	4%	~ 30000	4 – 6
ATLAS	scint	50%	2%	~ 10000 <i>PM</i>	3
CMS	scint	110%	5%	~ 20000 <i>HPD</i>	2

The resolution values are given for charged hadrons (pions). For jets (mixture of neutral hadrons (π^0) and charged hadrons) the energy resolution becomes somewhat worse - for most detectors.

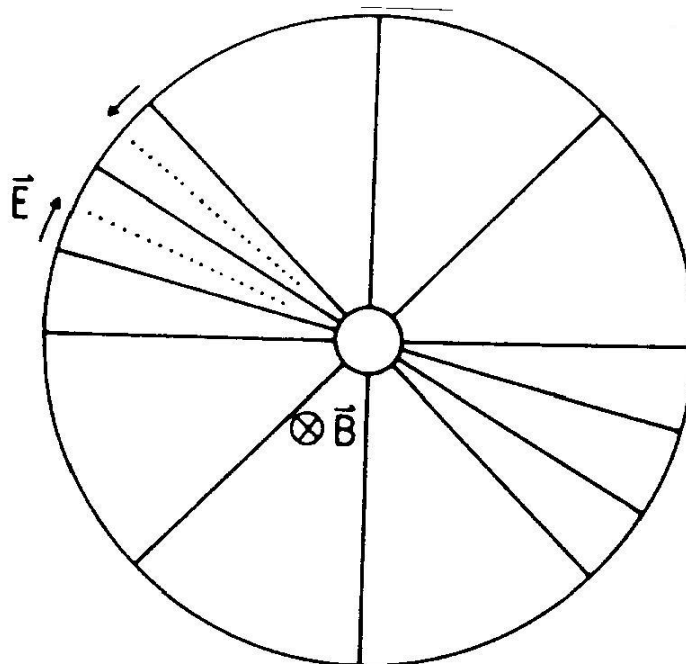
1.2.4. (Inner) tracking and vertexing

As we will see, mainly three types of tracking detectors are used:

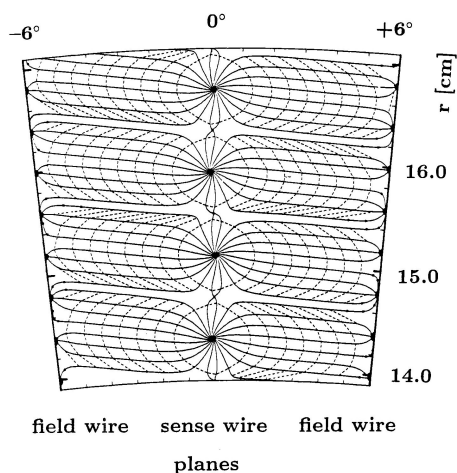
- drift chambers
- silicon strip and silicon pixel detectors
- scintillating fibres

Before we will discuss the different detectors in detail, some general comments on these devices:

Drift chambers inside solenoid magnets often look like this ‘jet chamber’:



The dots indicate long anode wires (> 1 m) parallel to the beam line, the thick straight lines are the cathodes. In addition there are field shaping wires, not shown. The drift lines are shown here:

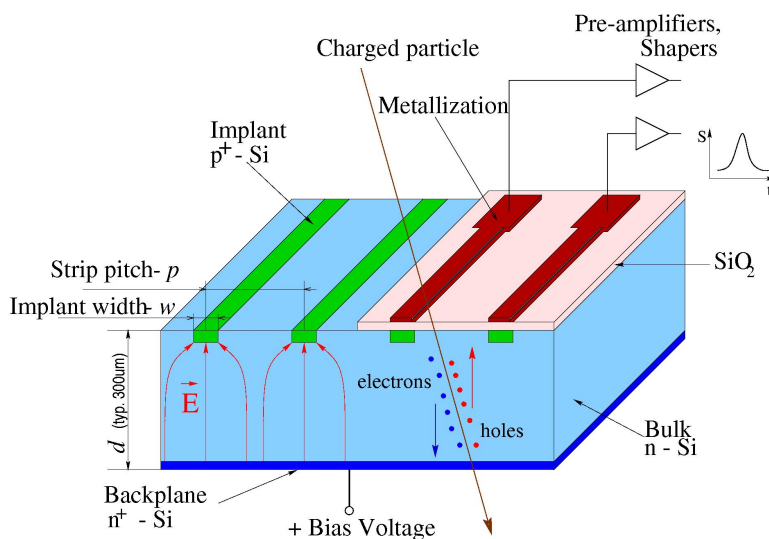


The number of anode wires fired by one particle from the interaction region varies between **30 . . . 300**. For each wire the drift time (relative to a fast external signal, for example generated by the accelerator for each bunch crossing) for the electrons to reach the amplification region is measured. This allows a precision of **50 – 200 μm** per wire, resulting in a sagitta resolution of few **10 μm** . If in addition to the drift time (TDC) also the pulse height is measured (ADC), a good dE/dx measurement can be performed, helping in identifying the particle (see below).

(Dis-)advantages:

- + standard technology
- + contains only a few percent of a radiation length of material (avoids showering)
- slow: drift distance / drift speed $\sim 50 \text{ mm} / 50 \text{ mm}/\mu\text{s} \sim 1 \mu\text{s}$
- pattern recognition difficult (if many tracks), occupancy high
- strong B field influences driftlines ('Lorentz angle' large)

Silicon strip detectors are semiconductors:

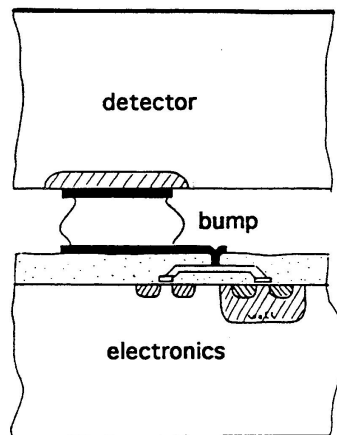


The material is typically $300\ \mu\text{m}$ thick, the strips $10 - 50\ \mu\text{m}$ apart and a couple of cm long. The voltage across the diode (strip versus backplane) is chosen such that there are no free charges inside the detector (as long as there is no particle traversing), the device is fully depleted. A minimum ionizing particle generates about 30000 electrons and holes. Typically 4-10 layers are used to measure a track.

(Dis-)advantages:

- + high spatial resolution $\sim 10\ \mu\text{m}$ (combining charge from neighboring strips)
- expensive
- detector contains up to one radiation length of material (\rightarrow showering)
- + fast: charge collection $\sim 20\ \text{ns}$
- limited radiation hardness ($\rightarrow T < -10^0\ \text{C}$)

Silicon pixel detectors have a typical pixel size of only $200\ \mu\text{m} \cdot 20\ \mu\text{m}$; each pixel has its own readout electronics:

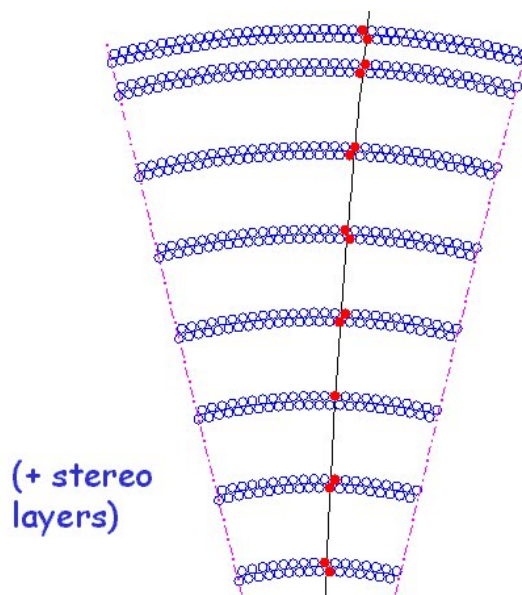


Pixel detectors are used as ‘vertex detectors’ close to the beam pipe.

(Dis-)advantages:

- + 3 D track reconstruction
- + high spatial resolution
- many channels \rightarrow expensive
- + many channels \rightarrow low occupancy
- + fast: charge collection $\sim 20\ \text{ns}$
- limited radiation hardness

Scintillating fibres allow a fast measurement in the $x - y$ plane:

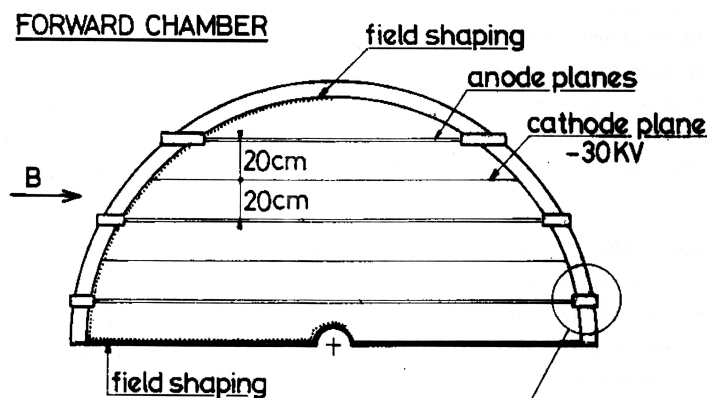


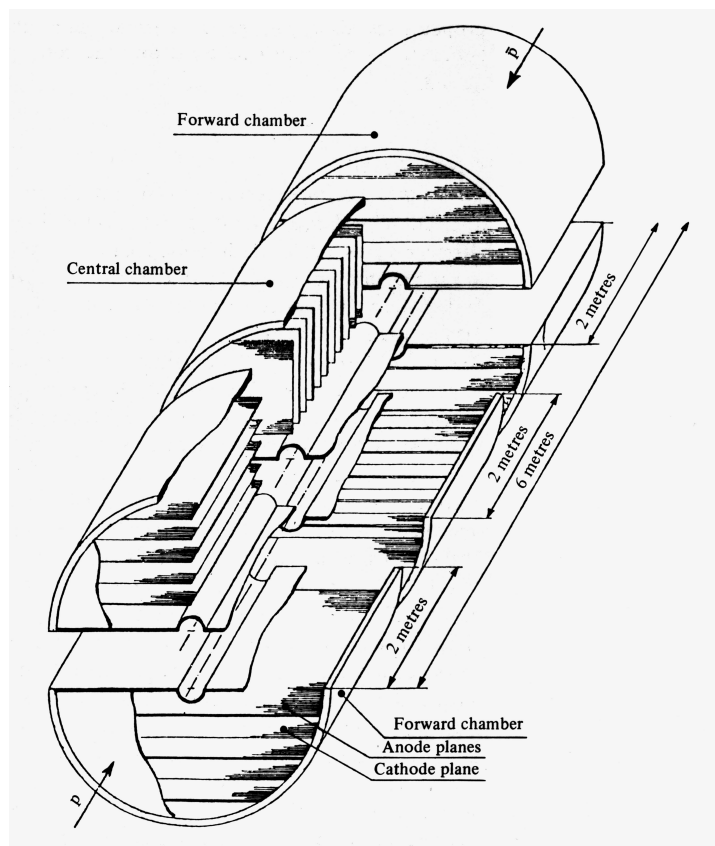
The fibres are typically 1 mm thick and 1 m long; they are strung parallel to the beam axis. The scintillating light can be measured with photomultipliers.

(Dis-)advantages:

- + fast, decay time = few ns
- z -coordinate (along beam axis) difficult to measure
- pattern recognition difficult (if many tracks), occupancy high
- light yield low (~ 10 photons per track !)

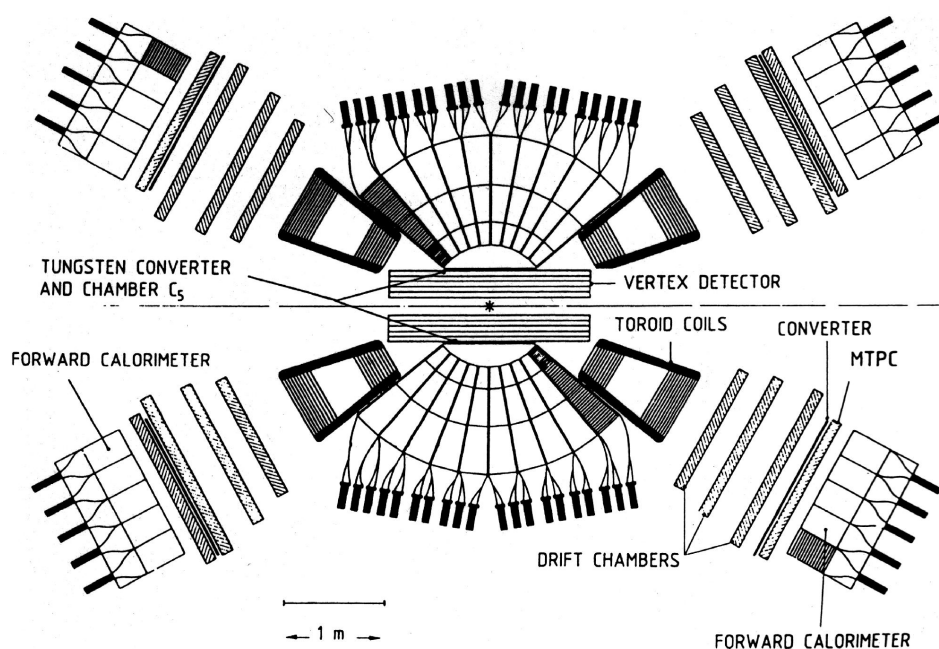
The large central detector ($r = 1.3$ m) of the **UA1** experiment was made of planar drift chambers, oriented such that the particles from the interaction point fly approximately parallel to those planes. Every second plane is a cathode plane; in the forward region:



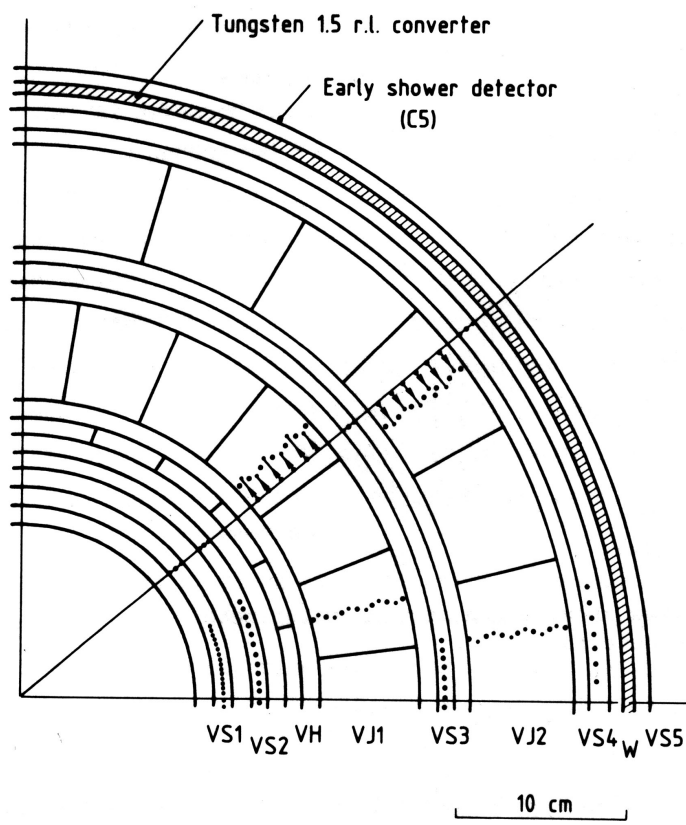


The magnetic dipole field causes up- and forward-going tracks to be bent in a direction perpendicular to the wire planes - thus the momentum can be measured easily. The electrons created by ionisation have to drift up to 20 cm. Each anode wire plane contains about 200 (350) wires in the central (forward) region, 5 mm apart, measuring the track with an accuracy of $\sigma = 250 \mu\text{m}$ per wire. The pulse height is measured, too. The coordinate along the wires (up to 2.2 m long) is determined from the ratio of the pulse heights measured at the two ends with a precision of 1% of the wire length. The sum of the pulse heights is proportional to dE/dx .

The **UA2 apparatus** looked like this (at the time of W/Z discovery):



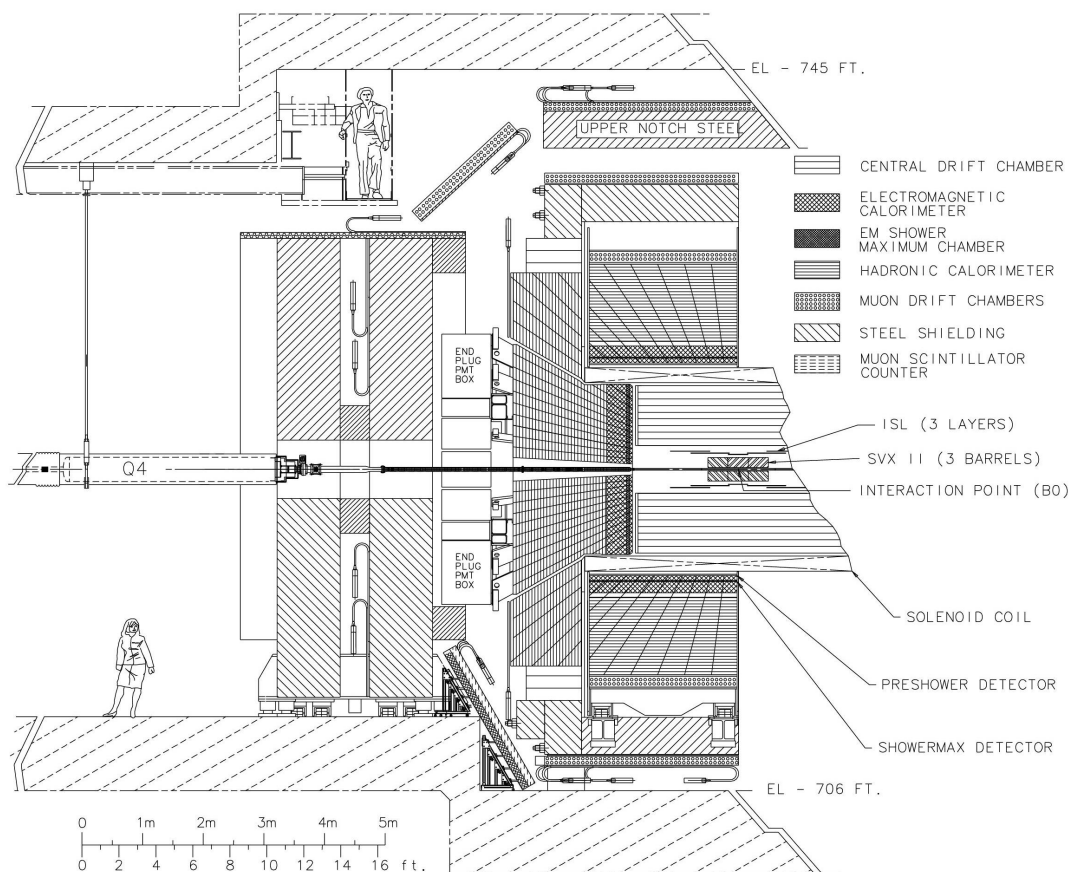
This was one of the first detectors calling its inner tracker a 'vertex detector', a cylindrical chamber:



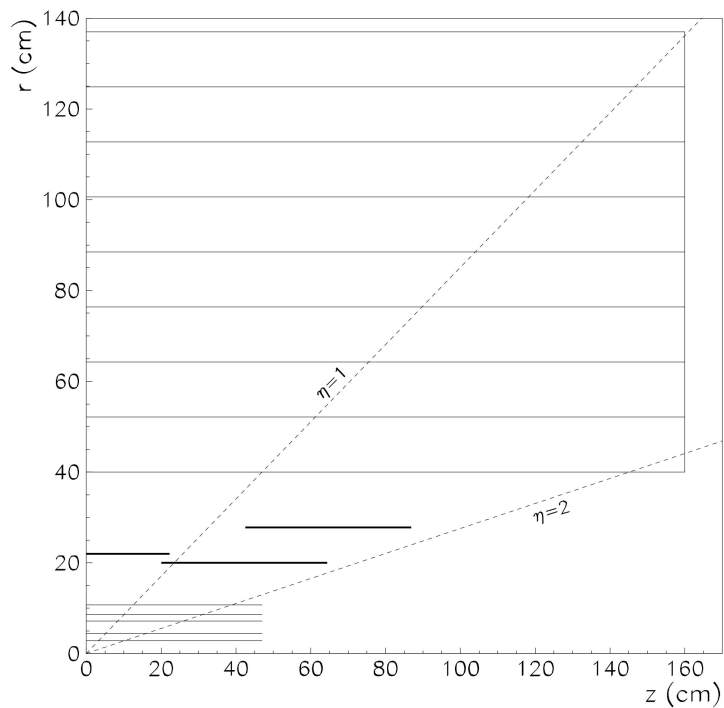
They consisted of drift chambers of 'jet' type (VJ1,VJ2) with a resolution of $300 \mu\text{m}$ per wire, proportional chambers with cathode strip readout (allows to measure z !) and a layer of scintillators (VH). Charge division was (also) used to determine the z coordinate. Along the beam axis the vertex could be localized with a precision of 1.5 mm; measurements of decay lengths (lifetimes) of short-lived particles were not possible.

The z vertex coordinate must be known to determine particle momenta, which was possible only in the forward (backward) regions, equipped with a toroidal field. The main goal at that time was to verify that the W bosons are polarized (positive electrons from W decays fly preferentially in the direction of the proton beam). After traversing the B field, the tracks were measured with several layers of drift- and proportional chambers. A momentum resolution of $0.5\% \cdot p/\text{GeV}$ was reached. Later the toroids and chambers were removed, in favor of a good endcap calorimeter.

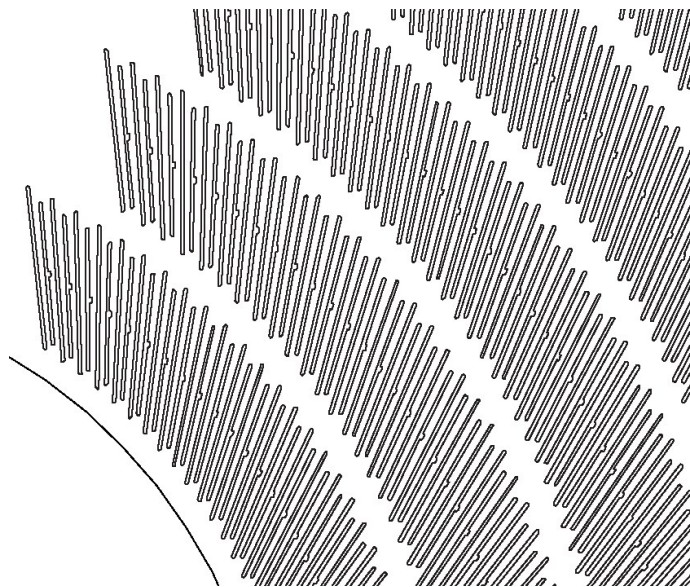
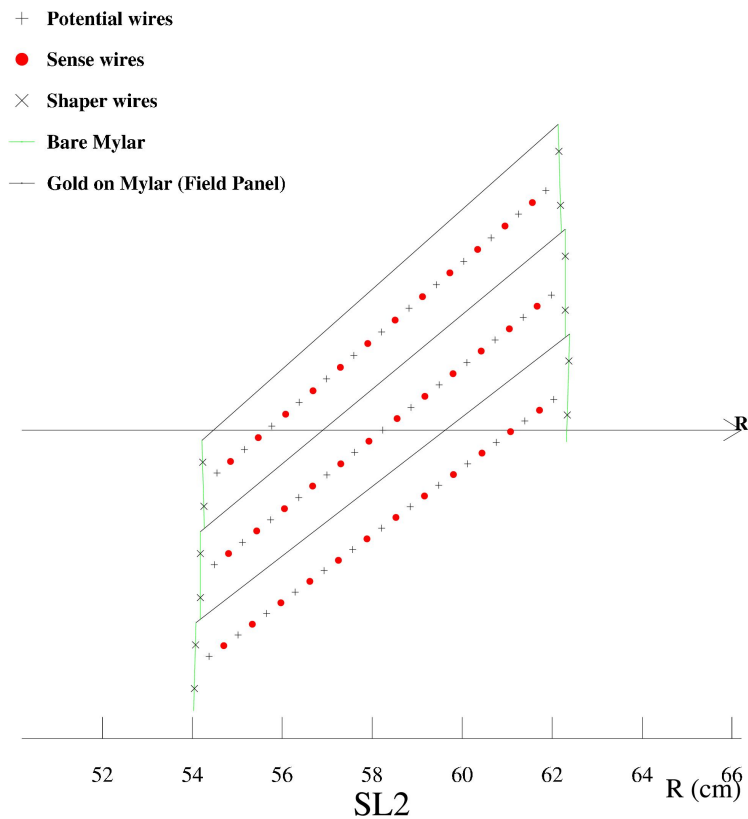
CDF got a new central tracker (shorter drift times!) and a new silicon vertex detector for the run II data period:



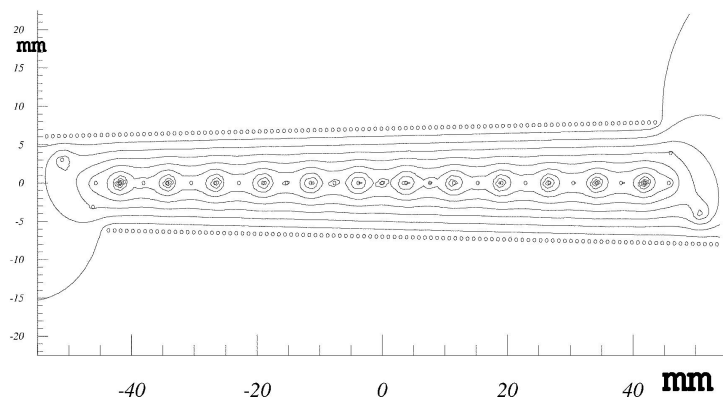
The tracker consists of three parts:



The ‘central outer tracker’ (COT) is a **3 m** long drift chamber with short drift distances of less than **1 cm** and a ‘fast’ gas (Ar Et CF₄, $\sim 100 \text{ mm}/\mu\text{s}$), so that the maximum drift time is below **132 ns** as (originally) required for run IIb. The chamber radius is large, approximately **1.4 m**, allowing for a good momentum resolution (**$B^2!$**). The 60000 wires (half of them sense wires) are strung this way:



Advantage of this layout: tracks from vertex cross ‘supercells’ under a large angle, thus avoiding left-right ambiguities. The electric field lines are shown here:

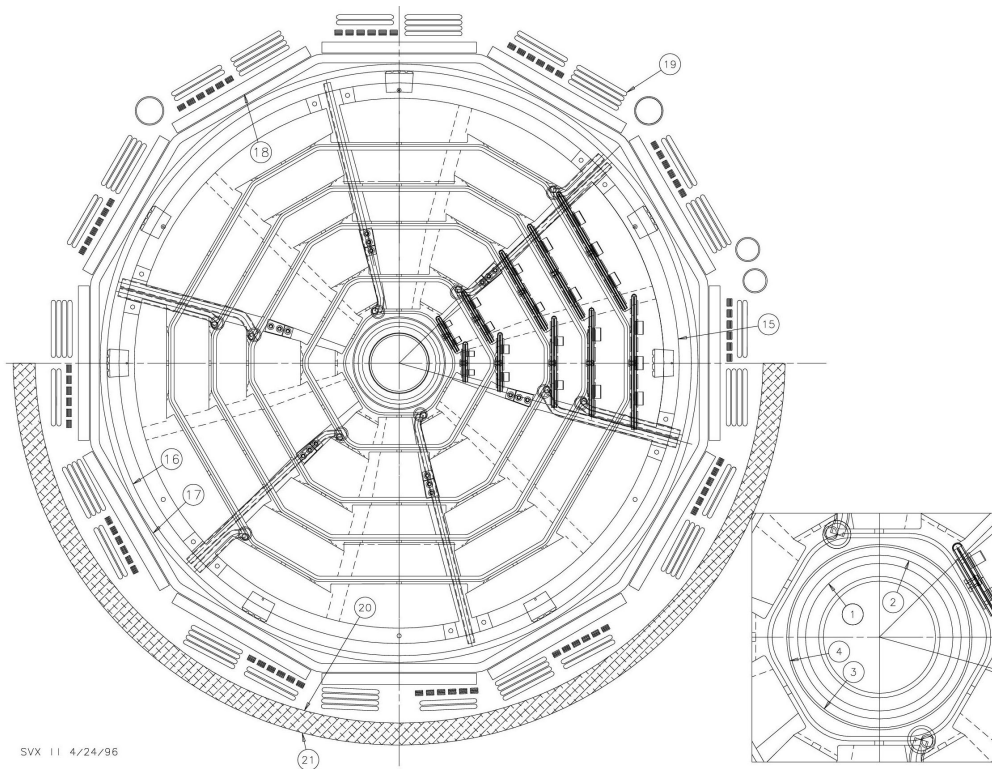


Note that the 'lines' of field wires are realized by gold plated mylar foils, thus simplifying the design. The position resolution is around $180 \mu\text{m}$ per signal wire.

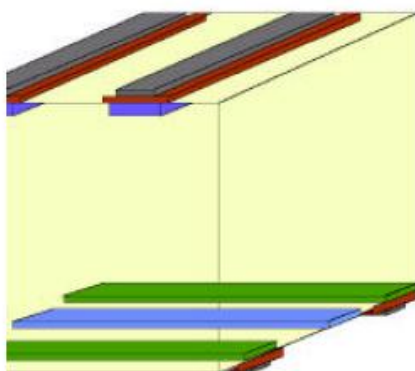
The electronics allows apart from the arrival time measurement also a determination of pulse heights; for a total of 96 layers this gives a decent dE/dx measurement.

In between the COT and inner silicon detector another silicon device (with a moderate resolution), the ISL (Intermediate Silicon Layers) was inserted; it provides a tracking point allowing to match the COT and inner silicon tracks.

The CDF silicon detector has five layers



In total 5 double sided layers are 'seen' by a traversing particle:



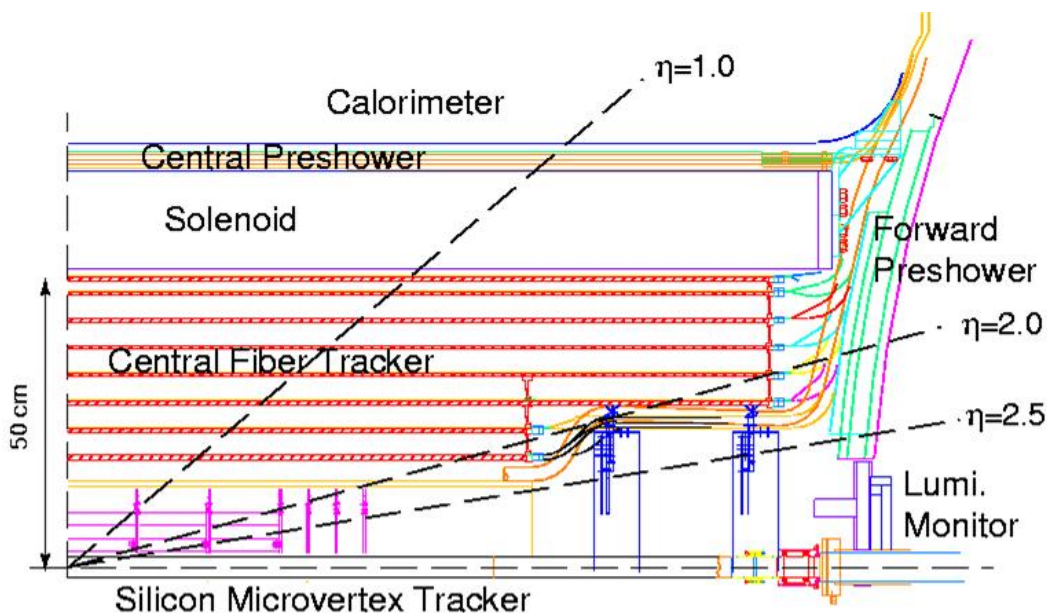
Only barrel modules with Si strips parallel to the beam axis¹ and strips measuring in the $x - y$ plane are used, there are no ‘endcaps’ (cf D0!). The layers are positioned at radii between 2.5 cm and 11 cm. In addition a ‘layer 00’ Si detector is mounted directly on the beam pipe, at a radius of ≈ 1.5 cm, where it has to stand 10 kGy/fb. To increase the lifetime these strips are operated at 0° C.

Using all inner tracking devices together, a momentum resolution of

$$\frac{\Delta p_T}{p_T} = 0.001 \cdot p_T/\text{GeV} \quad (1)$$

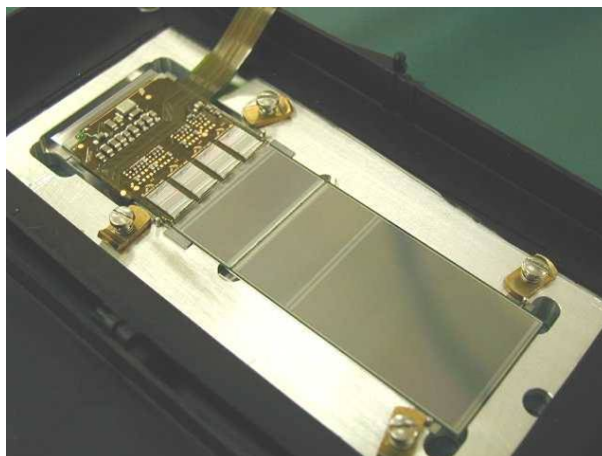
can be reached.

D0 has no drift chamber, due to the limited space inside the solenoid coil (determined by the calorimeter size...):



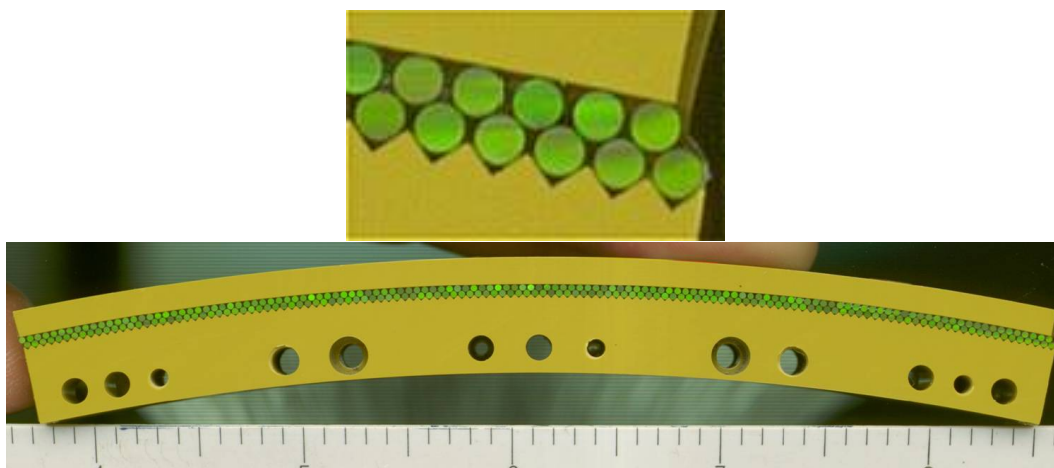
The ‘barrel’ shaped silicon modules are complemented by disk like modules, some in the end regions, others close to the vertex. Other parameters are similar to those of the CDF Si tracker. A barrel ‘ladder’ is about 12 cm long and looks like this:

¹ $\pm 1.2^\circ$ stereo angle

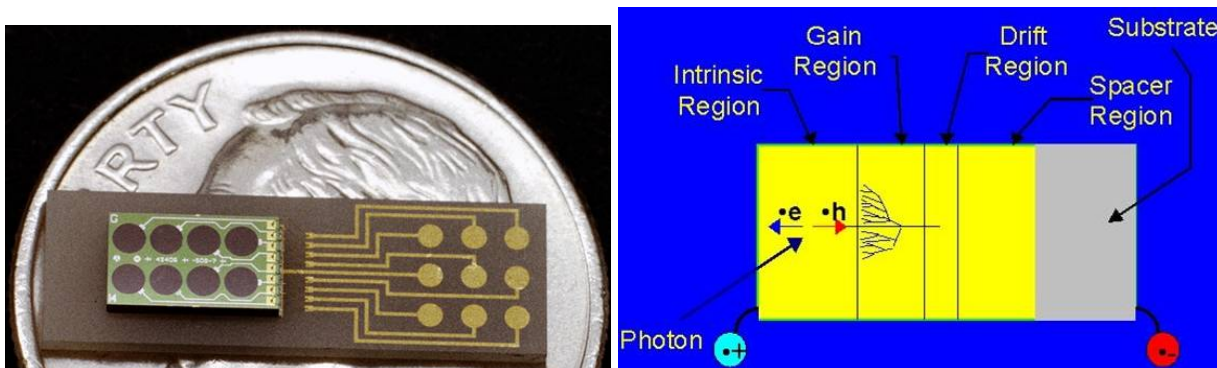


Both single sided and double sided modules are used.

Unique is the scintillating fibre tracker with ‘VLPC’ readout surrounding the silicon tracker:



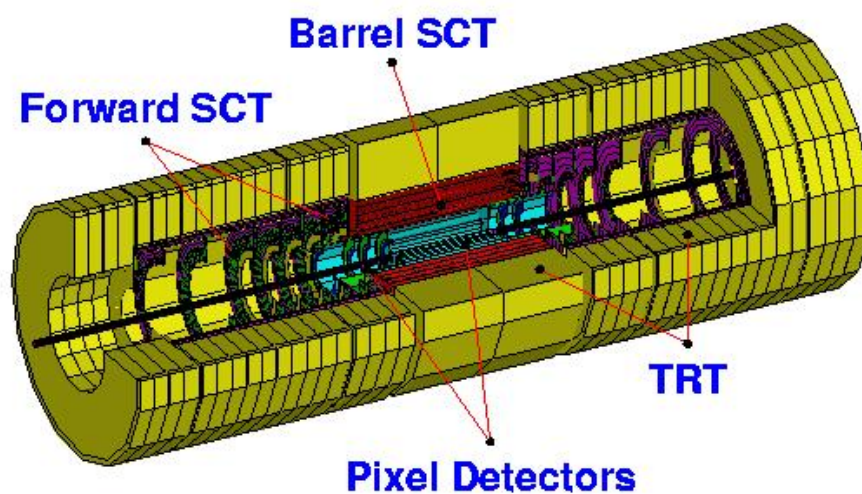
The fibres are 2.5 m long and 0.835 mm thick; a minimal ionising particle produces results in about 10 photons arriving via clear fibres at the photon detectors, the ‘Visible Light Photon Counters’. These are semiconductor detectors operating at a temperature of $T \approx 9 \text{ K}$, reaching a quantum efficiency of 75%:



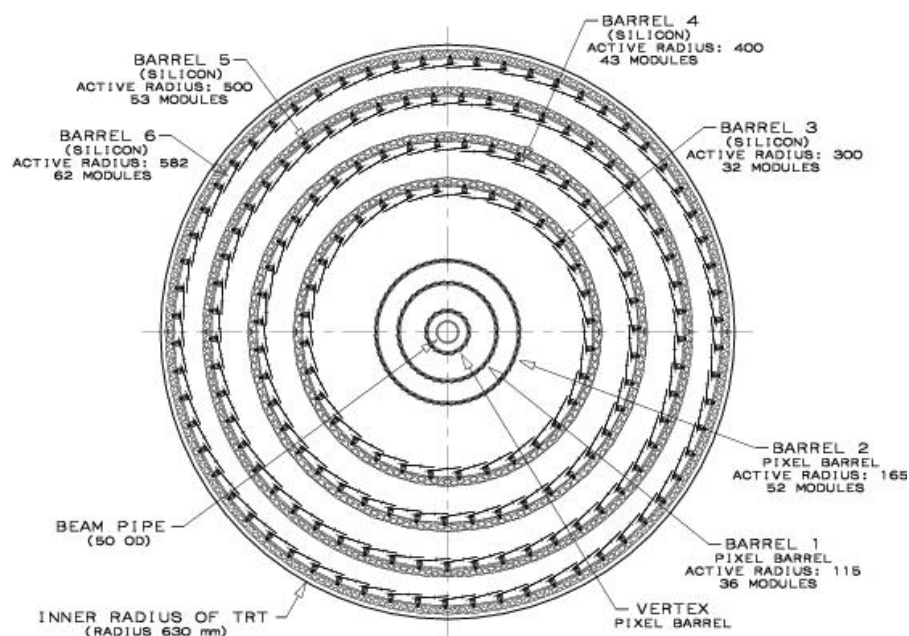
Due to the limited tracker radius, the p_T resolution is not quite as good as for CDF:

$$\frac{\Delta p_T}{p_T} = 0.002 \cdot p_T / \text{GeV} \quad (2)$$

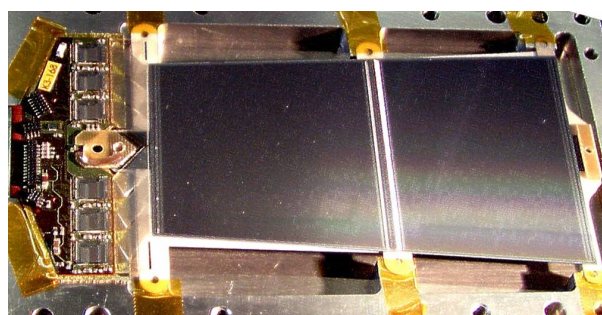
ATLAS uses a combination of silicon trackers and gas detectors to measure tracks:



Here two types of silicon devices are used, pixels and strips:



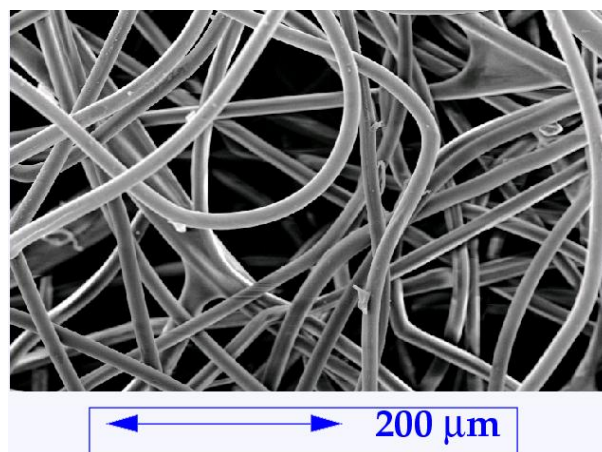
The silicon strip detector is similar to the one used in CDF. Double sided modules are used in both the barrel and endcap regions:



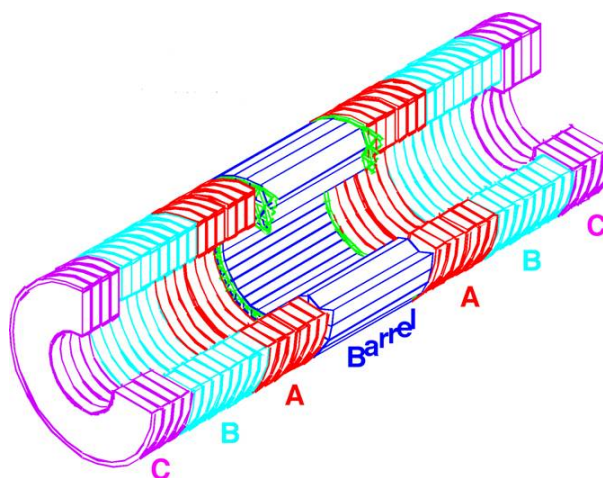
In total an area of 61 m^2 is covered, the resolution is typically $15 \mu\text{m}$. A particle at $\eta \approx 0$ traverses four layers. The temperature will be kept at -10^0 C .

The pixel detector covers the innermost region; the inner of the three barrels is located at a distance of 5 cm from the beam line. There are in total 80 million pixels with a size of $50\mu\text{m} \cdot 300\mu\text{m}$.

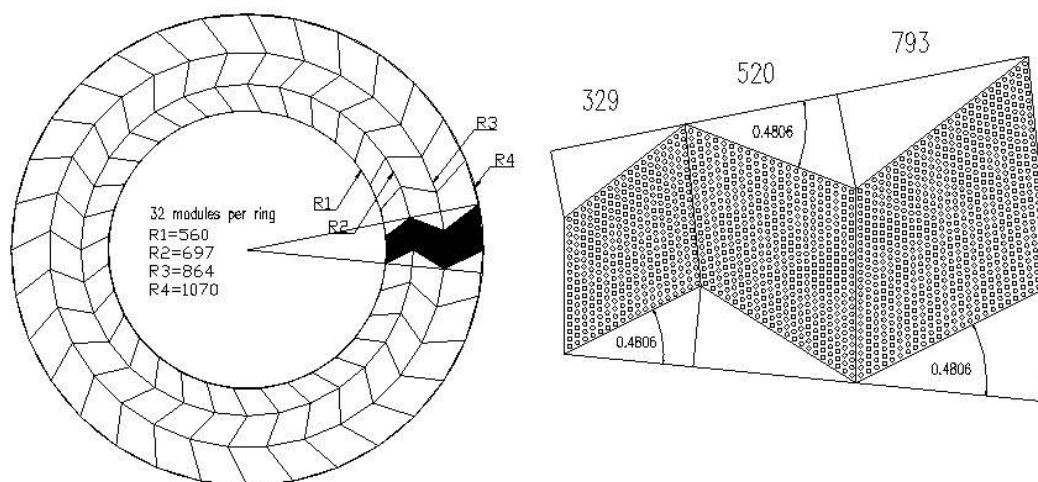
The outer part of the inner tracker, made out of barrel and endcap disks, consists of straw tubes together with a ‘radiator’ material with a huge effective surface, thus yielding a measurable amount of transition radiation:



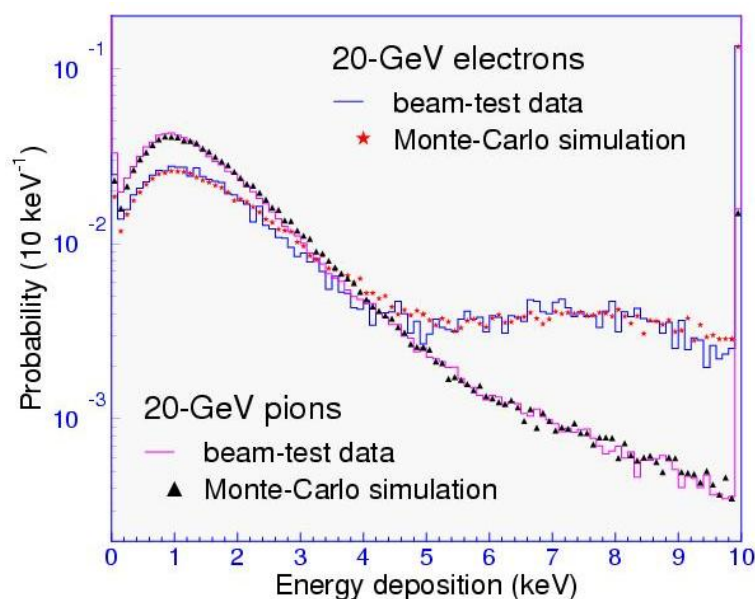
This ‘Transition radiation Tracker’ (TRT) encloses the silicon tracker; in the central region the tubes are oriented along the beam axis, in the forward regions they run radially:



The tubes are $39 - 144 \text{ cm}$ long and have a diameter of less than 1 cm . The straw walls are made out of different (conducting) synthetic materials, with a total thickness of only $70\mu\text{m}$. Due to the small diameter the drift time is short, around 40 ns . The position resolution will be around $150 \mu\text{m}$. A particle produced at the collision point will traverse at least 36 straws. The loosely packed radiator material is inserted in between the tubes:



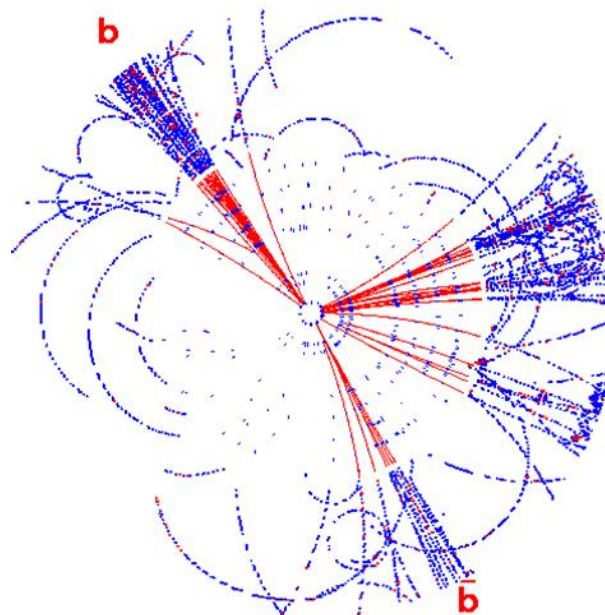
Transition radiation occurs at the surfaces; the probability is proportional to $\alpha \approx 1/137$, thus small. The (average) amount of light is proportional to γ of the charged particle flying through. Therefore a measurable effect can be expected only for electrons. Most TR photons will be able to traverse the polyethylene radiator and also the straw walls. Inside the tubes the photons are absorbed in the gas: 70% Xe ($Z = 54$), 20% CF_4 , 10% CO_2 . The corresponding energy deposits of about 5 keV adds to the charged particle's energy loss of about 2keV per tube. Thus electrons can be identified:



In spite of the radiator material the construction is very 'light', at $\eta = 0$ the whole TRT detector represents only 15% of a radiation length.

A simulated ATLAS event (inner tracker only) looks like this:

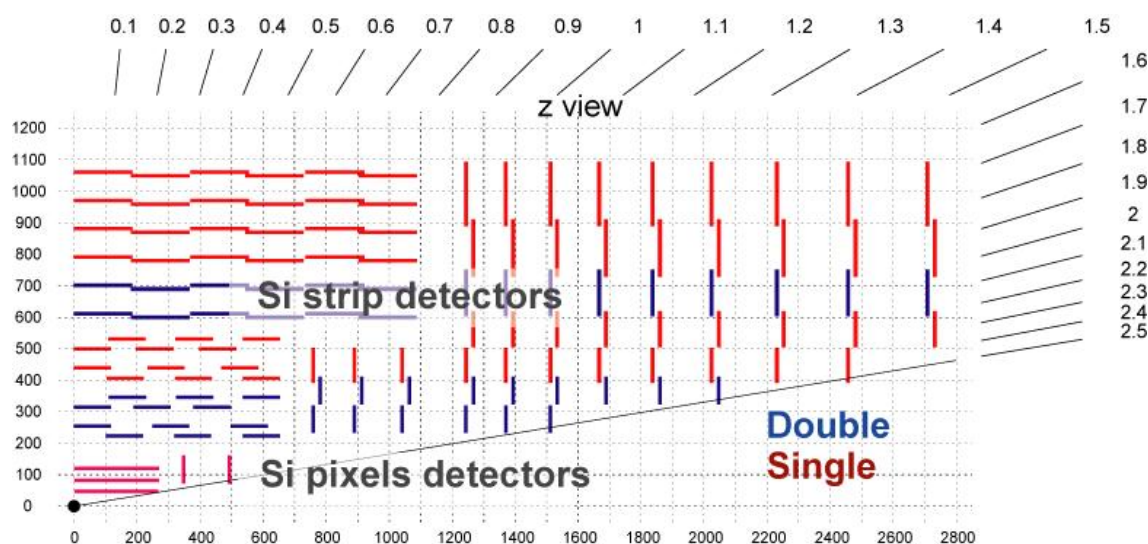
ATLAS Barrel Inner Detector
 $H \rightarrow b\bar{b}$



One can clearly see the different spatial resolutions achieved in the silicon and TRT parts.

CMS has an only-silicon inner tracker; the strip detector will have a total surface of 220 m^2 = world record.

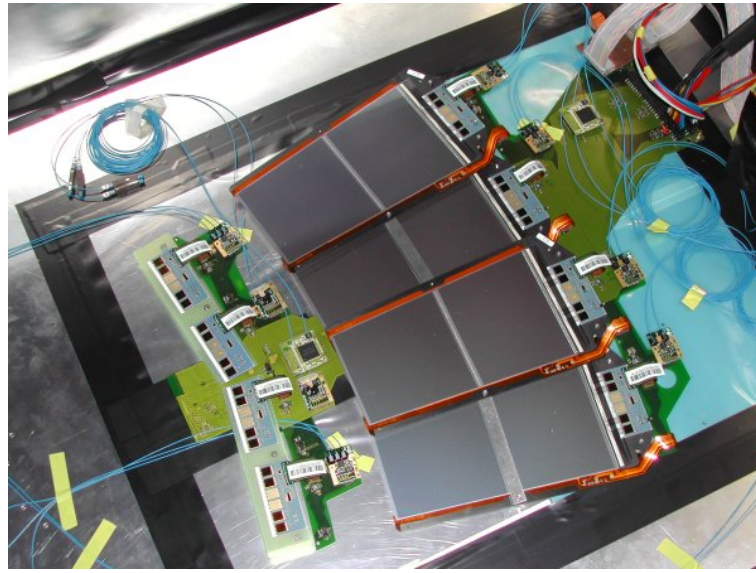
In the barrel region it is made out of 2 pixel layers and 10 strip layers.



The layout of the CMS inner tracker

The total length amounts to more than 5 m, the radius exceeds 1 m.

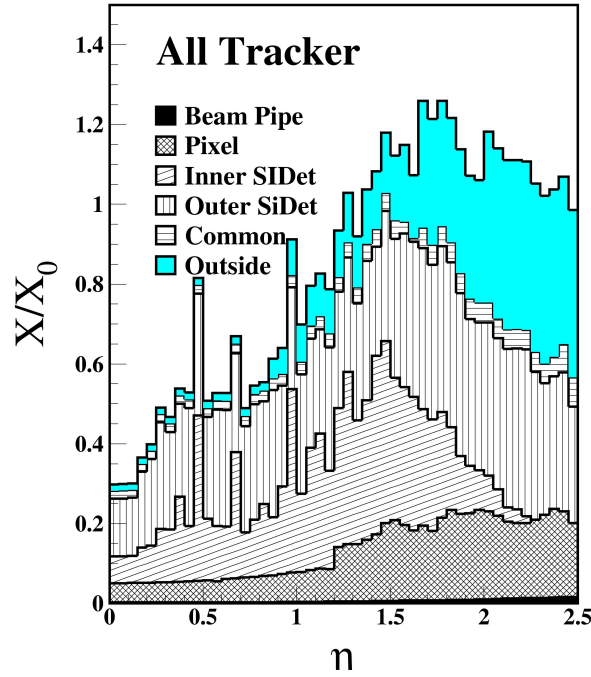
A silicon strip ‘petal’ in the endcap region:



Result of a test assembly:



A problem is the material thickness (represented by the beam pipe, tracking detectors, infrastructure) in front of the calorimeter:



This can lead to showering inside the silicon tracker. The situation is even worse for ATLAS, reaching $2 X_0$ at $\eta = 0$.

Let's now take the CMS silicon strip tracker as an example to estimate the momentum resolution from the position resolution and the magnetic field strength.

A track at $\eta = 0$ traverses 10 silicon strip layers in between $r = 20$ cm and $r = 100$ cm with a resolution in the $r - \phi$ plane of $15 \mu\text{m}$ each. The magnetic field strength is $B = 4$ T. Thus, approximating the 10 layers by the 4 detector model discussed in chapter 1.2.1, using a resolution of $\Delta y = 15 \mu\text{m} / \sqrt{2.5} = 9 \mu\text{m}$:

$$c_{det} = 0.026 \cdot \frac{9 \mu\text{m}/\text{mm}}{(0.8 \text{ m})^2/\text{m}^2 (4 \text{ T})/\text{T}} \approx 1.0 \cdot 10^{-4} \quad (3)$$

We can also estimate the multiple scattering effect, reading the value $L = 0.3 X_0$ from the figure shown above:

$$c_{MS} = \frac{0.052}{0.8 \text{ m/m} 4 \text{ T/T}} \sqrt{0.3} \approx 1.0 \cdot 10^{-2} \quad (4)$$

Thus, a 100 GeV track will be measured with a precision of

$$\frac{\Delta p}{p} = 10^{-4} \cdot \frac{p}{\text{GeV}} \oplus 1\% = 1\% \oplus 1\% = 1.4\% \quad (5)$$

This number is in good agreement with the outcome of CMS MC studies. The inclusion of the silicon pixels will improve this figure slightly.

Comparison of trackers:

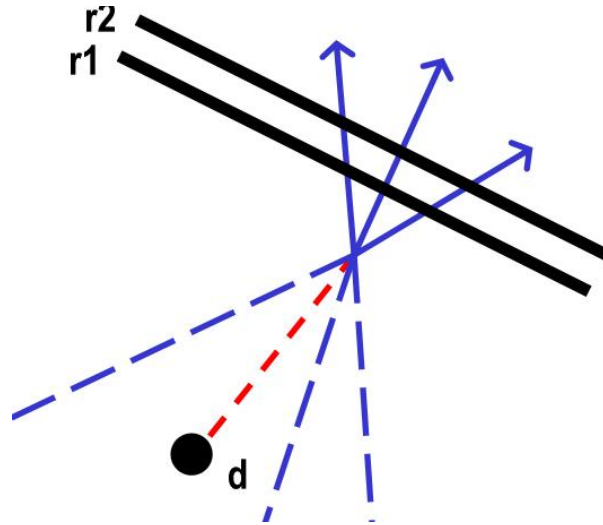
detector	type	pos. resol. ($R\phi$) / μm	mom.-resol. ($\eta = 0, 100\text{ GeV}$)	channels
UA1	drift	250	30%	6100
UA2	drift/prop	300	50%	?
CDF	silicon strip	7-11		700000
CDF	drift	180	10% total	30000
D0	silicon	10		800000
D0	fibres	100 (doublet)	20% total	80000
ATLAS	pixel	14		$1.4 \cdot 10^8$
ATLAS	silicon strip	15		$3 \cdot 10^6$
ATLAS	straw	150	4% total	400000
CMS	pixel	10		$5 \cdot 10^7$
CMS	silicon strip	15	1.6% total	10^7

Important is also the impact parameter resolution. For ATLAS it can be parametrized by

$$\delta d = 12 \mu\text{m} \oplus \frac{88 \mu\text{m}}{p_T/\text{GeV} \sqrt{\sin \theta}} \quad (6)$$

in the $R - \Phi$ projection. The second term is due to multiple scattering.

To understand the impact parameter measurement, we study the following simple (CMS inspired) model, making use of two pixel layers:



We assume a particle originated at the origin, and the measured impact parameter d in the $r - \phi$ plane is due to the position uncertainty of $\delta_1 = \delta_2 \equiv \delta = 10 \mu\text{m}$ in both of the 2 CMS pixel layers, located at radii $r_1 = 4\text{ cm}$, $r_2 = 7\text{ cm}$ at low luminosity running²:

$$\delta d^{det} \equiv d = \frac{r_1}{r_2 - r_1} \delta_2 \oplus \frac{r_2}{r_2 - r_1} \delta_1 = 25 \mu\text{m} \quad (7)$$

²Later, at higher luminosity and radiation dose, there will be two layers, at 7 and 11 cm.

The smaller r_1 (for fixed $r_2 - r_1$), the better the resolution³. Taking into account also the silicon strips, the resolution improves to about $15 \mu\text{m}$. The multiple scattering contribution can be estimated by calculating the scattering angle in the beam pipe (CMS: beryllium) and the inner detector layer, assuming zero distance between beam pipe and first pixel layer:

$$\delta d^{MS} = r_1 \cdot \theta_{MS} = r_1 \cdot \frac{0.0136 \text{ GeV}}{p_T} \sqrt{\frac{L}{X_0}} \quad (8)$$

First we estimate which contribution is dominant:

a) Assuming a thickness of $L = 1 \text{ mm}$, and inserting $X_0(\text{Be}) = 35 \text{ cm}$ we get

$$\delta d^{MS,pipe} \sim \frac{30 \mu\text{m}}{p_T/\text{GeV}} \quad (9)$$

b) A single pixel layer is more than 2% of a radiation lengths thick, thus

$$\delta d^{MS,pixel} \sim \frac{80 \mu\text{m}}{p_T/\text{GeV}} \quad (10)$$

Thus, the latter effect is most important!

Combining all measurements (incl. silicon strips) the CMS impact parameter resolution is predicted (MC) to reach:

$$\delta d = 15 \mu\text{m} \oplus \frac{90 \mu\text{m}}{p_T/\text{GeV} \sqrt{\sin \theta}} \quad (11)$$

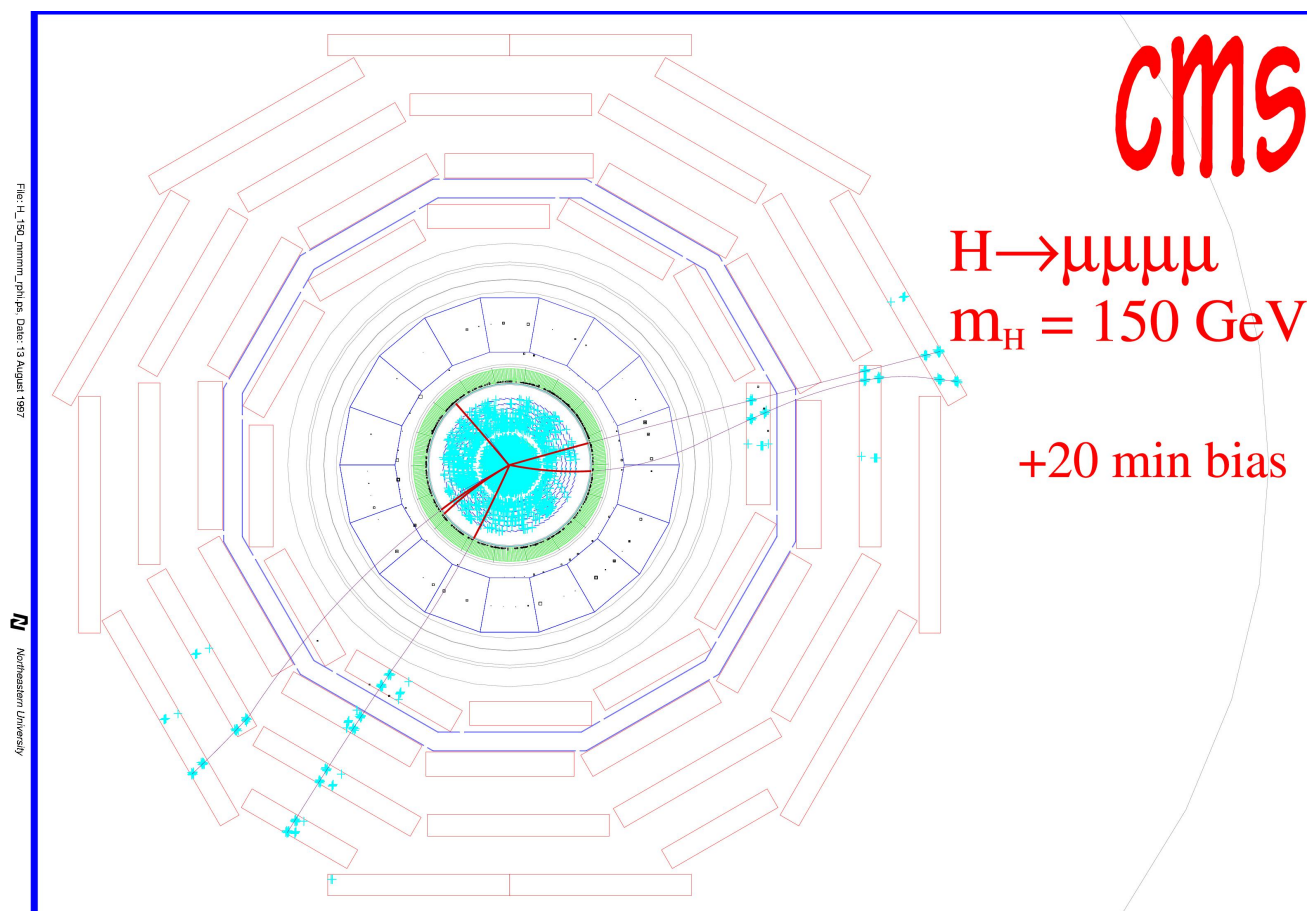
Thus our estimate on the multiple scattering term was good, but the silicon strip tracker must not be neglected.

³for fixed r_1 an increase of r_2 is beneficial!

1.2.5. Muons

A clean identification of muons is possible with track detectors, ‘muon chambers’, outside the hadron calorimeter + absorber material (assuming enough absorption lengths so that only few ‘punch through’ hadrons remain).

Example: Simulated ‘Higgs event’ in the CMS detector:

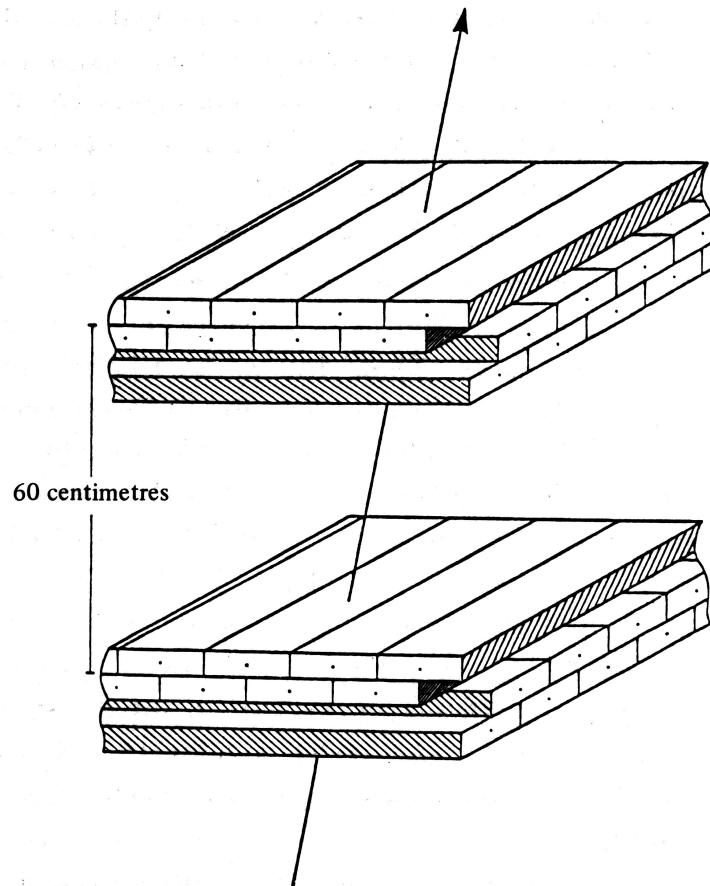


The momentum can be measured ‘stand alone’ with these muon detectors, and/or by ‘matching’ the muon track with the corresponding one seen in the inner tracker.

Also for triggering purposes these detectors are very important.

Due to the large surface to be covered, only relatively ‘cheap’ gas detectors can be used, silicon devices or scintillating fibres are not (yet) a realistic alternative.

UA1 used large area drift chambers¹, enclosing the magnet yoke in the barrel region and in the end-caps. In total 350 m^2 were covered (2 layers a 4 planes):

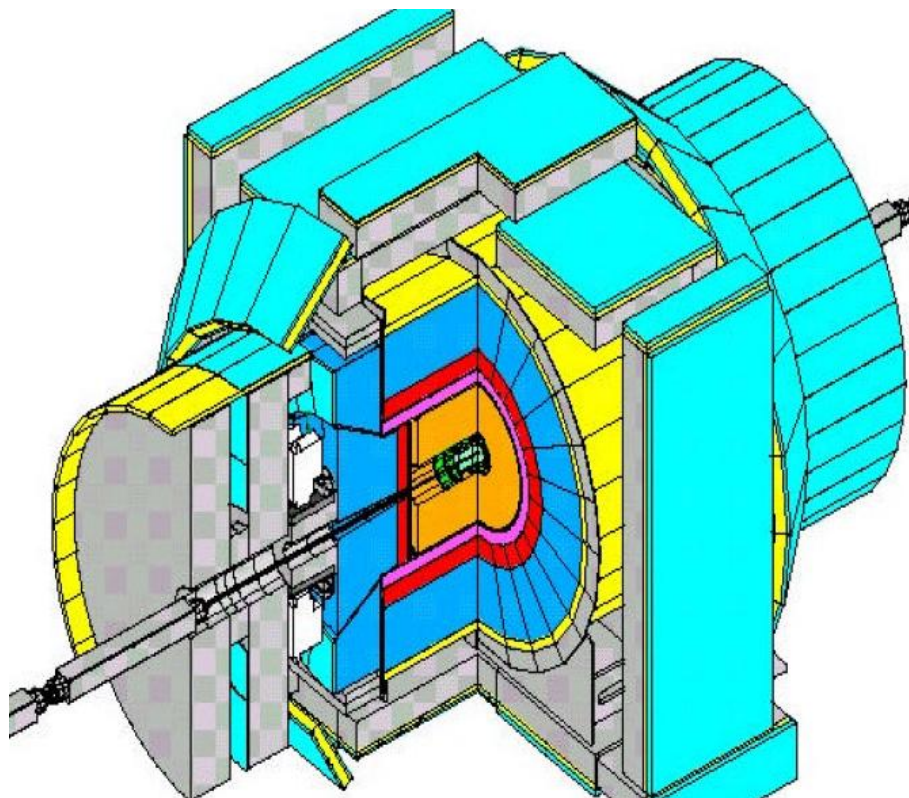


Obviously a stand-alone momentum measurement is not possible (no B-field), also a severe vertex constraint (R-z plane) is unavailable. The main purpose is the identification of muons via matching tracks seen in the other detector components; since the punch through fraction is substantial (one particle per 30 GeV hadronic shower at $\eta = 0$), this is an important task! The drift cells had a cross section of $15 \text{ cm} \times 5 \text{ cm}$ and gave a position resolution of $400 \mu\text{m}$. Later both UA1 magnet and muon chambers were reused in the NOMAD neutrino detector.

The **UA2** apparatus did not have outer muon detectors; thus the W (and Z) could only be studied in the $e\nu$ (e^+e^-) decay mode.

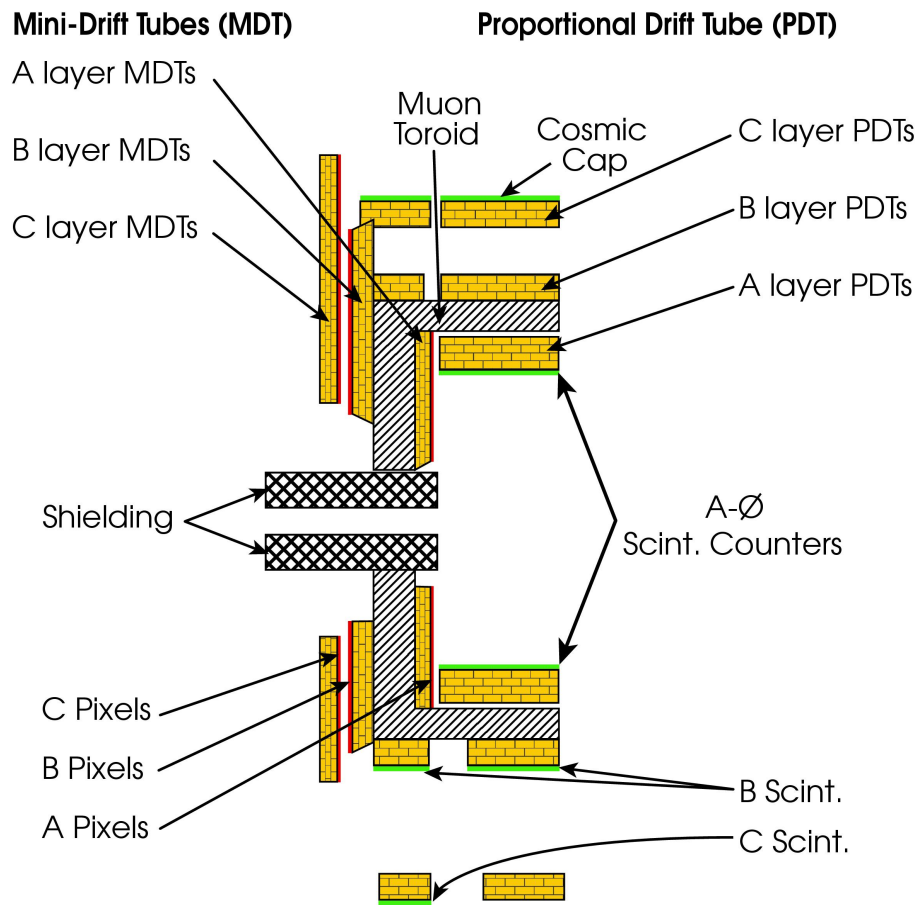
The **CDF** muon chambers cover the barrel, the intermediate region (45°) and surround the forward toroids. Apart from drift chambers (yellow) also scintillators (light blue) are employed:

¹built in Aachen

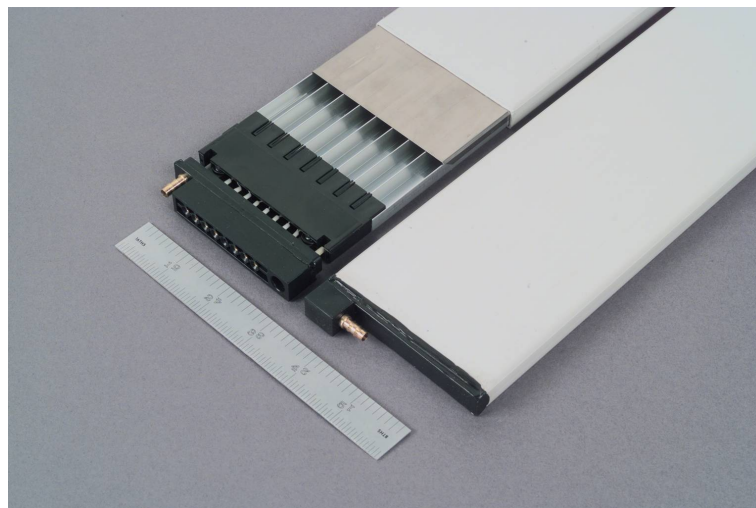


The very forward region is not covered. For small values of $|\eta|$ a nonmagnetic steel layer reduces the punch through in the outer of two separate chamber layers. The role of the muon chambers is similar to UA1, also the cell size is comparable, eg $15 \text{ cm} \times 2.5 \text{ cm}$ in the outer barrel region. The max. drift time is quite long, $1.4 \mu\text{s}$, but since the occupancy is low, this is acceptable. The scintillators are used to determine the corresponding beam crossing.

D0 uses two types of muon chambers (barrel and endcap regions) and scintillators (many in form of tiles):



The PDTs (Proportional Drift Tubes) cover the barrel, the MDT (Mini Drift tubes) have been added for run II in the forward regions:



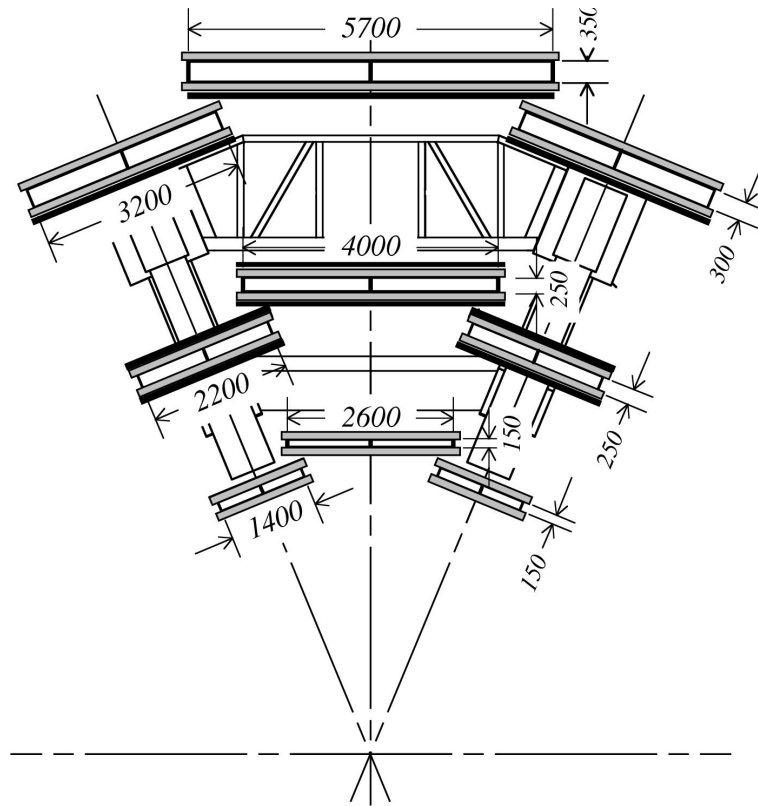
Due to the small size (~ 1 cm) the max. drift time is only 60 ns.

Since the inner layer of both the PDTs and MDTs is inside the toroid magnets, a stand alone momentum measurement is possible, but not very precise. At $\eta = 0$:

$$\frac{\Delta p}{p} = 0.3\% \cdot p/\text{GeV} \oplus 18\% \quad (1)$$

The most ambitious muon detector (together with the air toroid) is being built by the **ATLAS** collaboration. They use MDTs (Monitored Drift Tubes), RPCs (Resistive Plate Chambers) and other species, which we will not discuss here.

In the barrel region the arrangement looks like this:



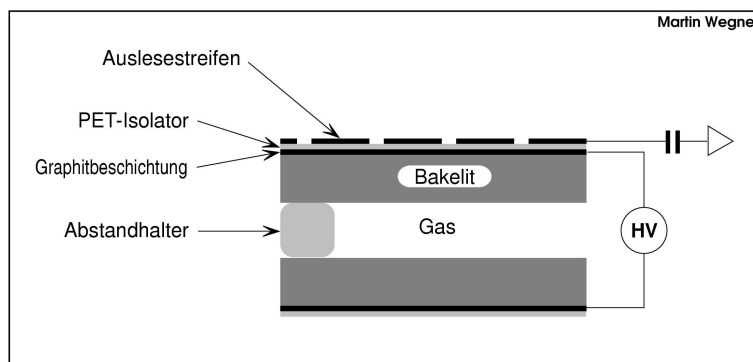
(light grey: MDT, black: RPC).

The MDT tubes have a diameter of **3 cm** and should reach a single cell resolution of $< 100 \mu\text{m}$. They are operated at a pressure of **3 bar** (Ar CO_2) and a voltage of **3.1 kV**. The good resolution is due to the short drift distance, the cell symmetry and the pressure (less charge diffusion, higher ionisation). One completed chamber:



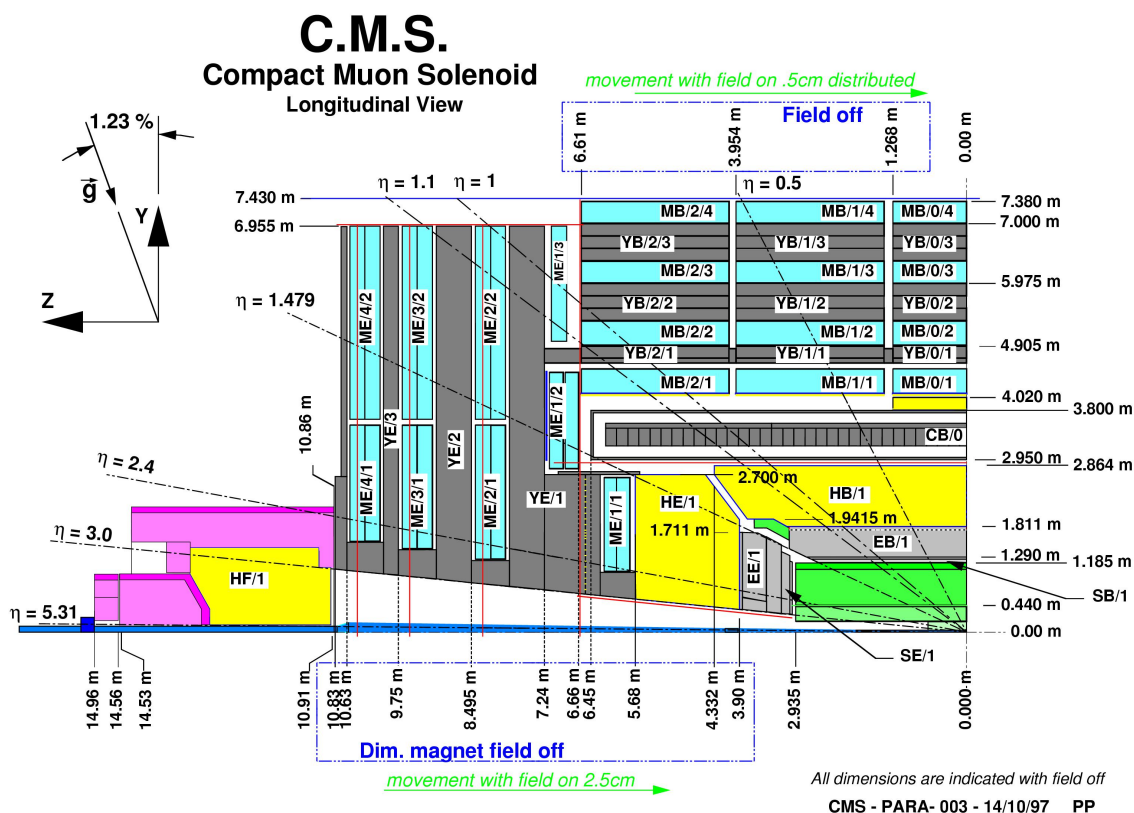
In total more than 300000 tubes will be produced, covering a surface of more than 5000 m². To be able to exploit the excellent resolution, a very precise chamber alignment is crucial.

RPCs are made out of two parallel plates with a small gas gap in between (few mm) and are operated at several kV:

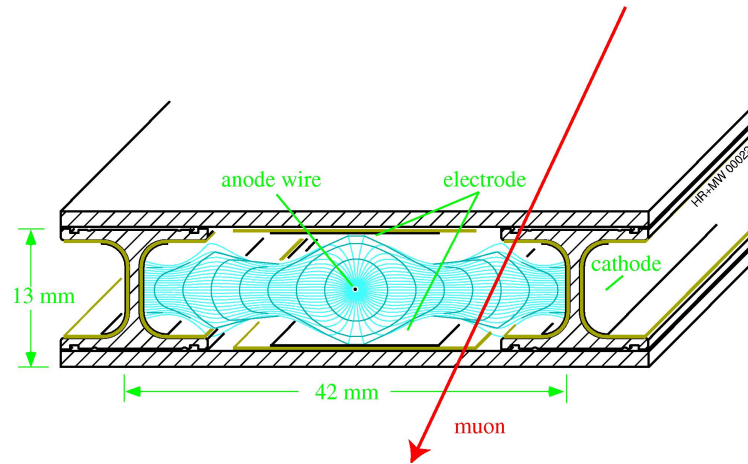


A charged particle initiates an avalanche, which induces charges on the readout strips. Important: the bakelite plates have a very high resistivity, so that locally the field collapses at this moment, thus the avalanche is interrupted and does not spread out. They are relatively simple to fabricate, since they don't use wires. Their high speed (some ns pulse length) make them ideal detectors for triggering purposes.

Also the CMS muon spectrometer uses RPCs, but the precision devices are again wire chambers, DTs (Drift Tubes) in the barrel region and CSCs (Cathode Strip Chambers) in the endcap region (high track density, high rate):

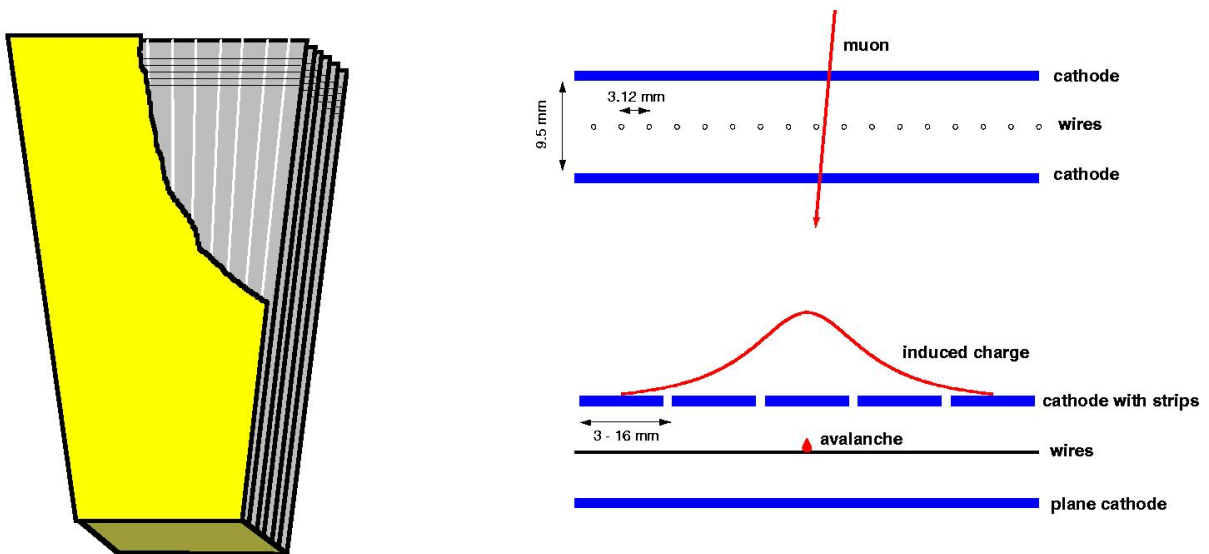


The barrel chambers consist of 190000 rectangular drift cells of typical size $4 \text{ mm} \times 1.5 \text{ mm} \times 2.5 \text{ m}$:



They are operated at standard pressure (Ar CO₂) and reach a single wire resolution of $200 \mu\text{m}$.

The working principle of CSCs is illustrated here:



Both cathodes and anodes (no drifttime measurement) are read out.

They have several advantages compared to DTs,

- both coordinates measured
- relatively insensitive to magnetic field
- small cell size \rightarrow high rate capability

but they are more expensive.

Comparison of muon detectors:

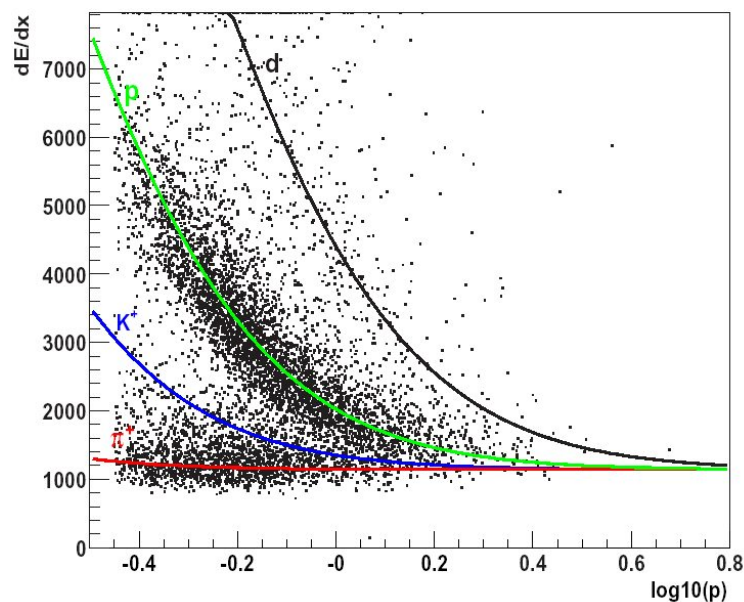
detector	type	pos. resol. / μm	channels
UA1	drift	400	7000
CDF	drift	200-300	7000
D0	drift	500 -700	23000
ATLAS	drift	100	400000
CMS	drift	200	700000

1.2.6. Particle identification

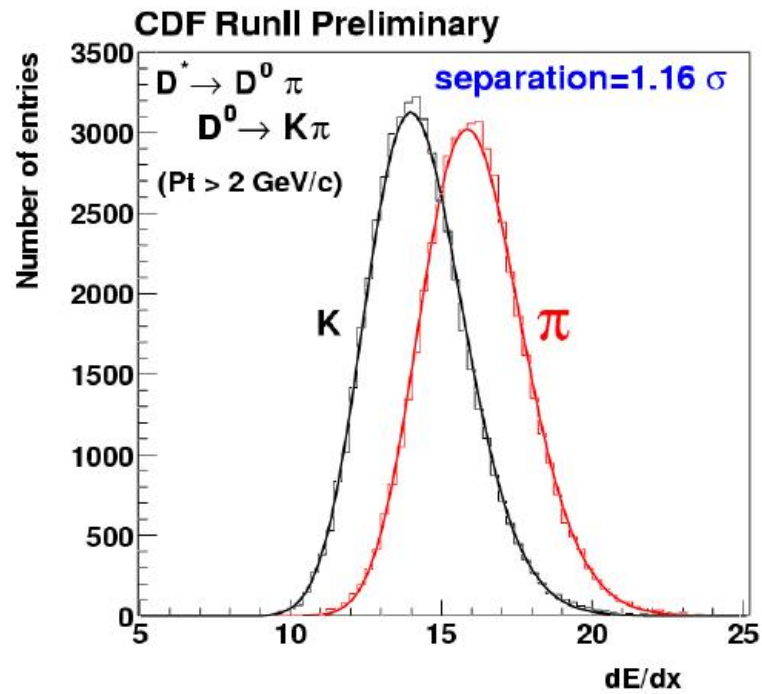
We have already encountered several examples of particle identification in the previous sections, making use of transition and Cerenkov radiation and - for muons - range!

A few more comments on dE/dx measurements in the central tracker, allowing to distinguish between charged hadrons of different type (π , K , p):

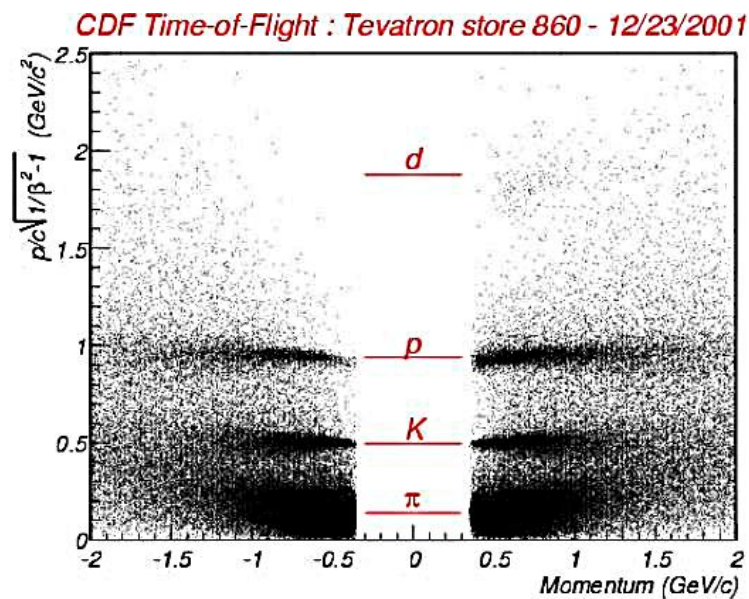
- The LHC silicon strip detectors are not foreseen for a dE/dx measurement (work only at low momenta - curl up; too few measurements; ATLAS: pulse height not read out!)
- CDF has demonstrated that in principle a silicon detector can be used:



- High quality dE/dx measurements are possible in the wire chambers of UA1 and CDF, both sampling with $\geq \sim 100$ cells:



Another tool in particle identification is TOF (Time of Flight), as used for example in CDF; their scintillators + PMs, installed behind the COT, reach a resolution of 100 ps:



The quantity plotted on the vertical axis is (apart from factors c^n):

$$p \sqrt{1/\beta^2 - 1} = m \gamma \beta \sqrt{1/\beta^2 - 1} = m \quad (2)$$

where p is measured in the tracker and β in the TOF system.

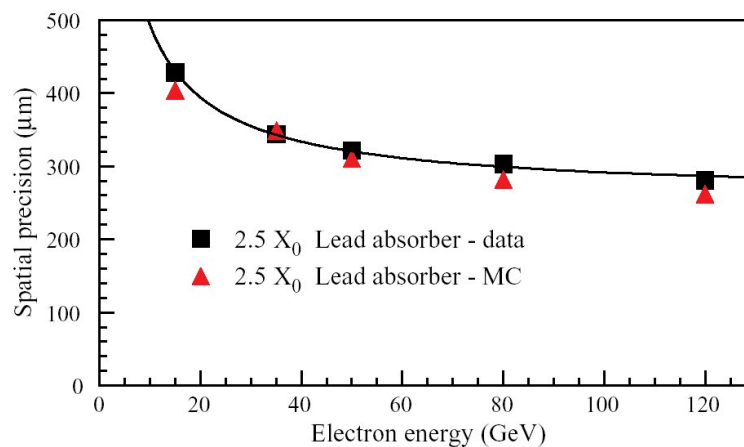
Finally the preshower detectors should be mentioned, which are used by CDF, D0, ATLAS and CMS.

These are thin position measuring detectors with absorber material ($\sim 1 - 3 X_0$), located in front of the electromagnetic calorimeters. Thus they measure the transverse profile in the first shower part. Their purpose is twofold:

- Distinction between an electron, a single photon and a $\pi^0 \rightarrow \gamma\gamma$
- Precise measurement of shower starting point (\rightarrow photon direction, electron track matching)

They can be realised in different ways: wire chambers, scintillators (CDF), silicon strips (CMS), scintillating fibres (D0), or a high granularity compartment of a LAr calorimeter (ATLAS).

This graph shows the simulated and measured (test beam) position resolution for the CMS preshower apparatus:



The transverse shower (maximum) position resolution by the crystals is somewhat less good (factor 1.7). Combining both measurements gives the shower direction without assumption on the event vertex.

In the following some selected physics topics will be presented.

2.1. Bottom physics

References:

- CERN yellow report CERN 2000-004, G. Altarelli and M.L. Mangano (editors), 'Proceedings of the workshop on standard model physics (and more) at the LHC'
- M. Paulini, 'B Lifetimes, Mixing and CP Violation at CDF', Int. J. Mod. Phys. A14, 2791 (1999)

Bottom Physics (= b physics) at p p colliders can serve two purposes:

- a) exploration of the properties of b quarks and b hadrons
- b) using b final states to identify particles as top quarks or higgs bosons.

We concentrate here on the first aspect.

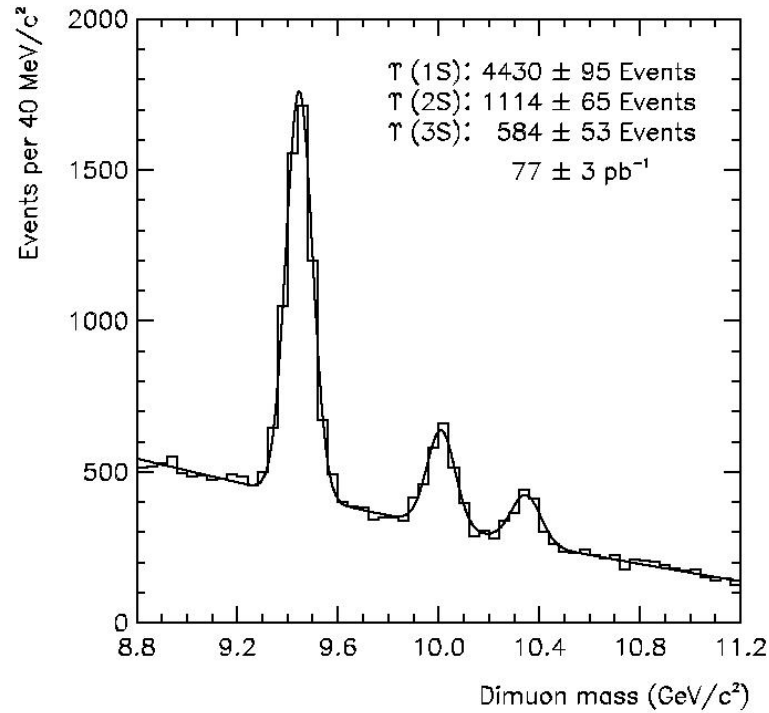
2.1.1 b hadrons and b jets

Sometimes it is possible to identify the b hadron explicitly (full reconstruction), in other cases 'only' the jet containing the b can be identified (e.g. via a secondary vertex); of course the two methods don't exclude each other.

2.1.1.1 b hadrons

- The Upsilon particles Υ contain a $b\bar{b}$ pair with parallel spins. Since they are short lived (elm. and strong decays, $\Gamma > 25 \text{ keV}$, $c\tau < 10^{-11} \text{ m}$), a secondary vertex is not measurable; these states can be identified via their leptonic decays ($\text{Br}(\Upsilon(1s) \rightarrow l^+l^-) = 2.5\%$). Similar arguments hold for the χ_b states (spins antiparallel).

Υ production has been seen in CDF and D0. The CDF $\mu^+\mu^-$ invariant mass peaks at 1.8 TeV are shown here:

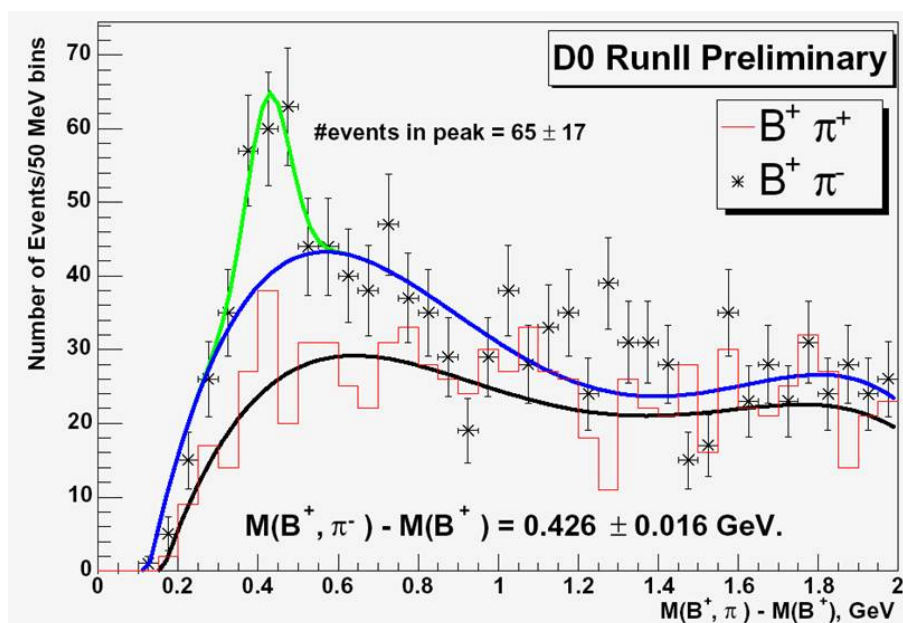


- Hadrons with ‘open’ bottom quantum numbers are either mesons or baryons. The mesons can contain - apart from the b - a light quark (u,d), or a quark from the second family (s,c), which is indicated by a subscript, e.g. B_s^0 . b hadrons are produced in their ground state or in excited states, labelled B^* or B^{**} . In their ground state they decay weakly and ‘profit’ from the smallness of the CKM matrix elements V_{ub} , V_{cb} , such that their lifetime is rather long ($\sim 1\text{ps}$), translating into decay lengths of a few mm. The following table¹ summarizes the properties of some b hadrons.

state	J^P	mass/GeV	τ/ps	quarks	decay (BR) [example!]
B^+	0^-	5.2790 ± 0.0005	1.674 ± 0.018	$u\bar{b}$	$\bar{D}^0 l^+ \nu(10\%)$
$B^0 \equiv B_d^0$	0^-	5.2794 ± 0.0005	1.542 ± 0.016	$d\bar{b}$	$D^- l^+ \nu(2\%)$
B_s^0	0^-	5.369 ± 0.0024	1.461 ± 0.057	$s\bar{b}$	$D_s^- l^+ \nu(8\%)$
B_c	0^-	6.4 ± 0.4	0.47 ± 0.17	$c\bar{b}$	$J/\Psi l^+ \nu X(\ll 1\%)$
Λ_b	$\frac{1}{2}^+$	5.624 ± 0.009	1.29 ± 0.080	udb	$\Lambda_c l^- \bar{\nu}(8\%)$

A B^{**} analysis result from D0 is shown here:

¹Note: For the neutral B mesons mixing has to be taken into account, see below.



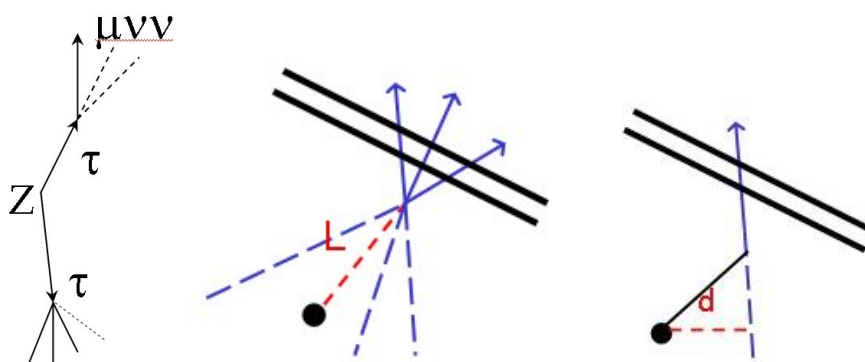
The neutral B_d^{**} decays strongly into $B^+ \pi^-$. Its mass is measured (see plot) to $5.710 \pm 0.016 \text{ GeV}$. The B^+ can be reconstructed e.g. via its decay $J/\Psi K^+$. Instead of plotting the invariant mass constructed from all decay products of the B_d^{**} , a more precise mass determination can be obtained from the difference $m(B_d^{**}) - m(B^+)$, since here the measurement errors drop out to a large extent! B^* mesons are spin-1 particles with zero orbital momentum and the two (anti)quark spins aligned. B^{**} denotes spin-1 mesons with orbital momentum 1 (p-wave) - however spin and quantum numbers have not yet been measured for the B_d^{**} , which was observed also at LEP and by CDF.

2.1.1.2 b jets

A b-jet can be identified by (a combination of) the following signatures, in decreasing importance:

- lifetime / decay length / impact parameter
- lepton (from $B \rightarrow l X$)
- jet topology (slightly fatter than for light quarks)

We will briefly discuss the lifetime tag. There are two possibilities:



- decay length method

If several tracks of the final state can be reconstructed, the decay path

$$L = t\gamma\beta \approx t \frac{E}{m} \quad (1)$$

can be measured. E is the energy of the decaying particle, m its mass and t its lifetime. We assume $\beta \rightarrow 1$.

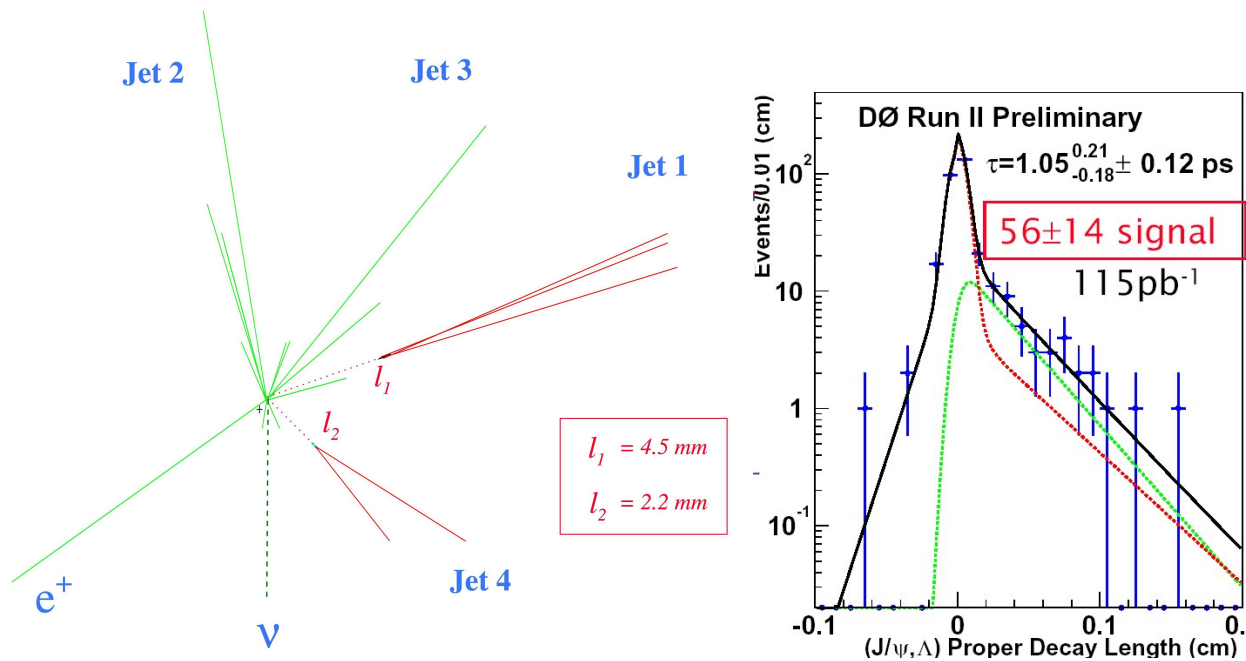
- impact parameter (= distance of closest approach) method

A single track that does not pass through the primary vertex indicates the decay of a long lived particle. For a relativistic particle the distance of closest approach is given by

$$d \sim L \cdot \frac{p_s^*}{p} \sim L \cdot \text{const} \frac{m}{p} = \text{const} \cdot t \quad (2)$$

p_s^* is the momentum of the daughter particle in the rest frame of the mother particle. Note that d is independent of the energy E of the decaying particle!

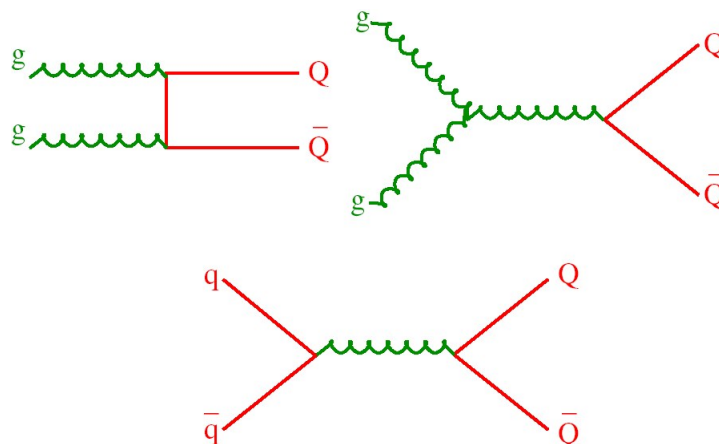
Examples:



The CDF event (figure, left) shows a top candidate from run I. The Λ_b (figure, right) was reconstructed via $\Lambda_b \rightarrow J/\Psi \Lambda \rightarrow \mu^+ \mu^- p \pi$.

2.1.2 bottom production

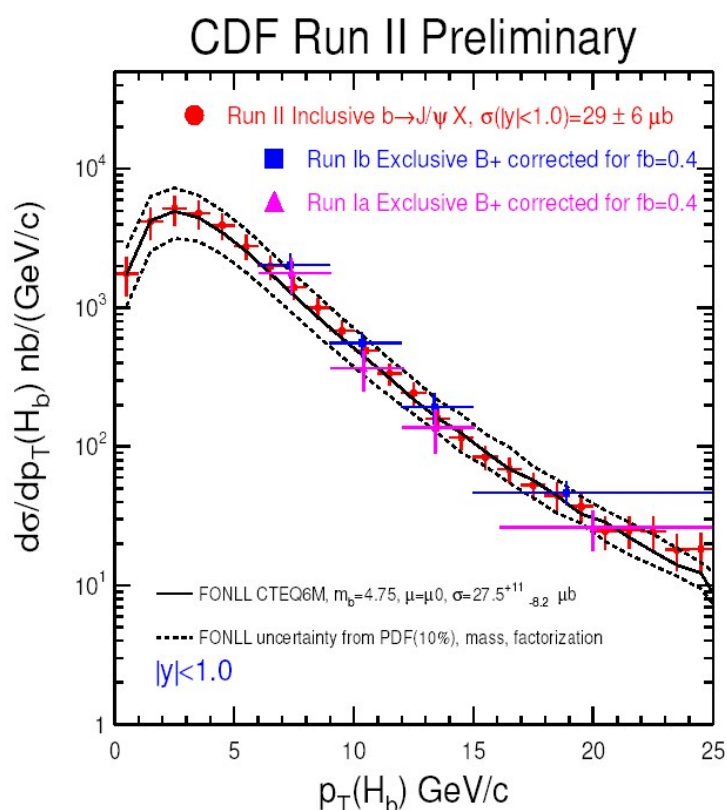
In most cases a $b\bar{b}$ is produced, in particular via strong processes like



Two b quarks can also arise from $t\bar{t}$ or Z decays. Single b quark production (e.g. via $W^* \rightarrow t\bar{b}$) is rare.

In the following we consider only direct pair production. Note that in pp collisions the final state will always contain additional hadrons (beyond the two B particles), so that the two B hadrons are **NOT** ‘entangled’².

The cross section for inclusive b production is large, $\sim 10\mu\text{b}$ at the SPS, $\sim 50\mu\text{b}$ at the Tevatron and even larger at the LHC. These numbers should be compared to the exclusive $\Upsilon(4s)$ cross section in e^+e^- machines (1 nb) and the b xsection on the Z resonance (7 nb).

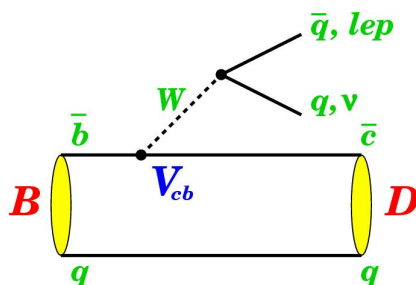


²This is different for $e^+e^- \rightarrow \Upsilon(4s) \rightarrow BB$

There is good agreement between QCD predictions³ and CDF measurements⁴.

2.1.3 B decays

Many lifetimes and branching fractions have already been measured and fill the tables of the Particle Data Book. Most decay modes can be described by a simple ‘spectator’ diagram as shown here:

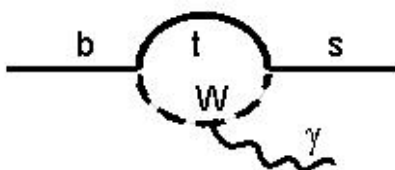


More interesting are ‘rare decays’, which are sensitive to ‘small’ CKM matrix elements and/or ‘new physics’.

We present two examples:

2.1.3.1 $b \rightarrow s \gamma$

A direct $b \rightarrow s$ transition via Z exchange is not possible (unitarity of CKM quark mixing matrix). Such a Flavor Changing Neutral Current (FCNC) can be accomplished through higher order ‘penguin diagrams’ such as



Note that the γ (or a gluon) is needed for 4-momentum conservation. This process is interesting since it allows the determination of the small matrix element $|V_{ts}|$ and/or to set limits on new particles like charged higgs bosons, which would also contribute (same diagram with $W^+ \rightarrow H^+$).

The $BR(B \rightarrow K^* \gamma)$ has been measured⁵ already in 1993 to $\sim 5 \cdot 10^{-5}$ by the CLEO collaboration at the $\Upsilon(4s)$ resonance. At the Tevatron so far only upper limits could be set, the most recent one is $< 1.4 \cdot 10^{-4}$ (95%) from the CDF experiment. The goal at LHC will be to reach a high statistical accuracy so that a precise determination of the corresponding branching fraction can be achieved.

In principle the same argument can be made for a V_{td} measurement through $b \rightarrow d \gamma$ ($B \rightarrow \rho \gamma$), however theoretical uncertainties (QCD corrections) are large, so that the interpretation is difficult. Also, the branching fraction is smaller by $|V_{td}/V_{ts}|^2 = \mathcal{O}(0.01)$.

³FONLL = Fixed Order next-to-leading order terms + Next-to-Leading-Log large- p_T resummation

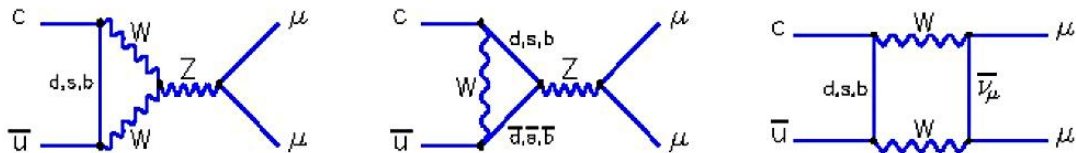
⁴this was not always the case - part of the differences could be traced down to the wrong use of a fragmentation model

⁵note that the s in the final state combines with the ‘spectator quark’ d to form a K meson - which is in an excited state since the photon radiation has reversed the quark spin ($b \rightarrow s$).

2.1.3.2 $B_s \rightarrow \mu^+ \mu^-$

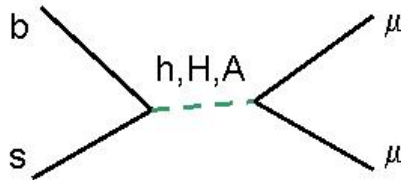
Neutral mesons (apart from the π^0) can - to first order - not decay into a lepton-antilepton pair, since this would require a FCNC.

Higher order diagrams make these decays possible, however with small branching fractions. Example $D^0 \rightarrow \mu^+ \mu^-$:



The SM prediction for the branching fraction $B_s \rightarrow \mu^+ \mu^-$ is very small ($\sim 3 \cdot 10^{-9}$), and cannot be measured at the Tevatron, however it might be possible at the LHC. The dominant contribution is given by the heaviest virtual quark exchange (top). Since $BR(B_s \rightarrow \mu^+ \mu^-)$ is proportional to $|V_{ts}|^2$ it is expected to be a factor of ~ 30 bigger than the corresponding BR for B_d decays.

However, in SUSY models this branching fraction can be enhanced by up to 3 orders of magnitude, through higgs mediated FCNC diagrams like this one:



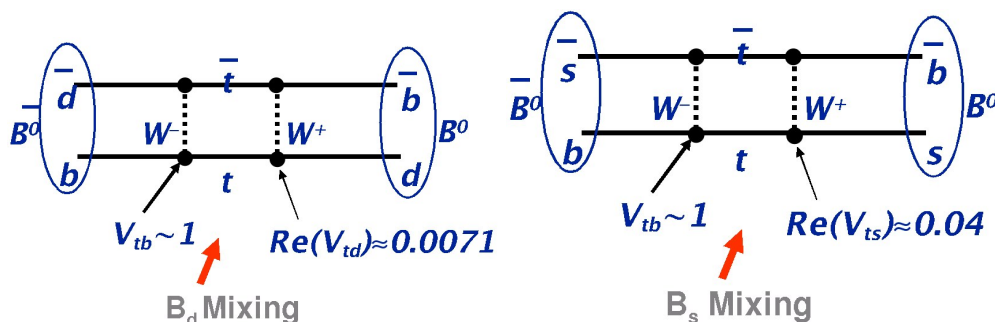
The BR grows with $\tan^6 \beta$ (ratio of vacuum expectation values of higgs doublets)!

CDF has searched (in vain) for the this decay in the run II data and set the following upper limit:

$$BR(B_s \rightarrow \mu^+ \mu^-) < 1.2 \cdot 10^{-6} \quad (95\% \text{ CL}) \quad (3)$$

2.1.4 B mixing

The neutral B mesons (both B^0 and B_s^0) can ‘mix’ and ‘oscillate’,



a phenomenon well known from the Kaon system and in principle also expected for neutral D mesons. It is a weak process changing s , c or b quantum numbers by ± 2 .

Since this topic is one of the ‘hot’ ones at the Tevatron, we will discuss it in some detail here.

In the next sections we will assume that CP violation does not exist!

2.1.4.1 Phenomenology

Let’s review first the neutral K sector with $K^0 = d\bar{s}$ and $\bar{K}^0 = s\bar{d}$. Oscillations in the kaon system have been predicted by Gell-Mann and Pais in 1955; they were verified by several experiments (Brookhaven) in the following years.

The new neutral K mesons are neither C nor CP eigenstates⁶:

$$CP(K^0) = \bar{K}^0 \quad CP(\bar{K}^0) = K^0 \quad (4)$$

However, the neutral kaons are observed to decay (weakly) into CP eigenstates like $\pi\pi$ (+1) or $\pi\pi\pi$ (-1). So, at this moment the mother particle must be in a CP eigenstate. We can construct CP eigenstates as linear combinations:

$$K_1 \equiv K_s = \frac{1}{\sqrt{2}} \cdot (K^0 + \bar{K}^0) \quad K_2 \equiv K_l = \frac{1}{\sqrt{2}} \cdot (K^0 - \bar{K}^0) \quad (5)$$

or

$$K^0 = \frac{1}{\sqrt{2}} (K_s + K_l) \quad \bar{K}^0 = \frac{1}{\sqrt{2}} (K_s - K_l) \quad (6)$$

Obviously:

$$CP(K_s) = +K_s \quad CP(K_l) = -K_l \quad (7)$$

These two states have different masses and lifetimes/decay widths, which can be written in form of the dimensionless quantities

$$y = \frac{\Gamma_s - \Gamma_l}{2\Gamma} \quad x = \frac{m_s - m_l}{\Gamma} \quad (8)$$

where $\Gamma = 0.5(\Gamma_s + \Gamma_l)$. The reason for relating $\Delta m = m_s - m_l$ to Γ in the definition of x will become clear soon (both Δm and Γ determine the time dependence). Note that while $|y| < 1$ no such constraint exists for x !

We can now apply the laws of quantum mechanics to calculate the time evolution of the kaon states. In their rest system the CP eigenstates have this time dependence:

$$K_i(t) = K_i(0) \cdot e^{-im_i t - \Gamma_i/2 \cdot t} \quad \Gamma_i = 1/\tau_i \quad (9)$$

The mass = energy term (imaginary) describes the quantum mechanical oscillation of the phase, the part containing Γ (real) stands for the decay. The amplitude A for finding at proper time t a \bar{K}^0 state in a beam containing only K^0 at $t = 0$ is given by

$$A_{\bar{K}^0}(t) \equiv \bar{K}^0(t) = \frac{1}{\sqrt{2}} (K_s(t) - K_l(t)) \quad (10)$$

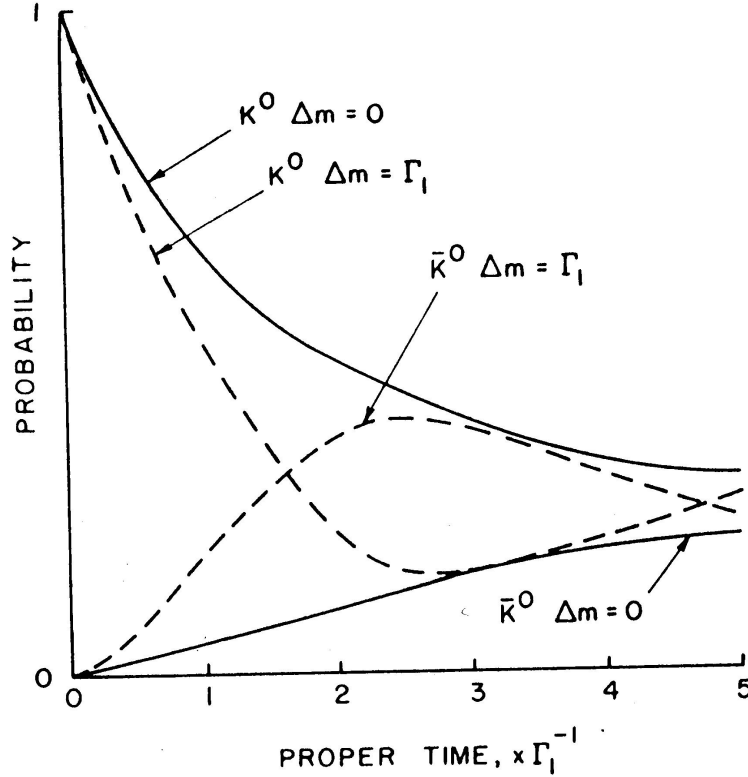
$$= \frac{1}{2} K^0 \cdot (e^{-im_s t - \Gamma_s t/2} - e^{-im_l t - \Gamma_l t/2}) \quad (11)$$

⁶sign is convention dependent

The corresponding probability $P = AA^*$ for finding a \overline{K}^0 at proper time t is thus

$$P_{\overline{K}^0}(t) = \frac{1}{4} \cdot (e^{-\Gamma_s t} + e^{-\Gamma_l t} - 2e^{-\Gamma t} \cdot \cos(\Delta m t)) \quad (12)$$

A similar formula describes the K^0 probability. Note that the sign of Δm cannot be measured this way⁷. The figure shows schematically the time evolution.



Experimentally, the states K^0 and \overline{K}^0 can be distinguished through their strong interactions or semi-leptonic decays. Result of those measurements (average over many experiments):

$$\tau(K_s) = 8.9 \cdot 10^{-11} \text{ s} \quad \tau(K_l) = 5.2 \cdot 10^{-8} \text{ s} \quad (13)$$

$$m = 0.5 (m_s + m_l) = 498 \text{ MeV} \quad \Delta m = 3.5 \cdot 10^{-6} \text{ eV} = 5.3 \cdot 10^9 / \text{s} \quad (14)$$

or

$$x = 0.95 \quad y = 0.997 \quad (15)$$

Thus the mass difference is much smaller than the average mass, while the lifetime difference is huge! Therefore the CP eigenstates can be distinguished best through their lifetimes (and not their masses!), the indices l and s mean 'long' and 'short'. $x = \mathcal{O}(1)$ implies that the oscillation period and the decay time constant are of the same order of magnitude.

Now we turn to the neutral B sector, or, more precisely, the two sectors B_d and B_s . B_d^0 oscillations have been discovered 1986 by UA1 and the Argus $e^+e^- \rightarrow \Upsilon(4s)$ experiment at DESY. The B_s

⁷In K system: from regeneration experiments, in B system: so far only from theory.

oscillations, which occur ‘faster’ and are more difficult to measure, have not been observed yet. The CP eigenstates are named $B_1 = B_L, B_2 = B_H$.

In principle the phenomenology is the same as for the kaon sector - just the numbers are quite different! B_d^0 sector:

$$\tau_d = 1.54 \cdot 10^{-12} \text{ s} \quad (16)$$

$$m_d = 5280 \text{ MeV} \quad \Delta m_d = 3.2 \cdot 10^{-4} \text{ eV} = 4.9 \cdot 10^{11} / \text{s} \quad (17)$$

or

$$x_d = 0.76 \quad (18)$$

So far the lifetime difference could not be measured, experimental upper limits ($y < 0.4$) are crude. Theoretical expectations are of the order of $y \sim 0.01$. The mass difference is still small compared to the absolute mass, but the oscillation curve (12) is now dominated by the Δm term since $y \rightarrow 0$. Therefore, we distinguish the B^0 CP eigenstates by their mass and call them ‘Heavy’ (H) and ‘Light’ (L).

For the B_s^0 system only lower limits on Δm_s and $x \equiv x_s$ exist:

$$\tau_s = 1.46 \cdot 10^{-12} \text{ s} \quad (19)$$

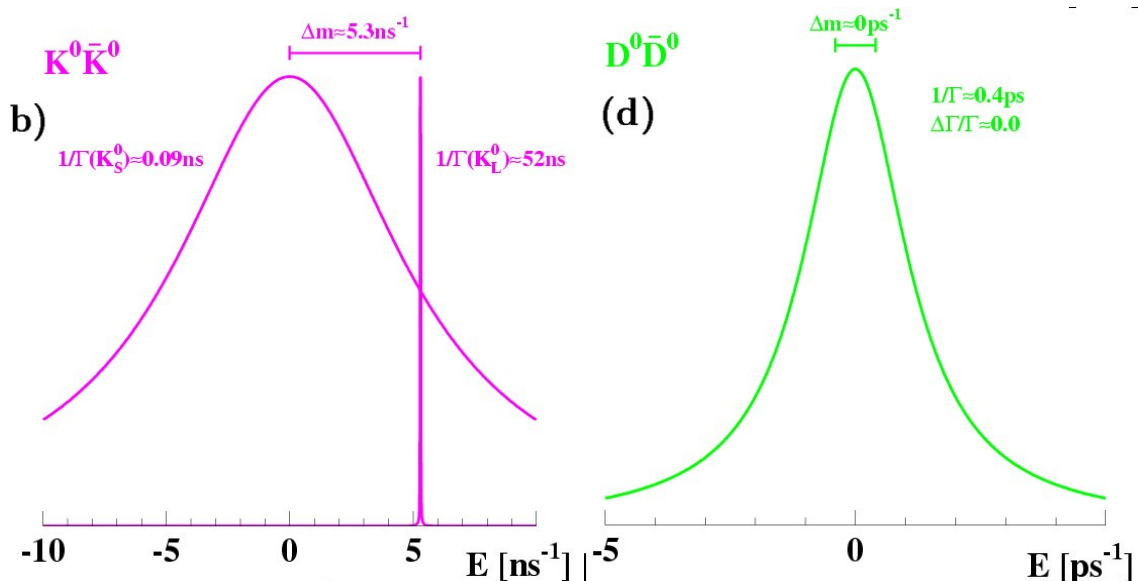
$$m_s = 5370 \text{ MeV} \quad \Delta m_s > 8.6 \cdot 10^{-3} \text{ eV} = 1.3 \cdot 10^{13} / \text{s} \quad (20)$$

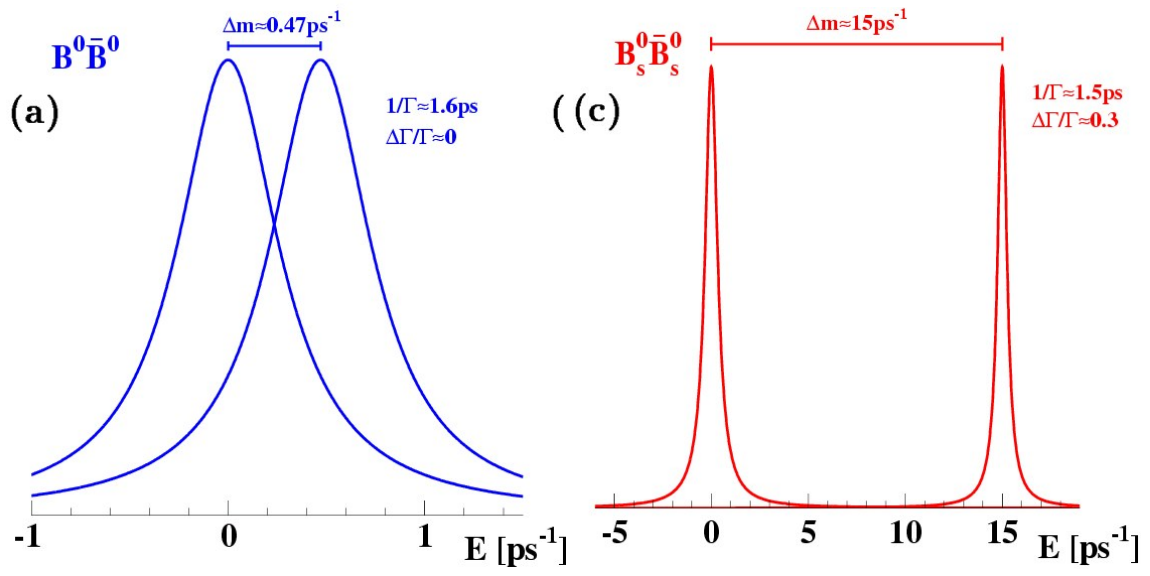
or

$$x_s > 19 \quad (95\%CL) \quad (21)$$

Again, the lifetime difference is unknown. Theory predicts $y \sim 0.1$. New: Here the oscillation period is much shorter than the decay time, thus it will be possible to observe several oscillations before the B_s decays!

A nice graphical comparison (from Paulini) of the different neutral meson systems is shown here:





2.1.4.2 CKM matrix and meson oscillations

The neutral K and B mesons are certainly interesting quantum mechanical systems; their particular importance for high energy physics lies in the connection to CKM matrix elements.

Let's first discuss the lifetime difference alias y . The large value in the kaon system can be understood easily: The decay

$$K_s \rightarrow \pi^0 \pi^0 \text{ oder } \pi^+ \pi^- \quad (\text{CP - eigenvalue} = +1) : \quad (1)$$

is favored by phase space with respect to

$$K_l \rightarrow \pi^0 \pi^0 \pi^0 \text{ oder } \pi^+ \pi^- \pi^0 \quad (\text{CP - eigenvalue} = -1) : \quad (2)$$

In B decays the difference between the partial decay widths of the many decay modes are much smaller. They depend on the dominant CKM matrix elements, the particle masses involved and QCD corrections.

The more interesting quantity is x alias Δm .

As can be seen from the B mixing box diagrams (chapter 2.1.4), the mixing probability depends on V_{td} or V_{ts} , since the virtual top exchange dominates (proof not given here). It can be shown that the mass difference is proportional to the mixing strength:

$$\Delta m_q \sim |V_{tq}|^2 \quad (3)$$

The factor $|V_{tb}|^2 \approx 1$ is not displayed. The remaining factors (also not shown) contain QCD effects and the top mass, leading to theoretical uncertainties of $\sim 20\%$. The uncertainties drop out to a large extent when considering the ratio m_s/m_d . We understand now why x_s is expected to be two orders of magnitude larger than x_d !

2.1.4.3 Oscillation measurements at pp colliders

To measure B oscillations, B^0 and \overline{B}^0 must be distinguished, that is their flavor must be tagged at the time of production and decay. There are different possibilities, we will discuss here only the lepton tag

$$B^0 \rightarrow l^+ X \quad \overline{B}^0 \rightarrow l^- X \quad (4)$$

i.e. the sign of the lepton charge is equal to the sign of the bottom quark charge. Note that this works also for charged b mesons and for b baryons.

For an oscillation measurement the following steps must be made:

- identification of B hadron/jet: secondary vertex!

- determination of flavor at decay (t).
- determination of flavor at production ($t = 0$).
Since in most cases the b (\bar{b}) is produced together with a \bar{b} (b), we need to tag the ‘other’ b hadron, which can be done the same way - via its leptonic decay¹.
- measurement of proper decay time. This can be determined from the decay length L and the B momentum p .
The momentum measurement is easy only if the B hadron is completely reconstructed; if some decay products are not seen (neutral ones), an appropriate correction factor must be applied.

Therefore one looks for $b\bar{b}$ events (secondary vertices!) with two associated leptons², determines the charges, classifies the events as ‘same-sign’ or ‘opposite sign’, and plots the asymmetry

$$A_{mix}(t) = \frac{N_{os}(t) - N_{ss}(t)}{N_{os}(t) + N_{ss}(t)} \quad (5)$$

as a function of proper decay time t . In the ideal case (no background, misidentification, resolution effects. . .) the two classes represent the mixed and unmixed events. In the limit of negligible lifetime differences $y \rightarrow 0$ the integrated oscillation probability becomes simply

$$P_{B^0}(t) = \frac{1}{2} e^{-\Gamma t} \cdot (1 - \cos(\Delta m t)) \quad (6)$$

This probability is proportional to N_{ss} , the number of same sign dilepton events as a function of decay time:

$$N_{ss}(t) \sim e^{-\Gamma t} \cdot (1 - \cos(\Delta m t)) \quad (7)$$

Similarly:

$$N_{os}(t) \sim e^{-\Gamma t} \cdot (1 + \cos(\Delta m t)) \quad (8)$$

If we start with a \bar{B}^0 instead of a B^0 , the signs of the leptons change, but the formulae for N_{ss} and N_{os} are still valid. Thus:

$$A_{mix}(t) = \cos(\Delta m t) \quad (9)$$

In this asymmetry the exponential decay term drops out - however it nevertheless determines the event statistics when performing the measurement!

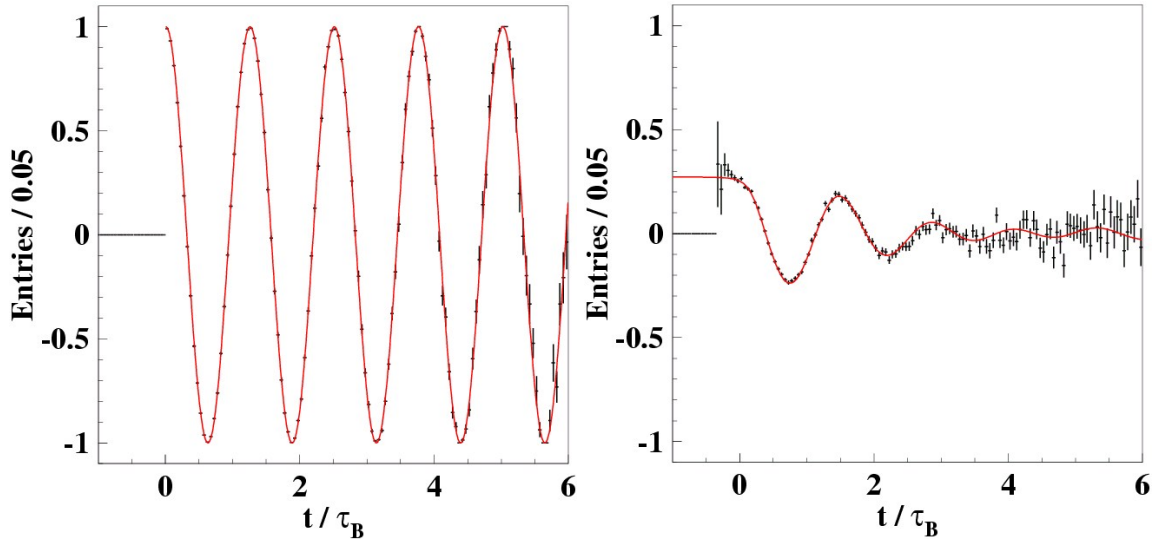
The first hint for B oscillations was found by the UA1 collaboration in 1986, which saw an excess of same-sign dilepton events, but without measuring the time dependence.³

Thus the measured asymmetry should look like the left graph below:

¹However, we must take into account, that the second meson can also be a neutral one, so it may oscillate, too. This requires a small correction to the simple formulae we will derive here.

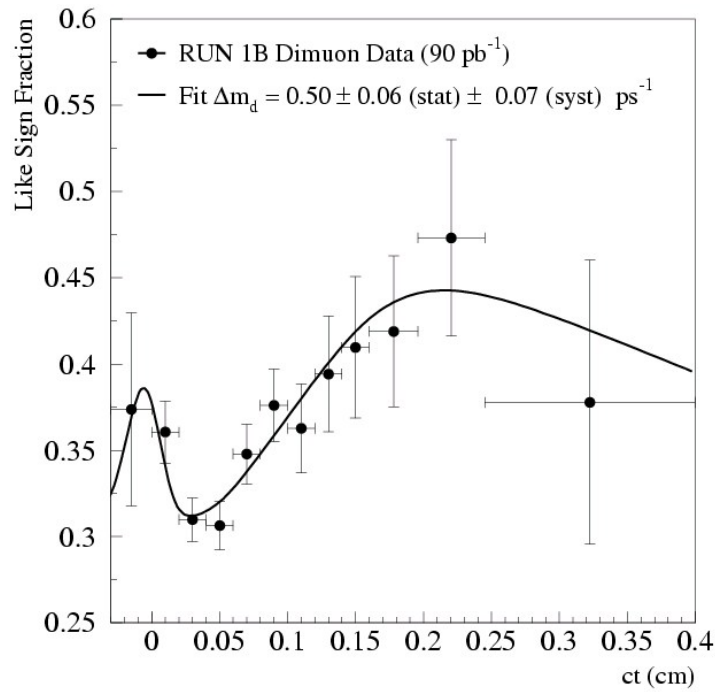
²Since the leptonic branching fractions are of the order of 10%, this is a small fraction of all b events!

³if the time dependence is not measured, often the term ‘mixing’ is used, else the word ‘oscillation’ is employed.



In real life several effects deteriorate this cosine curve, in particular the momentum resolution (smears out t , in particular at large values) and the mistag probability (wrong charge, wrong lepton, background. . .) play a negative role. The resulting Monte Carlo prediction (for CDF, run I) is shown on the right.

CDF has published a measurement based on dimuon events in 1999. The sample contains 2044 like-sign and 3924 opposite-sign muon events. The result:



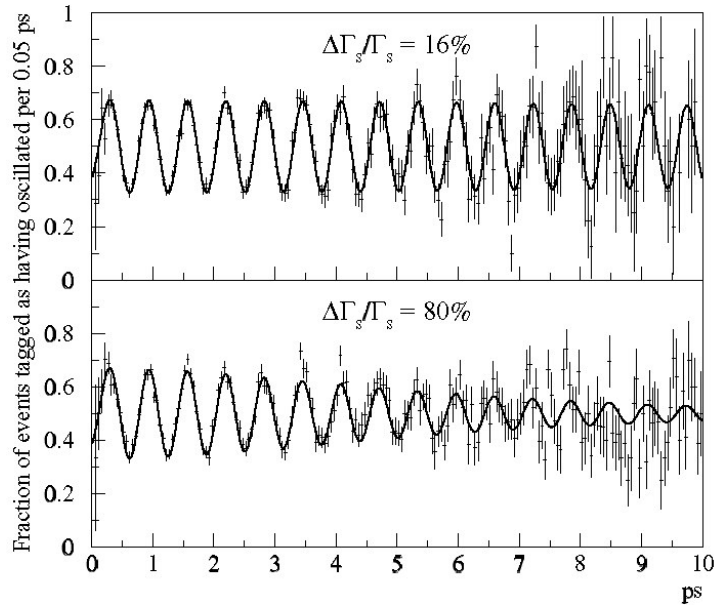
What is plotted here is not the asymmetry A_{mix} , but the related quantity

$$F_{mix}(t) = \frac{N_{ss}(t)}{N_{os}(t) + N_{ss}(t)} = \frac{1}{2} \cdot (1 - \cos(\Delta m t)) = \sin^2 \frac{\Delta m t}{2} \quad (10)$$

$$\Delta m_d = (0.503 \pm 0.064 \pm 0.071)/ps \quad (11)$$

Note that the ‘peak’ in the figure near $t = 0$ is due to background and has nothing to do with the oscillation. Details of this analysis: \rightarrow tutorial. So far the best B_d^0 oscillation measurements were performed with e^+e^- machines.

How the B_s mixing could be measured at the LHC is illustrated by the following curves, obtained in an ATLAS study:



The oscillation amplitude is damped due to backgrounds and wrong sign assignments (second B oscillates, muon from cascade decay $b \rightarrow c \rightarrow \mu^+, \dots$). Note that once the statistics is sufficient to see the oscillation, the period can be determined quite precisely from a \cos -fit. In both cases $\Delta m_s = 10/\text{ps}$ was assumed, but in the upper half of the plot the lifetime difference is small, while it is quite large in the lower half; in this case the simplified formulae can not be used any more and we must go back to formula (12) in section 2.1.4.1:

$$P_{B^0}(t) = \frac{1}{4} \cdot (e^{-\Gamma_1 t} + e^{-\Gamma_2 t} - 2e^{-\Gamma t} \cdot \cos(\Delta m t))$$

After a while only the $e^{-\Gamma t}$ term with the smaller Γ will survive and the oscillation term plays no role any more.

The implications of the Δm_d measurement on our knowledge of the CKM-Matrix are shown at the end of the next section.

2.1.5. CP violation

2.1.5.1 ‘The’ unitarity triangle

In the Standard Model CP violation is directly related to the non-vanishing complex phase δ in the unitary CKM matrix

$$V = \begin{pmatrix} V_{ud} & V_{us} & V_{ub} \\ V_{cd} & V_{cs} & V_{cb} \\ V_{td} & V_{ts} & V_{tb} \end{pmatrix} \quad (12)$$

which can be parametrised by three angles and one phase. Here we will use another (frequently used) parametrisation of V , invented by Wolfenstein:

$$V^W = \begin{pmatrix} 1 - \lambda^2/2 & \lambda & A\lambda^3\omega e^{-i\delta} \\ -\lambda & 1 - \lambda^2/2 & A\lambda^2 \\ A\lambda^3(1 - \omega e^{i\delta}) & -A\lambda^2 & 1 \end{pmatrix} + \mathcal{O}(\lambda^4) \quad \omega e^{-i\delta} = \rho - i\eta \quad (13)$$

Advantage: ‘Hierarchy’ is ‘built-in’. Numerically (from experimental data!): $A \approx 0.8$, $\lambda \approx 0.2$. Necessary condition of CPV: $\eta/\rho \neq 0$. Note that V^W is equal to V only up to $\mathcal{O}(\lambda^3)$. ρ and η are not known precisely - yet.

The phase can only be measured through an interference phenomenon, otherwise only the magnitude counts:

$$A \sim V_{xy} \quad \rightarrow \quad |A|^2 \sim |V_{xy}|^2 \quad (14)$$

$$A \sim V_{xy} + V_{ab} \quad \rightarrow \quad |A|^2 \sim |V_{xy}|^2 + |V_{ab}|^2 + V_{xy} V_{ab}^* + V_{xy}^* V_{ab} \quad (15)$$

Note that the vertex $q - W - q'$ is described by $V_{qq'}$ while for the antiquark vertex $\bar{q} - W - \bar{q}'$ the amplitude is proportional to $V_{qq'}^*$.

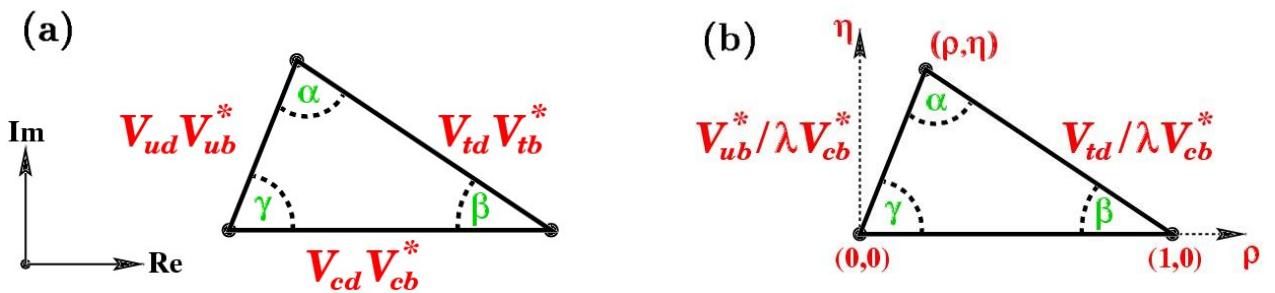
The unitarity condition $V^* \cdot V^T = 1$ implies six normalization relations like

$$1 = V_{cd} V_{cd}^* + V_{cs} V_{cs}^* + V_{cb} V_{cb}^* \equiv |V_{cd}|^2 + |V_{cs}|^2 + |V_{cb}|^2 \quad (16)$$

In these equations the complex phase drops out - thus they are not of interest here. They can be used to determine $\rho^2 + \eta^2$, but not η/ρ . This is different for the six orthogonality relations, for example

$$0 = V_{ud} V_{ub}^* + V_{cd} V_{cb}^* + V_{td} V_{tb}^* \quad (17)$$

This equation can be represented as a triangle in the complex plane⁴:



When dividing by $V_{cd} V_{cb}^*$ we arrive at figure (b). Here we have approximated $V_{ud} = 1$ and used $\lambda = V_{us} = -V_{cd}$:

$$0 = \frac{V_{ud} V_{ub}^*}{V_{cd} V_{cb}^*} + 1 + \frac{V_{td} V_{tb}^*}{V_{cd} V_{cb}^*} \rightarrow -\frac{V_{ub}^*}{\lambda V_{cb}^*} + 1 - \frac{V_{td}}{\lambda V_{cb}^*} \quad (18)$$

In Wolfenstein language, approximating $V_{ud} = 1 - \lambda^2/2 = 1$:

$$0 = -[\rho + i\eta] + 1 + [-(1 - \rho - i\eta)] \quad (19)$$

⁴Beware: real part of $V_{cd} V_{cb}^*$ is negative!

Thus, determination of the triangle means measuring ρ, η . Why is such a triangle interesting ?

- it is related to $\eta/\rho = \tan \delta$.
- its size and form can be measured through the lengths of their legs, (e.g. $|V_{td}/(\lambda V_{cb}^*)|$) - this does not require a CPV process!
- it can be measured via the angles, in a CP violating process
- comparing b) and c): important consistency check!

Out of the 6 unitarity triangles two are very similar (identical to $\mathcal{O}(\lambda^3)$) and it is sufficient to discuss one of them, which is (17). While all six triangles have the same area, the other four are ‘squashed’, that is two of the sides are much longer than the third one and/or all angles are close to $0^\circ, 90^\circ$ or 180° , example:

$$0 = V_{ud} V_{us}^* + V_{cd} V_{cs}^* + V_{td} V_{ts}^* \rightarrow (0.2) + (0.2) + (0.002) \quad (20)$$

But angles θ near $0^\circ, 90^\circ$ and 180° cannot be measured easily (CPV effect $\sim \sin 2\theta$), and it is also difficult to infer the smallest (least known) side from the two big ones.

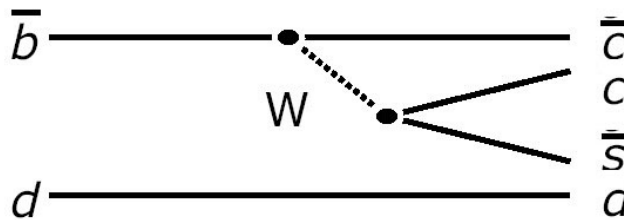
Therefore (17) is **the** unitarity triangle! Note that the three angles are given by

$$\frac{V_{td} V_{tb}^*}{V_{ud} V_{ub}^*} / \left| \frac{V_{td} V_{tb}^*}{V_{ud} V_{ub}^*} \right| = e^{-i\alpha} \quad \frac{V_{cd} V_{cb}^*}{V_{td} V_{tb}^*} / \left| \frac{V_{cd} V_{cb}^*}{V_{td} V_{tb}^*} \right| = e^{-i\beta} \quad \dots \quad (21)$$

2.1.5.2 CP violation in neutral B decays - theory

CPV is measurable through decays to CP eigenstates. The best (‘golden’) channel (relatively high branching fraction, good theoretical understanding) is

$$B_d^0, \overline{B}_d^0 \rightarrow J/\Psi K_s^0 \rightarrow l^+ l^- \pi^+ \pi^- \quad (22)$$



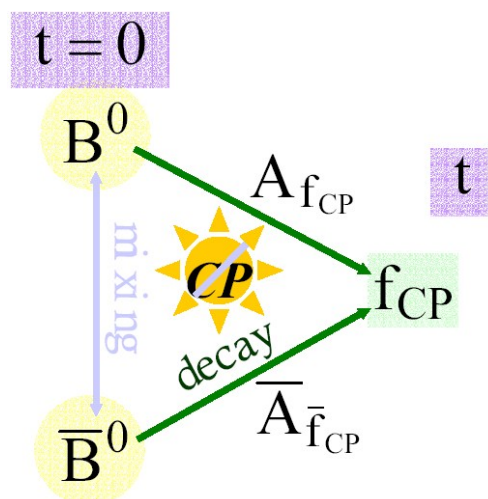
Since

$$CP(B^0) = \overline{B}^0 \quad CP(J/\Psi K_s^0) = J/\Psi K_s^0 \quad (23)$$

CP conservation implies **no** difference between B_0 and \overline{B}_0 decays into this final state.

In case of **CP violation** there are differences - but they are observable only if an interference phenomenon can be exploited - see above. Here there the two processes that interfere are:

- direct decay of B^0 into CP eigenstate
- oscillation of $B^0 \rightarrow \overline{B}^0$ and subsequent decay of \overline{B}^0 .

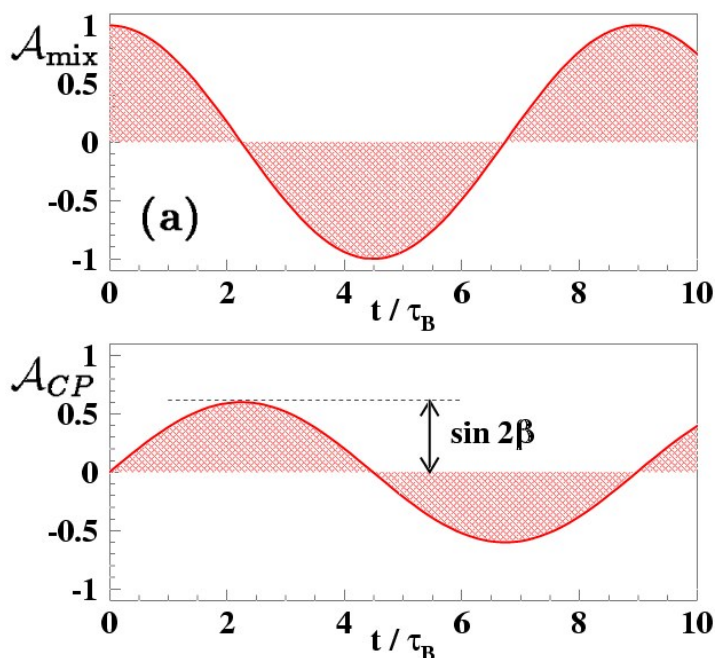


Note that the final state is in both cases the same and there is no way to distinguish between the two paths experimentally.

Thus oscillation plays a major role in this context! The CPV effect can be measured through the time dependent CP asymmetry

$$A_{CP}(t) = \frac{\overline{B}^0(t) - B^0(t)}{\overline{B}^0(t) + B^0(t)} = \text{const} \cdot \sin \Delta m_d t \quad (24)$$

Here $B^0(t)$ denotes the number of decays at proper time t for a meson that was a pure B^0 state at $t = 0$ (known from the second b), and $\overline{B}^0(t)$ is the probability number of decays at time t for an initially pure \overline{B}^0 state. The following graph illustrates on the top the mixing asymmetry and on the bottom the CP asymmetry, which is ‘out of phase’ by $\pi/2$: at the start we have a pure B^0 state and there is no CP violation; then, when A_{mix} is zero, we have equal amounts of B^0 and \overline{B}^0 , resulting in a maximum in A_{CP} .



How big is the amplitude *const* in equation (24) ? Some crude arguments: Three effects play a role, the direct decay $\sim V_{cb}V_{cs}^*$, the B^0 oscillation $\sim V_{tb}^*V_{td}$, and also the K^0 mixing $\sim V_{cs}V_{td}^*$. The ratio r of the amplitudes for $B^0 \rightarrow J/\Psi K^0$ and $\bar{B}^0 \rightarrow J/\Psi K^0$ is given by this expression:

$$\underbrace{\left(\frac{V_{tb}^*V_{td}}{V_{tb}V_{td}^*}\right)}_{B^0 \text{ mixing}} \underbrace{\left(\frac{V_{cb}V_{cs}^*}{V_{cb}^*V_{cs}}\right)}_{\text{Decay}} \underbrace{\left(\frac{V_{cs}V_{cd}^*}{V_{cs}^*V_{cd}}\right)}_{K^0 \text{ mixing}}$$

Thus

$$r = \frac{V_{cd}^*V_{cb}}{V_{td}^*V_{tb}} / \frac{V_{cd}V_{cb}^*}{V_{td}V_{tb}^*} = e^{2i\beta} \quad (25)$$

It is important to note that only CKM matrix elements enter and no QCD corrections - which can be large for other CP eigenstates! Therefore

$$\text{Im}(r) = \sin(2\beta) \quad (26)$$

It follows (without proof)

$$\text{const} = \sin(2\beta) \quad (27)$$

PS: CPV in the B_s meson system is expected to be much smaller than for B_d^0 , and is therefore not discussed here. Instead of K_s^0 also K_l^0 could be used, but it is experimentally disfavored (decay into pions rarely observable).

2.1.5.3 CP violation in neutral B decays - experiments

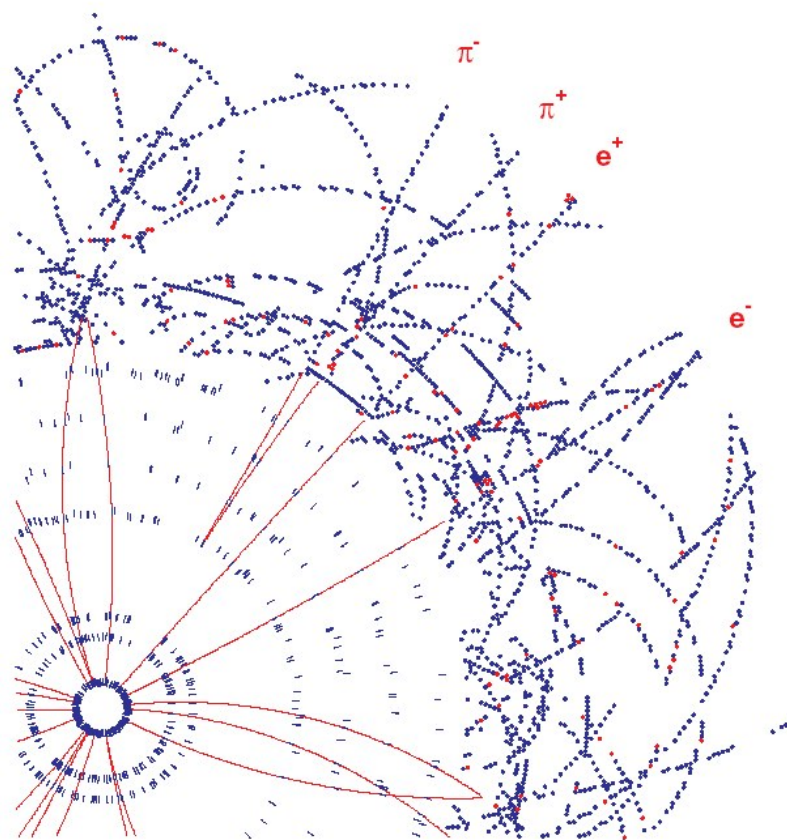
The decay into $J/\Psi K^0$ has been measured in many experiments, in spite of the rather small branching fractions

$$BR(B^0 \rightarrow J/\Psi K^0) = 0.09\% \quad BR(J/\Psi \rightarrow \mu^+\mu^-) = 6\% \quad (28)$$

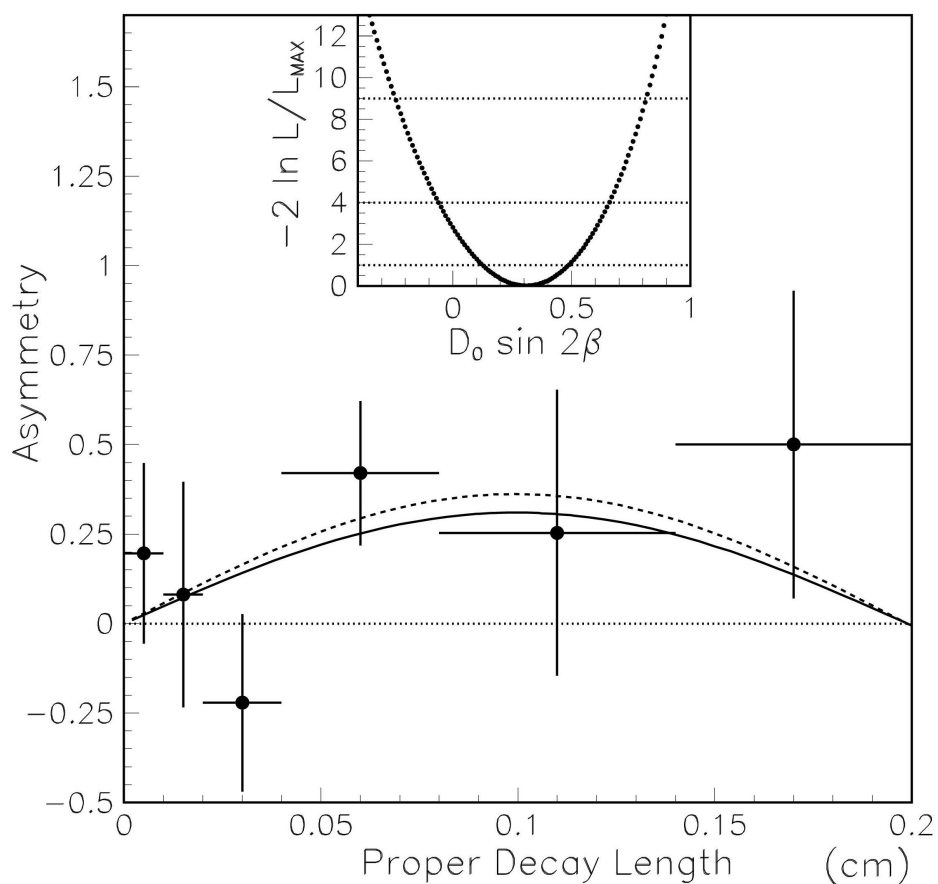
The following graph shows a simulated ATLAS event where the J/Ψ decays into an e^+e^- pair.

ATLAS Barrel Inner Detector

$$B_d^0 \rightarrow J/\psi K_s^0 L = 5 \times 10^{33} \text{ cm}^{-2} \text{ s}^{-1}$$



The CP asymmetry has been measured by several collaborations, including CDF (via $J/\Psi \rightarrow \mu^+ \mu^-$).



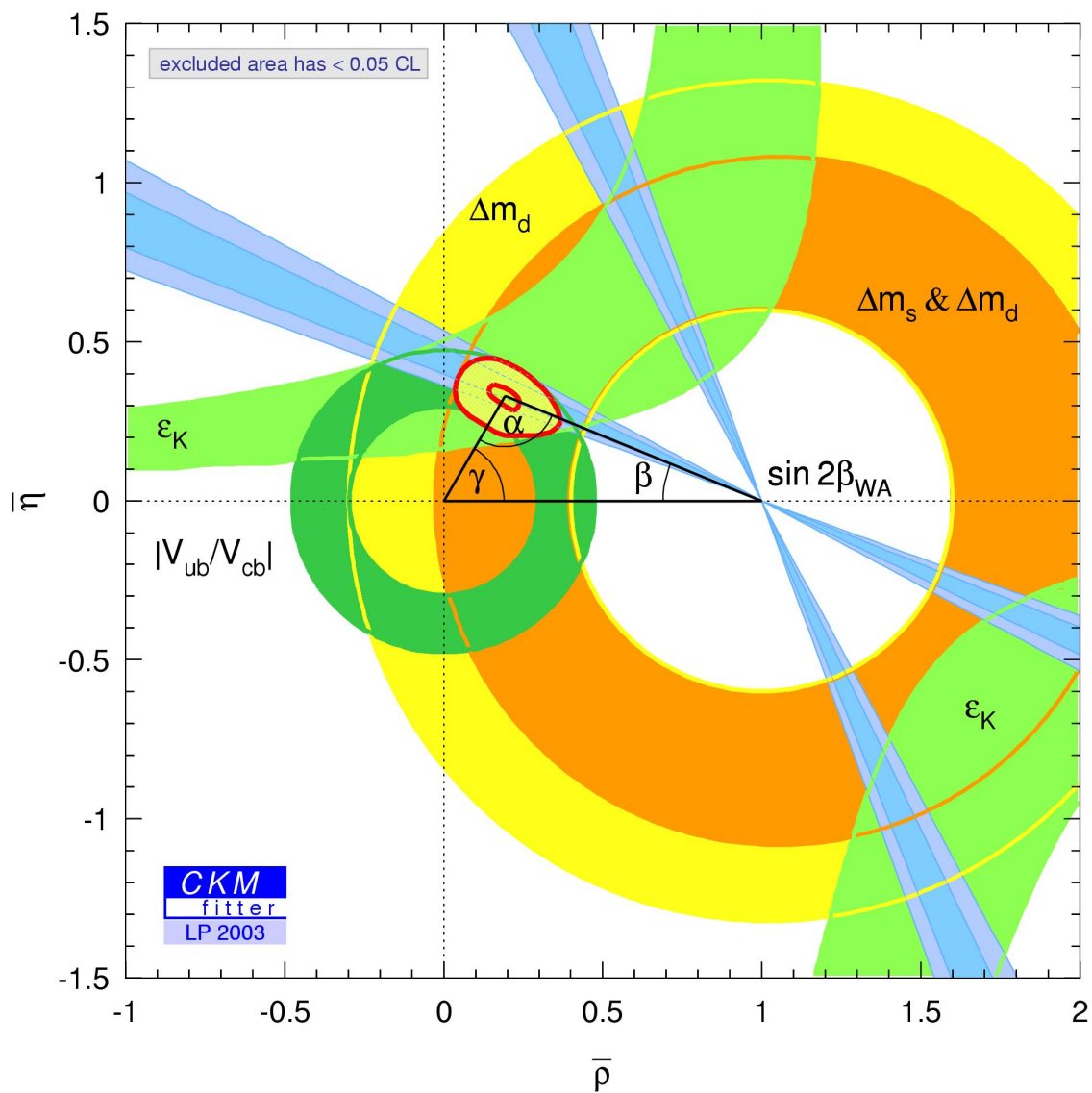
About 200 neutral B events have been used for this analysis. The insert shows the result of the fit, including a dilution factor D_0 . The latest CDF number (run I) is $\sin 2\beta = 0.79^{+0.41}_{-0.44}$. At the moment the best results come from the e^+e^- experiments Babar and Belle, dominating the world average of

$$\sin(2\beta) = 0.701 \pm 0.053 \quad (29)$$

Clearly, CP violation is established in the B_d^0 system.

2.1.5.4 The unitarity triangle in 2003

Finally we summarize the experimental knowledge on the unitarity triangle:



Here $\bar{\rho} = \rho(1 - \lambda^2/2) \sim \rho$ and $\bar{\eta} = \eta(1 - \lambda^2/2) \sim \eta$. Note that all the different measurements are consistent within this framework, a major success of the Standard Model!

2.2. Supersymmetry

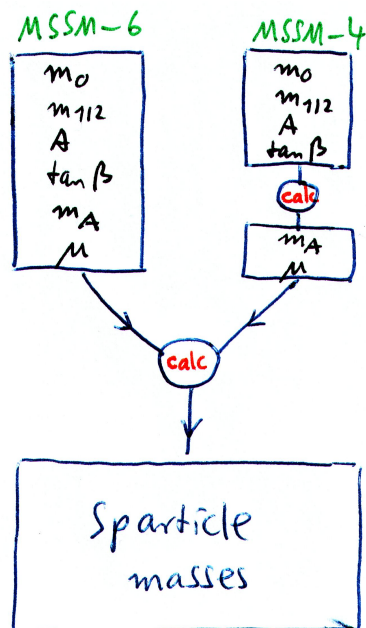
References:

- H.E. Haber and G.L. Kane, 'The Search for Supersymmetry: Probing Physics Beyond the Standard Model', Phys. Rep. 117 (1985) 75.
- Stephen P. Martin, 'A Supersymmetry primer', hep-ph/9709356
- W. de Boer, 'Grand Unified Theories and Supersymmetry in Particle Physics and Cosmology', hep-ph/9402266
- Review of Particle Physics, Phys. Rev. D (2002) 1
- L. Roszkowski et al, 'New Cosmological and Experimental Constraints on the MSSM', hep-ph/0106334
- M. Battaglia et al, 'Updated Post-WMAP Benchmarks for Supersymmetry', hep-ph/0306219

Web form to calculate SUSY parameters:

<http://www.phys.ufl.edu/~jblender/isajet/isajet.html>

I consider only models with 'gravity mediated supersymmetry breaking' without R parity violation. There are two variants, which are often discussed in the literature and for which many experimental and cosmological constraints have been evaluated. The more general one, here called MSSM-6, depends on 6 free parameters, the other one, MSSM-4, on 4 (plus a sign); we will discuss the corresponding parameters below¹. MSSM stands for 'Minimal Supersymmetric Extension of the Standard Model'; 'minimal' refers to the particle content.



¹The nomenclature is not very uniform in the literature: the names CMSSM and MSUGRA are often used.

Additional constraints from cosmology are often imposed: dark matter = LSP = $\tilde{\chi}_1^0 \equiv \tilde{\chi}_1$.

Even in the MSSM-4 (to be explored here) it takes a beginner some time to ‘understand’ the parameter space. In order to move in this direction we will in the following:

- start from two ‘benchmark scenarios’ (= two points in the MSSM-4 parameter space),
- calculate the corresponding SUSY masses, and
- explore the associated cross sections and branching fractions (as far as they are relevant for the Tevatron/LHC).

But first of all we list the particle content of the minimal SUSY model²:

Particle	Spin	Susy-Partner	Spin
ν_e	1/2	$\tilde{\nu}_e^L$	0
e^-	1/2	$\tilde{e}_L^-, \tilde{e}_R^-$	0
u	1/2	\tilde{u}_L, \tilde{u}_R	0
d	1/2	\tilde{d}_L, \tilde{d}_R	0
γ, Z, h, H, A	1, 0	$\tilde{\chi}_1^0, \tilde{\chi}_2^0, \tilde{\chi}_3^0, \tilde{\chi}_4^0$	1/2
W^\pm, H^\pm	1, 0	$\tilde{\chi}_1^\pm, \tilde{\chi}_2^\pm$	1/2
g	1	\tilde{g}	1/2

The number of degrees of freedom is the same on the left and on the right, line by line. Note that (at least) five physical higgs fields, h, A, H, H^\pm are required. While the lightest higgs h plays a central role in SUSY searches, due to its theoretical mass constraint of $\leq 130 \text{ GeV}$, we will focus here on the particles with the quantum number R parity = -1 , while ‘normal’ particles and all higgs bosons have $R = 1$.

2.2.1 MSSM-parameters

In the MSSM-6 there are six parameters beyond the Standard Model parameters (however, the higgs mass is now predicted as a function of the SUSY parameters). The parameters are:

- common scalar mass m_0 for all sfermions at GUT scale
- common gaugino mass $m_{1/2}$ for all gauginos at GUT scale
- higgs mass m_A
- higgsino mass parameter μ (at elw. scale)
- universal trilinear coupling A_0 at GUT scale
- ratio of higgs vacuum expectation values $\tan \beta$ (at elw. scale)

It is very important to realize at which energy scale these numbers are defined, see below.

²Probably right handed neutrinos need to be added. . .

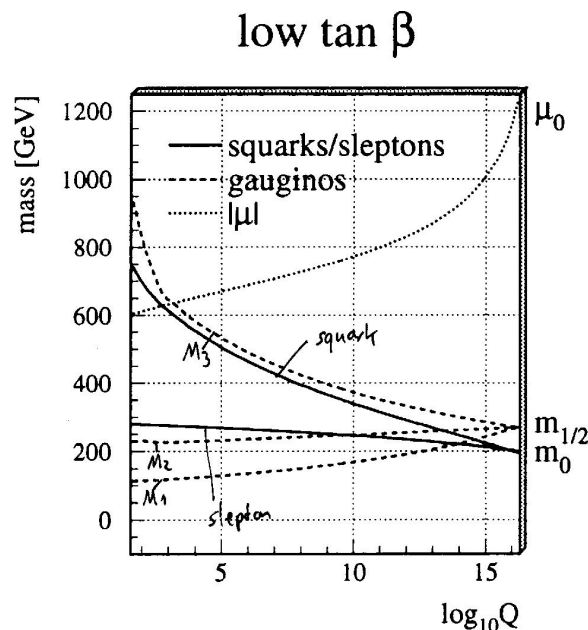
Remarks:

- The masses and A are ‘soft supersymmetry breaking parameters’ - they are arbitrary constants in an effective Lagrangian compatible with SUSY breaking - since we don't know more about it!
- In SUSY at least two higgs doublets are required, the corresponding vacuum expectation values are v_u and v_d , where, as in the Standard Model, $v_u^2 + v_d^2 \equiv v^2 = 1/(\sqrt{2}G_F) = (246 \text{ GeV})^2$ is fixed while their ratio $(v_u = v \sin \beta)/(v_d = v \cos \beta) = \tan \beta$ is a free parameter. β appears in many formulae, since the higgs couplings determine masses and radiative corrections as well as cross sections and decay rates.
- all higgs masses are fixed by m_A and $\tan \beta$. Example (lowest order): $m_{H^\pm}^2 = m_W^2 + m_A^2$
- the higgsino mass parameter μ determines the higgsino masses - however the situation is more complicated due to the mixing with the gauginos.
- the ‘trilinear coupling’ A describes the strength of the sfermion-higgs couplings, similar to the Yukawa couplings in the fermion-higgs term in the SM. Thus A influences the sfermion masses, see below.

The underlying assumptions in the MSSM-6 are:

- no CPV (beyond SM)
- grand unification of couplings at $\sim 10^{16} \text{ GeV}$
- universal mass for sfermions and universal trilinear coupling at the GUT scale
- universal gaugino mass at the GUT scale \rightarrow GUT inspired relation between the gaugino masses at elw. scale

The energy scale dependence of SUSY mass parameters is illustrated here (from R. Ehret):



Here masses denoted by a capital M are gaugino masses at the elw. scale. Running implies quantitatively for the SU(2) gaugino:

$$M_2 = 0.82 m_{1/2} \quad (1)$$

The beforementioned gaugino mass relations are:

$$M_1 = \frac{5}{3} \tan^2 \theta_W \cdot M_2 \approx 0.4 \cdot m_{1/2} \quad (2)$$

$$M_3 = \frac{\alpha_s}{\alpha} \sin^2 \theta_W \cdot M_2 \approx 3 \cdot m_{1/2} \quad (3)$$

where M_1 and $M_3 = m_{\tilde{g}}$ are the U(1) and SU(3) gaugino masses.

Furthermore we constrain the parameter space by excluding all points where the lightest SUSY Particle (LSP) is **not** neutral (charge and color), so that dark matter can be explained by SUSY. Since sneutrinos tend to be relatively heavy, this implies $LSP = \tilde{\chi}_1$.

What are the allowed values for the six (four) parameters ? There is no exact answer! In order to avoid the higgs mass hierarchy problem, one must have SUSY masses below 1 TeV, thus the dimensionful parameters like m_0 cannot be much larger. For $\tan \beta$ one chooses values between 1 and $\sim 35 = m_t/m_b$, since in models with a universal Yukawa coupling the quark masses are proportional to v_u and v_d . So:

$$\begin{array}{ll} m_0 & 0 - 2 \text{ TeV} \\ m_{1/2} & 0 - 2 \text{ TeV} \\ m_A & 0 - 2 \text{ TeV} \\ |A| & 0 - 2 \text{ TeV} \\ |\mu| & 0 - 2 \text{ TeV} \\ \tan \beta & 1 - 50 \end{array}$$

Low values of the mass parameters as well as the regime $\tan \beta < 3$ are already excluded experimentally.

So far we discussed the MSSM-6 model. Two additional constraints allow to calculate m_A and $|\mu|$ from the other parameters, thus bringing us to the MSSM-4:

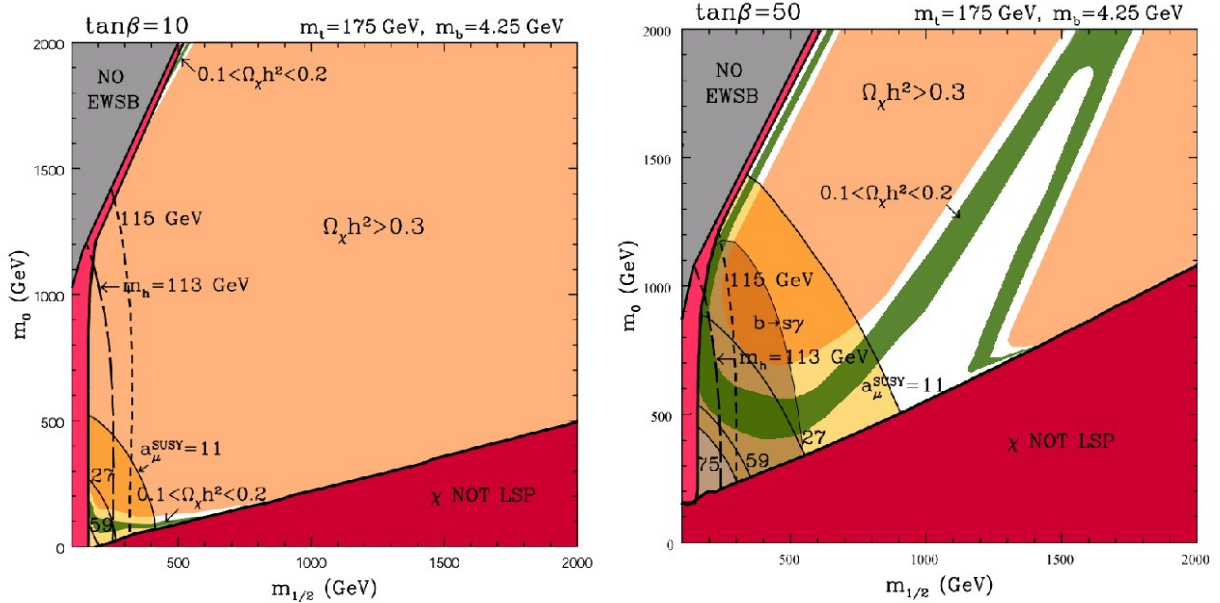
- a) also the higgs masses (scalar particles!) are determined by m_0
- b) electroweak (!) symmetry breaking occurs automatically via radiative corrections influencing the higgs potential. This implies a relation fixing μ^2 .

Therefore, in the MSSM-4 there are four independent parameters (see figure above) and the sign of μ^3 .

2.2.2 MSSM benchmark scenarios

Several groups have analysed the existing experimental (LEP, $b \rightarrow s \gamma$, $g_\mu - 2 \dots$) and cosmological constraints (WMAP: $\Omega_{dark} h^2 \sim 0.1$) and have calculated the remaining 'allowed' regions in the MSSM-4 parameter space. Example (L. Roszkowski et al):

³Since mass terms in the Lagrangian are $\sim m^2$ the value of m may be negative. It turns out that only a relative sign between $m_{1/2}$ and μ matters; by convention $m_{1/2} > 0$



In both cases $\mu > 0$ was assumed. We will restrict ourselves to this case, since $\mu < 0$ is disfavored by measurements of $g_\mu - 2$. The limits shown here are not very sensitive to A , so this parameter was set to 0.

It must be stressed, that different authors arrive at different contours (calculations of Ω_{dark} are difficult!) and that variations of standard model parameters (e.g. $m_{top} = (175 \pm 5)$ GeV) can have dramatic effects on the contours in the $m_0 - m_{1/2}$ plane, in particular at high values of $\tan \beta$.

In some of those papers analyzing the MSSM-4 parameter space some ‘representative’ benchmark scenarios have been proposed, typically 10, which are scattered over the *allowed* parameter region. They are further investigated in view of the experimental possibilities at existing and future colliders.

We will pick up one proposal (M. Battaglia et al, table 2, reproduced in the appendix of this lecture note) and have a closer look at the following two points in parameter space (terminology taken from that table):

	B'	L'
m_0/GeV	57	303
$m_{1/2}/\text{GeV}$	250	450
$\tan \beta$	10	47
A/GeV	0	0

Note that low values of $\tan \beta$ are not considered, since they are already excluded.

2.2.3 SUSY masses

If we want to calculate masses, we need to compute μ and m_A first. Since both are related to Higgs masses, which ‘suffer’ heavily from radiative corrections, a simple tree level formula is not sufficient. Instead one can use the following crude ($\pm 10\%$) approximations:

$$\mu^2 = \left(\frac{2100}{\tan^2 \beta} - 1.0 \right) \cdot m_0^2 + \left(\frac{-60}{\tan^2 \beta} + 1.2 \right) \cdot m_{1/2}^2 + 49000 \text{ GeV}^2 \quad (4)$$

$$m_A^2 = \left(\frac{5700}{\tan^2 \beta} - 3.5 \right) \cdot m_0^2 + \left(\frac{-160}{\tan^2 \beta} + 1.3 \right) \cdot m_{1/2}^2 + 18000 \text{ GeV}^2 \quad (5)$$

yielding

	B'	L'
μ/GeV	389	501
m_A/GeV	416	427

Alternatively one can simply use the values from the appendix, as we will do for the following computations.

2.2.3.1 Fermion masses

Sparticle masses at the electroweak scale are given by the general formula:

$$m^2(\tilde{f}) - m^2(f) = m_0^2 + \Delta_{gauge} \quad (6)$$

Δ_{gauge} describes the running from GUT to ELW scales, determined by the coupling to the different gauge fields:

$$\Delta_{gauge} = \Delta_{SU(3)} + \Delta_{SU(2)} + \Delta_{U(1)} \quad (7)$$

The individual terms are proportional to the corresponding gaugino mass squared and the sfermion-gaugino coupling². With GUT assumptions:

$$\Delta_{SU(3)} = N_C^2 \cdot 0.91 M_2^2 \quad (8)$$

$$\Delta_{SU(2)} = T^2 \cdot 2.96 M_2^2 \quad (9)$$

$$\Delta_{U(1)} = Y^2 \cdot 0.22 M_2^2 \quad (10)$$

Note the dependence on weak isospin T and weak hypercharge $Y = Q - T_3$. Since left- and right handed fermions differ in these quantum numbers, also the corresponding SUSY masses are different from each other:

$$m^2(\tilde{u}_L) - m^2(u) = m_0^2 + 8.95 M_2^2 \quad (11)$$

$$m^2(\tilde{d}_L) - m^2(d) = m_0^2 + 8.95 M_2^2 \quad (12)$$

$$m^2(\tilde{\nu}) = m_0^2 + 0.80 M_2^2 \quad (13)$$

$$m^2(\tilde{e}_L) - m^2(e) = m_0^2 + 0.80 M_2^2 \quad (14)$$

$$m^2(\tilde{u}_R) - m^2(u) = m_0^2 + 8.30 M_2^2 \quad (15)$$

$$m^2(\tilde{d}_R) - m^2(d) = m_0^2 + 8.22 M_2^2 \quad (16)$$

$$m^2(\tilde{e}_R) - m^2(e) = m_0^2 + 0.22 M_2^2 \quad (17)$$

However, the situation is more complicated; the mass matrix contains also non diagonal terms. For 'up' type fermions:

$$\begin{pmatrix} m_L^2(\tilde{f}) & m_f \cdot (A - \mu \cot \beta) \\ m_f \cdot (A - \mu \cot \beta) & m_R^2(\tilde{f}) \end{pmatrix} \quad (18)$$

Mass matrix for ‘down’ type fermions:

$$\begin{pmatrix} m_L^2(\tilde{f}) & m_f \cdot (A - \mu \tan \beta) \\ m_f \cdot (A - \mu \tan \beta) & m_R^2(\tilde{f}) \end{pmatrix} \quad (19)$$

The sfermion fields \tilde{f}_R and \tilde{f}_L mix into observable mass eigenstates $\tilde{f}_1 < \tilde{f}_2$:

$$\tilde{f}_1 = \tilde{f}_L \cos \theta + \tilde{f}_R \sin \theta \quad (20)$$

$$\tilde{f}_2 = -\tilde{f}_L \sin \theta + \tilde{f}_R \cos \theta \quad (21)$$

Note: This ‘mixing’ is relevant only if m_f is large, i.e. for $\tilde{\tau}, \tilde{b}, \tilde{t}$. The masses m_1 and m_2 and the mixing angle θ can be calculated by diagonalizing the mass matrix:

$$m_{1,2}^2 = \frac{1}{2}(m_R^2 + m_L^2) \mp \sqrt{(m_L^2 - m_R^2)^2/4 + (m_f(A - \mu \cot \beta))^2} \quad (22)$$

for ‘up’ and similarly for ‘down’.

Applying the sfermion mass formulae to our benchmark scenario, we get

	B'	L'
$m(\tilde{\nu})/\text{GeV}$	191	447
$m(\tilde{e}_L)/\text{GeV}$	191	447
$m(\tilde{e}_R)/\text{GeV}$	112	349
$m(\tilde{d}_L)/\text{GeV}$	616	1145
$m(\tilde{d}_R)/\text{GeV}$	591	1101
$m(\tilde{u}_L)/\text{GeV}$	616	1145
$m(\tilde{u}_R)/\text{GeV}$	593	1105
$m(\tilde{\tau}_1)/\text{GeV}$	105	316
$m(\tilde{\tau}_2)/\text{GeV}$	195	471
$m(\tilde{b}_1)/\text{GeV}$	586	1066
$m(\tilde{b}_2)/\text{GeV}$	621	1177
$m(\tilde{t}_1)/\text{GeV}$	618	1119
$m(\tilde{t}_2)/\text{GeV}$	641	1158

These numbers are in reasonable agreement with the expert’s results as given in the appendix.

In these examples the mixing between sfermions \tilde{f}_L and \tilde{f}_R is small; for other parameters it can be large and the lightest stop \tilde{t}_1 might be the lightest squark!

2.2.3.2 Gaugino masses

Here ‘mixing’ has to be taken into account.

To determine the neutralino masses, we start with the fields

$$(\tilde{B}, \tilde{W}^3, \tilde{H}_u^0, \tilde{H}_d^0) \quad (23)$$

the corresponding mass matrix reads

$$\begin{pmatrix} M_1 & 0 & -M_Z \cos \beta \sin \theta_W & M_Z \sin \beta \sin \theta_W \\ 0 & M_2 & M_Z \cos \beta \cos \theta_W & -M_Z \sin \beta \cos \theta_W \\ -M_Z \cos \beta \sin \theta_W & M_Z \cos \beta \cos \theta_W & 0 & -\mu \\ M_Z \sin \beta \sin \theta_W & -M_Z \sin \beta \cos \theta_W & -\mu & 0 \end{pmatrix} \quad (24)$$

The off diagonal elements are due to gaugino-higgs-higgsino couplings. With the GUT gaugino mass relations and $\sin^2 \theta_W = 0.23$:

$$\begin{pmatrix} 0.4 m_{1/2} & 0 & -0.48 \cos \beta M_Z & 0.48 \sin \beta M_Z \\ 0 & 0.8 m_{1/2} & 0.88 \cos \beta M_Z & -0.88 \sin \beta M_Z \\ -0.48 \cos \beta M_Z & 0.88 \cos \beta M_Z & 0 & -\mu \\ 0.48 \sin \beta M_Z & -0.88 \sin \beta M_Z & -\mu & 0 \end{pmatrix} \quad (25)$$

After diagonalization one obtains the mass eigenstates

$$\tilde{\chi}_1^0, \tilde{\chi}_2^0, \tilde{\chi}_3^0, \tilde{\chi}_4^0 \quad (26)$$

and the rotation matrices, which tell us the composition of the neutralinos in terms of bino, wino and higgsino fields. This is quite important, since the coupling (neutralino-particle-sparticle and gaugeboson-neutralino-neutralino) is quite different for these fields. For example: a higgsino couples preferentially to heavy particles, the photino (mixture of \tilde{B} and \tilde{W} , as in SM) does not couple to the Z.

In the limit $M_Z \ll |\mu \pm M_1|, |\mu \pm M_2|$ the neutralino mass matrix is considerably simplified, since the terms $\sim M_Z$ can be neglected. In that case the LSP mass $m(\tilde{\chi}_1)$ is $0.4 m_{1/2}$ if μ if $m_{1/2} \gg |\mu|$. If $m_{1/2} \ll |\mu|$ we have also the following nice approximate relation: $m(\tilde{\chi}_2) \approx m(\tilde{\chi}_1^\pm) = 2 m(\tilde{\chi}_1)$.

Similarly, to compute chargino masses and composition, the matrix

$$\begin{pmatrix} M_2 & \sqrt{2} M_W \sin \beta \\ \sqrt{2} M_W \cos \beta & \mu \end{pmatrix} \quad (27)$$

must be diagonalized, giving⁴

$$m^2(\tilde{\chi}_1^\pm, \tilde{\chi}_2^\pm) = 0.5 \cdot [M_2^2 + \mu^2 + 2M_W^2] \quad (28)$$

$$\mp \sqrt{(M_2^2 - \mu^2)^2 + 4M_W^4 \cos^2(2\beta) + 4M_W^2(M_2^2 + \mu^2 + 2M_2 \mu \sin(2\beta))} \quad (29)$$

For the benchmark points we find with these formulae:

	B'	L'
$m(\tilde{\chi}_1)/\text{GeV}$	99	184
$m(\tilde{\chi}_2)/\text{GeV}$	186	356
$m(\tilde{\chi}_3)/\text{GeV}$	345	568
$m(\tilde{\chi}_4)/\text{GeV}$	367	581
$m(\tilde{\chi}_1^\pm)/\text{GeV}$	185	501
$m(\tilde{\chi}_2^\pm)/\text{GeV}$	386	501

Example for composition: In model L' the LSP is

$$\tilde{\chi}_1 = 0.995 \tilde{B} - 0.014 \tilde{W}^3 + 0.090 \tilde{H}_u^0 - 0.031 \tilde{H}_d^0 \quad (30)$$

It is dominantly 'gaugino' ('bino'), and not 'higgsino'.

⁴The chargino mixing is a bit more involved, see article by S.P. Martin, section 7.3

APPENDIX

from M. Battaglia et al, hep-ph/0306219

Supersymmetric spectra in post-WMAP benchmarks
calculated with ISASUGRA 7.67

Model	A'	B'	C'	D'	E'	F'	G'	H'	I'	J'	K'	L'	M'
$m_{1/2}$	600	250	400	525	300	1000	375	935	350	750	1300	450	1840
m_0	107	57	80	101	1532	3440	113	244	181	299	1001	303	1125
$\tan\beta$	5	10	10	10	10	10	20	20	35	35	46	47	51
$\text{sign}(\mu)$	+	+	+	-	+	+	+	+	+	+	-	+	+
m_t	175	175	175	175	171	171	175	175	175	175	175	175	175
Masses													
$ \mu(m_Z) $	773	339	519	663	217	606	485	1092	452	891	1420	563	1940
h	116	113	117	117	114	118	117	122	117	121	123	118	124
H	896	376	584	750	1544	3525	525	1214	444	888	1161	480	1623
A	889	373	580	745	1534	3502	522	1206	441	882	1153	477	1613
H^\pm	899	384	589	754	1546	3524	532	1217	453	892	1164	490	1627
χ	242	95	158	212	112	421	148	388	138	309	554	181	794
χ_2	471	180	305	415	184	610	286	750	266	598	1064	351	1513
χ_3	778	345	525	671	229	622	492	1100	459	899	1430	568	1952
χ_4	792	366	540	678	302	858	507	1109	475	908	1437	582	1959
χ_1^\pm	469	178	304	415	175	613	285	750	265	598	1064	350	1514
χ_2^\pm	791	366	541	679	304	846	507	1108	475	908	1435	582	1956
\tilde{g}	1367	611	940	1208	800	2364	887	2061	835	1680	2820	1055	3884
e_L, μ_L	425	188	290	376	1543	3499	285	679	304	591	1324	434	1660
e_R, μ_R	251	117	174	224	1534	3454	185	426	227	410	1109	348	1312
ν_e, ν_μ	412	167	274	362	1539	3492	270	665	290	579	1315	423	1648
τ_1	249	109	167	217	1521	3427	157	391	150	312	896	194	796
τ_2	425	191	291	376	1534	3485	290	674	312	579	1251	420	1504
ν_τ	411	167	273	360	1532	3478	266	657	278	558	1239	387	1492
u_L, c_L	1248	558	859	1103	1639	3923	814	1885	778	1554	2722	1001	3670
u_R, c_R	1202	542	830	1064	1637	3897	787	1812	754	1497	2627	969	3528
d_L, s_L	1250	564	863	1107	1641	3924	818	1887	783	1556	2723	1004	3671
d_R, s_R	1197	541	828	1059	1638	3894	786	1804	752	1491	2615	967	3509
t_1	958	411	653	860	1052	2647	617	1477	584	1207	2095	753	2857
t_2	1184	576	837	1048	1387	3373	792	1753	748	1428	2366	920	3231
b_1	1147	514	789	1015	1375	3356	737	1719	677	1377	2297	844	3149
b_2	1181	535	816	1043	1602	3816	770	1761	725	1423	2349	904	3217

Table 2: Proposed post-WMAP CMSSM benchmark points and mass spectra (in GeV), as calculated using ISASUGRA 7.67 [20] and adapting the values of m_0 and $\tan\beta$ (when it is large) to give the best fit to the SSARD spectra shown in Table 1, as described in the text.

2.2.4 Collider cross sections and branching fractions

2.2.4.1 Rough estimate of cross sections

To get a rough idea about the order of magnitude of SM and other cross sections we consider as 'reference process' $e^+e^- \rightarrow \mu^+\mu^-$ via s channel photon exchange, with the well known total cross section

$$\sigma_{ref}^{elw} = \frac{4\pi}{3} \frac{1}{s'} \alpha^2 \approx 0.1 \text{ pb} \cdot \frac{(1 \text{ TeV})^2}{s'} \quad (1)$$

s' is the center of mass energy of the colliding elementary fermions. Of course, this expression is not valid for quarks, since they have smaller charges. But these factors are of the order of 1 and will be neglected here.

Electroweak processes are interesting for us only for effective collision energies $> M_W, M_Z$, since we are looking for heavy particles. Furthermore the weak couplings are of the same order as the electromagnetic coupling (electroweak unification!), so that formula (1) can be used also for W and Z exchange.

Strong processes differ mainly due to the higher coupling constant, so the reference cross section must be multiplied by $(\alpha_s/\alpha)^2$. Additional vertex factors are of $\mathcal{O}(1)$ and will be ignored.

$$\sigma_{ref}^{QCD} \approx \sigma_{ref} \frac{\alpha_s^2}{\alpha^2} \approx 20 \text{ pb} \cdot \frac{(1 \text{ TeV})^2}{s'} \quad (2)$$

When will our formulae fail? Certainly for resonance production (e.g. Z'), for t-channel processes with small energy transfer ...

So far we have ignored the kinematical suppression due to final state masses m_i not negligible with respect to $\sqrt{s'}$. Here we approximate this effect by a step function:

$$\sigma = \begin{cases} 0 & \sqrt{s'} < 2 \sum m_i \equiv s_{thr} \\ \sigma_{ref} & \sqrt{s'} \geq 2 \sum m_i \equiv s_{thr} \end{cases} \quad (3)$$

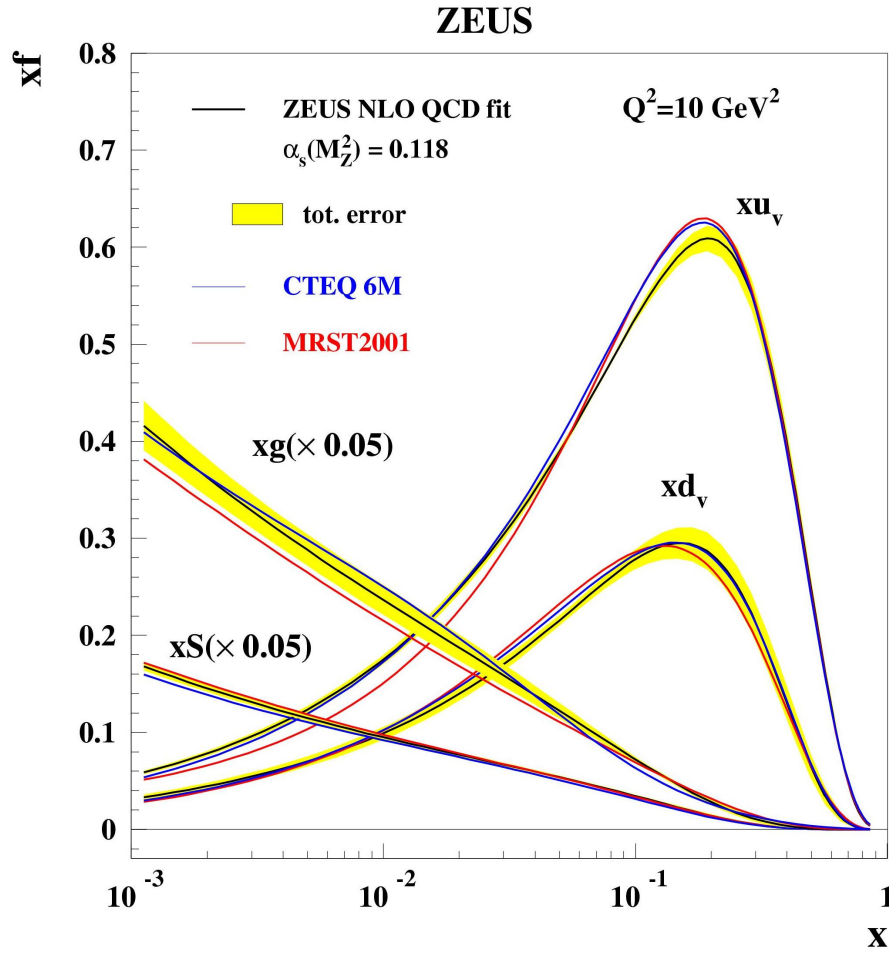
Finally we have to know the relation between s and s' , which is given by the structure functions:

$$s' = s \cdot x_1 x_2 \quad (4)$$

We assume that the process is only possible if both x_i fulfill

$$x_i > x_{thr} \equiv \sqrt{\frac{s_{thr}}{s}} \quad (5)$$

Since the dominant contributions come from s' values near s_{thr} we insert s_{thr} into formulae (1) or (2). The corresponding probabilities are given by the structure functions,



which we approximate (see figure) in the following way, in the range $x_i = 0.01 - 0.5$:

$$f_q(x) = 10 \cdot (-0.045 - 0.15 \log_{10} x)/x \quad (6)$$

$$f_g(x) = 20 \cdot (-0.045 - 0.15 \log_{10} x)/x \quad (7)$$

and ignore the Q^2 dependence. f_q denotes the sum of all sea quarks, which dominate at low x relative to the valence quarks.

Altogether, we expect that cross section estimates based on these approximations will be ok within a factor of 10 or so.

Example: Top pair cross section at LHC. Literature tells us that gg annihilation is the dominant contribution:

$$\sigma = 20 \text{ pb} \cdot \left(\frac{1000 \text{ GeV}}{700 \text{ GeV}} \right)^2 \cdot 3.2^2 = 400 \text{ pb} \quad (8)$$

The last factor

$$P_{struct} \equiv \left(\int_{x_{thr}}^1 f_g(x) dx \right)^2 = 3.2^2 \quad x_{thr} = 0.05 \quad (9)$$

contains the probability to find partons (gluons) with a sufficient momentum inside the protons. A full calculation yields **800 pb** (LHC).

2.2.4.2 SUSY cross sections

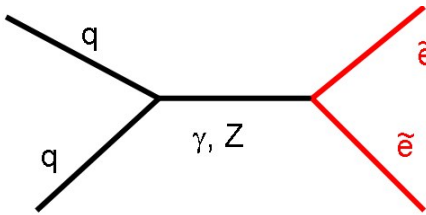
The following table shows selected cross sections calculated with Pythia for the Tevatron conditions and for the LHC.

	Tevatron		LHC	
	B'	L'	B'	L'
$\tilde{\chi}_1 \tilde{\chi}_1$	0.001 pb	< 0.001 pb	0.001 pb	0.0014 pb
$\tilde{\chi}_1 \tilde{\chi}_1^\pm$	0.002 pb	< 0.001 pb	0.014 pb	0.002 pb
$\tilde{\chi}_2 \tilde{\chi}_1^\pm$	0.07 pb	0.001 pb	1.3 pb	0.090 pb
$\tilde{t} \tilde{t}$	0.001 pb	-	1.7 pb	0.053 pb
$\tilde{e}^+ \tilde{e}^-$	0.009 pb	0.0006 pb	0.12 pb	0.004 pb
$\tilde{g} \tilde{g}$	-	-	4.0 pb	0.090 pb

This table shows that at Tevatron it will be difficult to test these scenarios, while at LHC there will be no problem to find or exclude SUSY for both parameter sets.

Can we understand these xsections (absolutely) ?

We estimate the selectron cross section (sum of $\tilde{e}_L \tilde{e}_L$ and $\tilde{e}_R \tilde{e}_R$) at the LHC in scenario L':



With a mass of ~ 400 GeV we get

$$\sigma = 0.1 \text{ pb} \cdot \left(\frac{1000 \text{ GeV}}{1600 \text{ GeV}} \right)^2 \cdot 0.74^2 = 0.02 \text{ pb} \tag{10}$$

$$P_{struct} \equiv \left(\int_{x_{thr}}^1 f_q(x) dx \right)^2 = 0.74^2 \quad x_{thr} = 0.11 \tag{11}$$

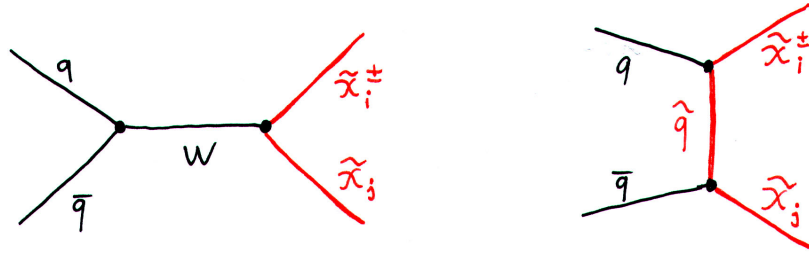
is smaller than for the top production, since there are less sea quarks than gluons and since the selectrons are heavier than top quarks. This is the right order of magnitude!

Can we understand the relative size of the different cross sections ?

Most intriguing is the very small value for $\tilde{\chi}_1 \tilde{\chi}_1$ compared to $\tilde{\chi}_2 \tilde{\chi}_1^\pm$, in spite of the mass differences. The following feynman diagrams contribute (to lowest order):



¹ $\sigma(\tilde{\chi}_1 \tilde{\chi}_1)$ and $\sigma(\tilde{\chi}_1 \tilde{\chi}_1^\pm)$ are small, too!



The t (and u) channel processes with squark exchange are suppressed for our scenarios, since the squarks are heavy: $m(\tilde{q}) \gg M_Z$. In the SM the $Z - ZZ$ and $Z - \gamma\gamma$ vertices do not exist, thus also the couplings $Z - \tilde{B}\tilde{B}$ and $Z - \tilde{W}^3\tilde{W}^3$ vanish. But the lightest neutralino is dominantly ‘gaugino’, as we have seen in the example in section 2.2.3.2. (scenario L’), while the higgsino contribution is only $\sim 10\%$, leading to a suppression factor of 0.01.

$$\tilde{\chi}_1 = 0.995 \tilde{B} - 0.014 \tilde{W}^3 + 0.090 \tilde{H}_u^0 - 0.031 \tilde{H}_d^0 \quad (12)$$

Therefore also the s channel Z exchange is strongly suppressed.

To understand why the xsection for $\tilde{\chi}_2 \tilde{\chi}_1^\pm$ is particularly large, we must investigate the composition of $\tilde{\chi}_2$ and $\tilde{\chi}_1^\pm$, we choose as an example again model L’:

$$\tilde{\chi}_2 = -0.039 \tilde{B} - 0.962 \tilde{W}^3 + 0.226 \tilde{H}_u^0 - 0.146 \tilde{H}_d^0 \quad (13)$$

With formulae similar to those given in section 2.2.3.2. we can obtain

$$\tilde{\chi}_1^\pm = 0.98 \tilde{W}^\pm + 0.20 \tilde{H}^\pm \quad (14)$$

In principle a $W \tilde{\chi}^\pm \chi$ coupling can occur via higgsino components or via gaugino components. Here both the lightest chargino and the two first neutralinos are dominantly gaugino, so we can neglect the higgsino part. The gaugino coupling is determined by the wino components in the neutralino, since the bino \tilde{B} does not couple to W and \tilde{W} . Therefore $\tilde{\chi}_1$ is suppressed with respect to $\tilde{\chi}_2$ by $(0.014/0.96)^2 \sim 2 \cdot 10^{-4}$. The cross sections do not differ by such a large factor, since kinematically the lighter $\tilde{\chi}_1$ is preferred.

2.2.4.3 SUSY signatures

A) Tevatron

Per experiment we expect a total luminosity of 5000/pb. To see a new particle in this environment, a rule of thumb says that at least 100 must be produced (acceptance, efficiency, background!). So, the cross section table tells us that scenario L’ is very difficult, and for case B’ the best channel is:

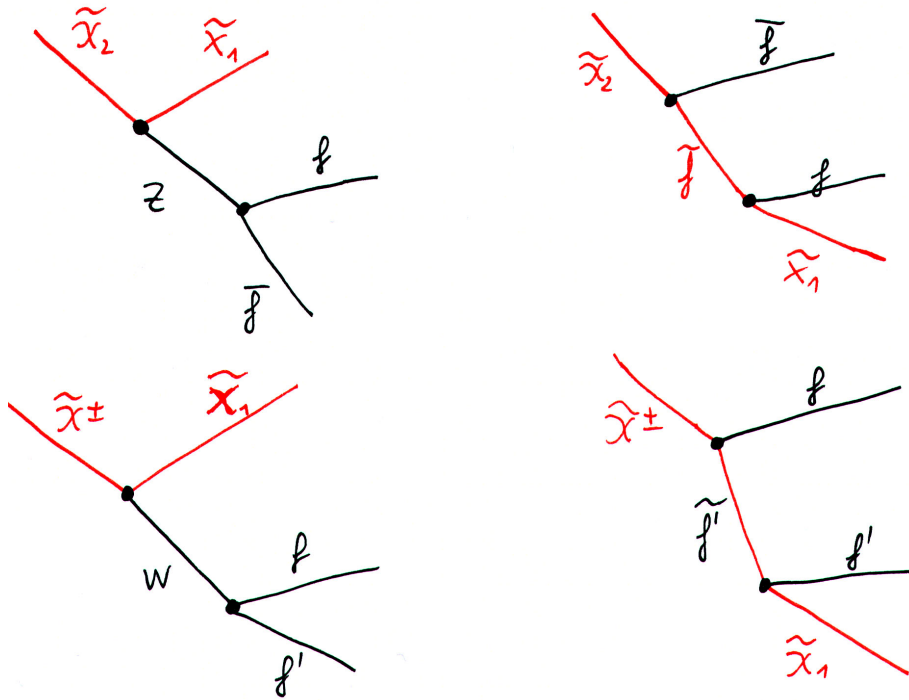
$$\tilde{\chi}_2 \tilde{\chi}_1^\pm$$

The dominant decay modes for these two SUSY particles are² (scenario B’):

²calculated with Isajet

initial	final	branching fraction
$\tilde{\chi}_2$	$e^+ e^- \tilde{\chi}_1$	5%
$\tilde{\chi}_2$	$\mu^+ \mu^- \tilde{\chi}_1$	5%
$\tilde{\chi}_2$	$\tau^+ \tau^- \tilde{\chi}_1$	41%
$\tilde{\chi}_2$	$\nu \bar{\nu} \tilde{\chi}_1$	49%
$\tilde{\chi}_2$	$q \bar{q} \tilde{\chi}_1$	0.04%
$\tilde{\chi}_1^\pm$	$e \nu \tilde{\chi}_1$	18%
$\tilde{\chi}_1^\pm$	$\mu \nu \tilde{\chi}_1$	18%
$\tilde{\chi}_1^\pm$	$\tau \nu \tilde{\chi}_1$	63%
$\tilde{\chi}_1^\pm$	$q \bar{q} \tilde{\chi}_1$	< 0.01%

with the corresponding feynman diagrams:



In scenario B' the second-lightest neutralino decays preferentially into a real \tilde{f}_R plus f , which is kinematically allowed for leptons, but not for quarks. The decay mode via virtual Z is suppressed (off shell). Neutrinos are preferred, since their NC couplings are bigger than for charged leptons (which have vector couplings ~ 0).

The τ final state is dominant due to the relatively large value of $\tan \beta$; this leads to a significant $\tilde{\tau}_R - \tilde{\tau}_L$ mixing, lowering the mass of $\tilde{\tau}_1$ with respect to \tilde{e}_R . The neutralino $\tilde{\chi}_2$ decays into $\tilde{\tau}_1$, which subsequently decays into τ and the LSP.

Since the cross section and the leptonic branching fractions are large, one can hope to find an excess of events with at least three leptons plus missing energy. In scenario B' one expects $\sim 350 \tilde{\chi}_2 \tilde{\chi}_1^\pm$ events. Half of them are invisible (3 or more neutrinos). Of the τ decays only 36% yield either e or μ , thus about 15% of all events give at least three leptons; counting only electrons and muons, this leaves about 50 events.

Background reactions are $W Z, Z Z, t \bar{t}$. Many of those events can be rejected by requiring that all

dilepton masses are **outside** the Z peak. With suitable cuts the signal efficiency is around **30%**, while the background fraction can be kept as low as **20%**. Thus one might see $15 + 3$ events for an expected background of **3** events - just enough to claim an excess!

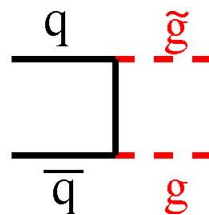
B) LHC

With luminosities well above $100/\text{fb}$ all channels listed in the above table seem detectable - except LSP pair production (invisible!). However, for benchmark L' the selectron cross section is small and background ($WW \rightarrow e\nu\nu$) important, so that it will probably not be possible to establish this process.

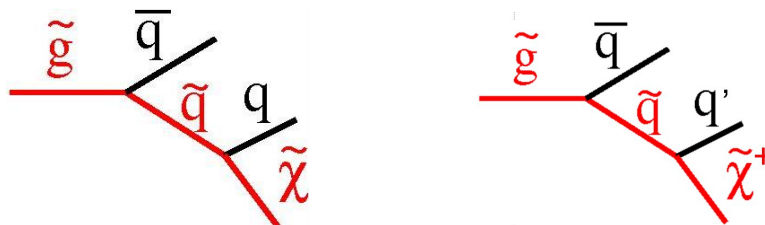
As an example we discuss here briefly gluino pair production:

$\tilde{g}\tilde{g}$

The production is described by this feynman diagram:



Gluinos decay dominantly as shown in the following figure:



These decay channels are unsuppressed only if (some) squarks are lighter than the gluino; this is in general not the case, as can be seen from the corresponding mass formulae. However, in scenarios B' and L' the squarks are sufficiently light. Let's look in detail³ at model B' (Isajet). The neutralino/chargino composition in terms of binos/winos/higgsinos is similar to scenario L' , discussed above. The gluino decay modes are:

³here we abbreviate $u d = u \bar{d} + \bar{u} d$ etc

	branching fraction
$u u \tilde{\chi}_1$	11%
$u u \tilde{\chi}_2$	2%
$d d \tilde{\chi}_1$	10%
$d d \tilde{\chi}_2$	2%
$u d \tilde{\chi}_1^\pm$	7%
$t t \tilde{\chi}_1$	1%
$t t \tilde{\chi}_2$	1%
$b b \tilde{\chi}_1$	4%
$b b \tilde{\chi}_2$	3%
$t b \tilde{\chi}_1^\pm$	13%

Comments:

- The intermediate state with a \tilde{q}_R is preferred since the ‘right’ squarks are lighter.
- While the \tilde{q}_R decays dominantly into $\tilde{\chi}_1 q$, the squarks \tilde{q}_L strongly prefer $\tilde{\chi}_2 q$ or $\tilde{\chi}_1^\pm q'$ as final state. Reason: The coupling constant of ‘left’ squarks is:

$$g_L \sim g_V + g_A = (I_3 - 2Q \sin^2 \theta_W) + (I_3) = 2I_3 - 2Q \sin^2 \theta_W \quad (15)$$

So they couple via electroweak isospin I_3 to winos ($\tilde{\chi}_2, \tilde{\chi}_1^\pm$!), while the ‘right’ coupling

$$g_R \sim g_V - g_A = (I_3 - 2Q \sin^2 \theta_W) - (I_3) = -2Q \sin^2 \theta_W \quad (16)$$

to winos vanishes. The \tilde{q}_R couples to bino components, so that the lightest $\tilde{\chi}_1$ is preferred.

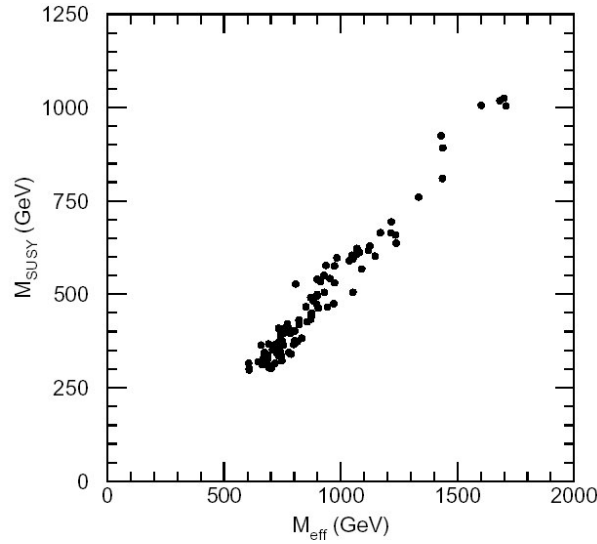
- The stop \tilde{t}_1 is quite light, but this advantage is eaten up by the heavy top quark!
- Since sbottom and stop states are mixtures, there is no preferred coupling to either $\tilde{\chi}_1$ or $\tilde{\chi}_2/\tilde{\chi}_1^\pm$.
- The channels not shown in the table (s, c) contribute as much as u, d .
- The neutralino $\tilde{\chi}_2$ decays dominantly into $\tilde{\chi}_1$ plus a $\tau^+ \tau^-$ pair (41%), thanks to the low $\tilde{\tau}_1$ mass, other decay modes lead to electron, muon or neutrino pairs, see above.
- The chargino will decay dominantly into leptons and $\tilde{\chi}_1$, see above.

Thus, also gluino decays yield leptons. However, since we have discussed similar signatures before, we concentrate here on the decay of the gluino into hadrons plus LSP (about half of all decays); the signature is: jets plus missing energy. Of course, apart from gluino pair production also squark production contributes to this final state!

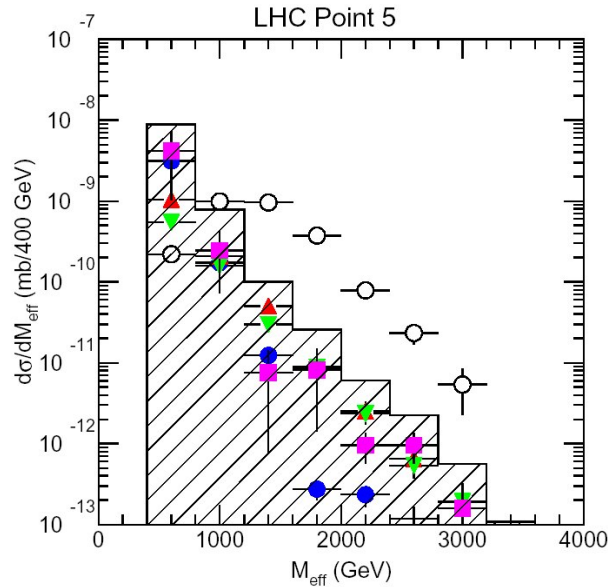
It turns out that the masses M_{SUSY} of the SUSY particles (gluinos, squarks) can be estimated by the following observable:

$$M_{eff} = \cancel{E}_T + \sum_{jets j} p_T^j \quad (17)$$

Monte Carlo studies show that in the MSSM-4 there is a strong correlation:



Here $M_{SUSY} = \min(m_{\tilde{g}}, m_{\tilde{q}})$. M_{eff} is bigger than M_{SUSY} since per event two primary SUSY particles are created! The next figure shows the expected M_{eff} distribution⁴



compared to background expectations, in the ATLAS experiment. The following selection cuts were applied:

$$\cancel{E}_T > 100 \text{ GeV} \quad p_T^j > 50 \text{ GeV}, j = 1 \dots 4 \quad (100 \text{ GeV for } j = 1) \quad (18)$$

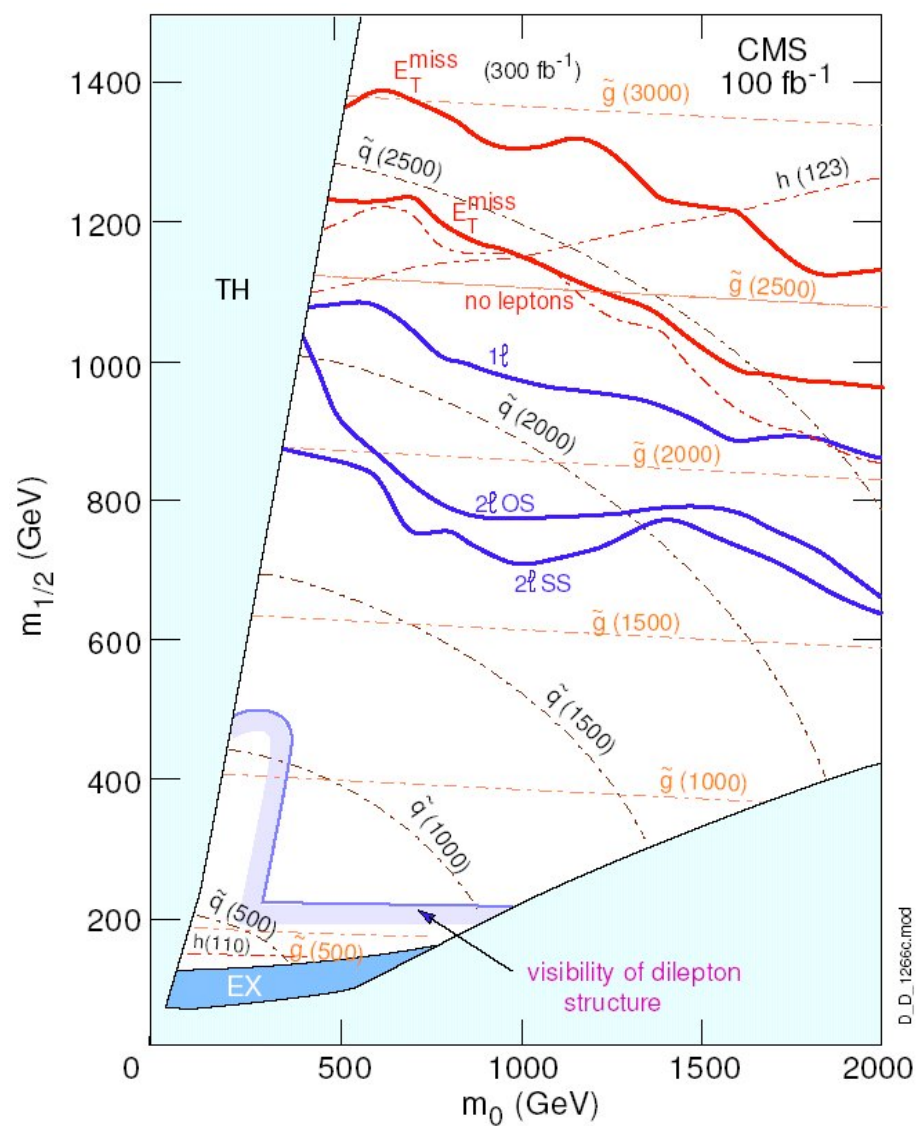
The SUSY cross section is large, since gluinos and squarks are produced via strong interactions. As can be seen from the figure the background⁵ is small compared to the signal at large M_{eff} values, thus a discovery should not be a problem.

Finally we compare the overall SUSY reach at the LHC comparing different signatures⁶:

⁴for LHCC benchmark point 5: $m_0 = 100 \text{ GeV}$, $m_{1/2} = 300 \text{ GeV}$, $A_0 = 300 \text{ GeV}$, $\tan \beta = 2.1$, $\mu > 0$. The gluino mass is **767 GeV**.

⁵top = filled circles, W+jets = triangles, Z + jets = inverted triangles, QCD = squares, SUSY = open circles

⁶ $\tan \beta = 35$, $A_0 = 0$



Overall the channel ‘missing E_T plus jets’ gives the best coverage of the $m_0 - m_{1/2}$ plane! These SUSY parameters correspond to gluino and squark masses beyond 2 TeV.